

The GUAPOS project. V: The chemical ingredients of a massive stellar protocluster in the making

Á. López-Gallifa^{1*}, V. M. Rivilla¹, M. T. Beltrán², L. Colzi¹, C. Mininni³, Á. Sánchez-Monge^{4,5}, F. Fontani², S. Viti^{6,7}, I. Jiménez-Serra¹, L. Testi⁸, R. Cesaroni², and A. Lorenzani²

¹Centro de Astrobiología (CAB) CSIC-INTA, Ctra. de Ajalvir, km. 4, Torrejón de Ardoz, E-28850 Madrid, Spain

²INAF-Osservatorio Astrofisico di Arcetri, Largo E. Fermi 5, I-50125, Florence, Italy

³INAF-IAPS, via del Fosso del Cavaliere 100, I-00133 Roma, Italy

⁴Institut de Ciències de l'Espai (ICE, CSIC), Carrer de Can Magrans, s/n, E-08193 Bellaterra, Barcelona, Spain

⁵Institut d'Estudis Espacials de Catalunya (IEEC), E-08034 Barcelona, Spain

⁶Leiden Observatory, Leiden University, Huygens Laboratory, Niels Bohrweg 2, NL-2333 CA Leiden, The Netherlands

⁷Department of Physics and Astronomy, University College London, Gower Street, WC1E 6BT, London, UK

⁸Dipartimento di Fisica e Astronomia, Università di Bologna, Via Gobetti 93/2, 40122 Bologna, Italy

Accepted XXX. Received YYY; in original form ZZZ

ABSTRACT

Most stars, including the Sun, are born in rich stellar clusters containing massive stars. Therefore, the study of the chemical reservoir of massive star-forming regions is crucial to understand the basic chemical ingredients available at the dawn of planetary systems. We present a detailed study of the molecular inventory of the hot molecular core G31.41+0.31 from the project GUAPOS (G31.41+0.31 Unbiased ALMA sPectral Observational Survey). We analyze 34 species for the first time plus 20 species analyzed in previous GUAPOS works, including oxygen, nitrogen, sulfur, phosphorus, and chlorine species. We compare the abundances derived in G31.41+0.31 with those observed in other chemically-rich sources that represent the initial and last stages of the formation of stars and planets: the hot corino in the Solar-like protostar IRAS 16293–2422 B, and the comets 67P/Churyumov-Gerasimenko and 46P/Wirtanen. The comparative analysis reveals that the chemical feedstock of the two star-forming regions are similar. The abundances of oxygen- and nitrogen-bearing molecules exhibit a good correlation for all pair of sources, including the two comets, suggesting a chemical heritage of these species during the process of star formation, and hence an early phase formation of the molecules. However, sulfur- and phosphorus-bearing species present worse correlations, being more abundant in comets. This suggests that while sulfur- and phosphorus-bearing species are predominantly trapped on the surface of icy grains in the hot close surroundings of protostars, they could be more easily released into gas phase in comets, allowing their cosmic abundances to be almost recovered.

Key words: Astrochemistry - Line: identification - ISM: molecules - ISM: individual object: G31.41+0.31 - Stars: formation - comets: general

1 INTRODUCTION

One of the fundamental open questions in astrochemistry is to understand which is the chemical feedstock of star and planet birthsites, and how it is transferred during the different phases of evolution of star and planetary systems: from parental molecular clouds, to starless/prestellar cores, to protostars, to planet-forming disks, and to planetary objects (planets, comets and asteroids). Nowadays, it is debated to what extent the molecular content is conserved or significantly reprocessed between the different evolutionary stages.

It has been shown that water ices from the Solar Nebula were widely available for the formation of the subsequent planetary system (Cleeves et al. 2014; Altwegg et al. 2017), and that at least most of them could survive to the process of accretion in planet-forming disks (Öberg et al. 2011; Visser et al. 2009). The detection of molecules in

protoplanetary disks also suggest that the chemical reservoir found in planet-forming sites might be directly inherited from earlier phases (e.g., Loomis et al. 2018; Bianchi et al. 2019; Booth et al. 2021; van der Marel et al. 2021; Ceccarelli et al. 2023; Tobin et al. 2023). Moreover, the molecular abundances of some species derived in planet-forming disks are similar to those found in comets (Öberg et al. 2015). Supporting this chemical heritage, Bockelée-Morvan et al. (2000) found that the abundances of some selected molecules present in the comet Hale-Bopp are similar to those of several interstellar high-mass star-forming regions. More recently, Drozdovskaya et al. (2019) showed that the molecular abundances of the comet 67P/Churyumov-Gerasimenko and the Solar-like protostellar environment IRAS 16293–2422 B are reasonably well correlated. Furthermore, Coletta et al. (2020) found that the molecular ratios of two complex organic molecules (COMs, species with >5 atoms; Herbst & van Dishoeck 2009), methyl formate and dimethyl ether, are nearly constant in multiple sources at different evolutionary stages of star

* E-mail: alvarolg@cab.inta-csic.es

and planetary system formation (molecular clouds, prestellar cores, low-, intermediate- and high-mass star-forming regions, protostellar shocks, and comets).

Since there is a growing evidence that our Sun was born in a dense stellar cluster that included also massive stars (Carpenter 2000; Lada & Lada 2003; Porras et al. 2003; Reach et al. 2009; Adams 2010; Öberg et al. 2011; Dukes & Krumholz 2012; Pfalzner & Vincke 2020; Korschinek et al. 2020; Brinkman et al. 2021), the study of the chemical composition of massive star-forming regions can give us information about the molecular feedstock of an environment that might resemble the birthsite of our Solar System. This is the main purpose of the project GUAPOS (G31.41+0.31 Unbiased ALMA sPectral Observational Survey), which carried out a spectral survey of the whole ALMA Band 3 towards the massive star-forming region G31.41+0.31 (hereafter G31.41). This region, with a mass of $70 M_{\odot}$ (Cesaroni 2019), harbors a hot molecular core (HMC) where at least four massive protostars are forming (Beltrán et al. 2021). G31.41 is located at 3.75 kpc distance (Immer et al. 2019), and has a luminosity of $\sim 4.4 \times 10^4 L_{\odot}$ (Osorio et al. 2009). The G31.41 hot core is one of the most chemically-rich sources in the Galaxy (Beltrán et al. 2009; Rivilla et al. 2017; Suzuki et al. 2023). The initial exploitation of GUAPOS data were focused on selected categories of COMs, like the isomers of glycolaldehyde (HCOCH₂OH; Mininni et al. 2020; hereafter GUAPOS I), peptide-like bond molecules (Colzi et al. 2021; hereafter GUAPOS II), several oxygen- and nitrogen-bearing COMs (Mininni et al. 2023; hereafter GUAPOS III); and phosphorus-bearing molecules (Fontani et al. 2024; hereafter GUAPOS IV).

The aim of this work, GUAPOS V, is to extend the chemical chemical census of the G31.41 massive star-forming region already presented in previous GUAPOS works, with the aim of comparing it with those of other well-studied astronomical objects at different evolutionary stages of the star- and planet-formation process. We have chosen sources that have been extensively studied in a homogeneous way, i.e. using the same dataset analyzed with the same method, and providing chemical censuses of tens of species, which will allow us to study the chemical budgets of different chemical families in a statistical way. The chosen sources to perform the comparison are: the low-mass proto-Solar analogue IRAS 16293-2422 B (hereafter IRAS16B; Jørgensen et al. 2016; Drozdovskaya et al. 2019), and the comets 67P/Churyumov-Gerasimenko (hereafter 67P/C-G; Rubin et al. 2019; Drozdovskaya et al. 2019), and 46P/Wirtanen (hereafter 46P/W; Biver et al. 2021). In Sect. 2 we present the ALMA observations of G31.41 used in our analysis. In Sect. 3 we describe the census of molecules that we have used to compare the chemical reservoir of G31.41 with those of other sources. In Sect. 4 we present the molecular data analysis of the G31.41 spectra. In Sect. 5, we quantitatively compare the molecular abundances derived in G31.41 with those of other three sources using three complementary statistical tests. In Sect. 6 we discuss the implications of our results, and in Sect. 7 we summarize the main conclusions of this work.

2 ALMA OBSERVATIONS OF G31.41+0.31

The observations were carried out with ALMA (Atacama Large Millimeter Array) during the Cycle 5 as part of the project 2017.1.00501.S (PI: M. T. Beltrán). The phase center was $\alpha_{J2000} = 18^{\text{h}}45^{\text{m}}34^{\text{s}}$ and $\delta_{J2000} = -0.1^{\circ}12'45''$. We fully covered the Band 3 (86.05 GHz - 115.91 GHz) obtaining an unbiased spectral survey. The frequency resolution of the correlator setup was 0.49 MHz equivalent to a velocity resolution of $\sim 1.6 \text{ km s}^{-1}$ at 90 GHz. The datacubes of the whole survey were created using a common restoring beam

of $1.2''$, about 4500 au. The uncertainties in the flux calibration are $\sim 5\%$ (from Quality Assessment 2 reports), which is in good agreement with flux uncertainties at ALMA band 3 reported in Bonato et al. (2018). For more details regarding the observations we refer to Mininni et al. (2020).

3 SAMPLE OF MOLECULES

The molecules considered in this study were selected because they have been detected or searched for (providing an upper limit for their column density) towards at least two of the four sources considered (the high- and low-mass star-forming regions G31.41 and IRAS16B, respectively, and the comets 67P/C-G and 46P/W). The total number of molecules considered for the comparative study are 57 and the information about the detection or non detection of the molecules towards the four astronomical sources are listed in Table B1. For IRAS16B, we have used the abundances and upper limits reported in Drozdovskaya et al. (2019) (see also references therein), Martín-Doménech et al. (2017), Coutens et al. (2018, 2019), Calcutt et al. (2019) and Manigand et al. (2021). Regarding 67P/C-G, we used the results presented in Calmonte et al. (2016), Dhooghe et al. (2017), Fayolle et al. (2017), Altwegg et al. (2019), Hadraoui et al. (2019), Rubin et al. (2019), Schuhmann et al. (2019) and Rivilla et al. (2020); while for 46P/W we considered the information reported in Biver et al. (2021). For G31.41, we have used the molecules already reported in previous works (GUAPOS I, Mininni et al. (2020); II Colzi et al. (2021); III, Mininni et al. (2023); García de la Concepción et al. 2022; and Cesaroni et al. 1994), and the ones analyzed in this work (see Sect. 4). For NH₃, we used the data presented by Cesaroni et al. (1994), based on VLA observations with a beam of $1.3'' \times 1''$, which is very similar to that of the GUAPOS ALMA observations, and hence allows a fair comparison.

4 DATA ANALYSIS OF THE G31.41+0.31 SPECTRA

We present here the analysis of the molecular emission of 34 molecules in the GUAPOS spectral survey, along with other 20 molecules analyzed in previous works (see Table 1). The ALMA data were calibrated and imaged with CASA¹ (the Common Astronomy Software Applications package, McMullin et al. 2007). Since G31.41 presents an extremely rich spectrum, with no line-free channels, we did not perform the continuum subtraction in the uv-space before imaging. For each observed basebands, the spectrum including the continuum level was extracted from an area equal to the synthesized beam ($1.2''$) and centered on the continuum peak of our source. The root mean square (rms) noise of the spectra is 7-27 mK. More details are described in Mininni et al. (2020). To subtract the continuum in the extracted spectra, as described in Colzi et al. (2021), we applied to each baseband spectrum the sigma clipping method (c-SMC) of the python based tool STATCONT² (Sánchez-Monge et al. 2018).

To perform the spectral analysis (line identification and fitting) we use the Madrid Data Cube Analysis (MADCUBA) software³ (Martín et al. 2019). We searched for different molecules in the spectrum, and we fit them using the SLIM (Spectral Line Identification and Modeling) tool of MADCUBA, which incorporates the Cologne

¹ <https://casa.nrao.edu>

² <https://hera.ph1.uni-koeln.de/sanchez/statcont>

³ MADCUBA is developed at the Centro de Astrobiología (CAB) in Madrid, free access: <http://cab.intacsic.es/madcuba/Portada.html>

Table 1. Molecules analyzed on G31.41 throughout all GUAPOS publications that are used in this work. The molecules that are not detected, for which we provide column density upper limits, are indicated in italics.

This work						
HCN	HNC	CO	H ₂ CO	<i>H₂S</i>	CH ₃ CCH	CH ₃ NC
NH ₂ CN	<i>C₃H₆</i>	<i>HOCN</i>	<i>c-C₂H₄O</i>	<i>syn-CH₂CHOH</i>	CS	<i>PN</i> †
H ₂ CS	trans-HONO*	<i>PO</i> †	CH ₃ SH	SO	<i>CH₃Cl</i>	HC ₃ N
<i>HC₂NC</i>	<i>trans-C₂H₃CHO</i>	<i>HOCH₂CN</i>	<i>CH₃CHCH₂O</i>	<i>C₂H₅CHO*</i>	OCS	<i>gauche-C₂H₅SH</i>
CH ₃ OCH ₂ OH*	<i>S₂</i>	SO ₂	<i>HS₂</i>	<i>H₂S₂</i>	<i>NH₂CH₂COOH (conf. I)</i>	
Previous publications						
NH ₃ ^e	CH ₃ OH ^c	CH ₃ CN ^c	HNCO ^b	CH ₃ CHO ^c	NH ₂ CHO ^b	C ₂ H ₅ OH ^c
CH ₃ OCH ₃ ^c	trans-HCOOH ^d	CH ₃ NCO ^b	C ₂ H ₃ CN ^c	CH ₃ COCH ₃ ^c	CH ₃ C(O)NH ₂ ^b	CH ₃ NHCHO ^b
C ₂ H ₅ CN ^c	CH ₃ OCHO ^a	CH ₂ OHCHO ^a	CH ₃ COOH ^a	aGg'-(CH ₂ OH) ₂ ^c	gGg'-(CH ₂ OH) ₂ ^c	

References. *a*) GUAPOS I – Mininni et al. (2020); *b*) GUAPOS II – Colzi et al. (2021); *c*) GUAPOS III – Mininni et al. (2023); *d*) García de la Concepción et al. (2022); *e*) Cesaroni et al. (1994). Molecules marked with * are tentative detections. † We note that PN and PO are not detected towards the position of the hot molecular core analyzed in this work, but that they are detected towards shocked gas in the region that is analyzed in GUAPOS IV (Fontani et al. 2024).

Database for Molecular Spectroscopy⁴ (CDMS, Müller et al. 2001, 2005; Endres et al. 2016) and the Jet Propulsion Laboratory molecular catalogs⁵ (JPL, Pickett et al. 1998).

SLIM produces a synthetic spectrum assuming local thermodynamic equilibrium (LTE) conditions, and taking into account the line opacity (see formalism in Martín et al. 2019). Considering the high density of the G31.41 molecular core, which is $\sim 10^8 \text{ cm}^{-3}$ (Mininni et al. 2020), LTE is a good approximation. SLIM compares the synthetic LTE spectrum with the observed spectrum, and finds the best fit applying the AUTOFIT tool based on a Levenberg-Marquardt algorithm. The free physical parameters of the fit are: the column density (N), the excitation temperature (T_{ex}), the velocity ($v - v_0$), where v_0 is the systemic velocity of G31.41 (96.5 km s^{-1} , Beltrán et al. 2018), and the full width at half maximum (FWHM). As discussed in Mininni et al. (2020) and Colzi et al. (2021), the molecular emission fills the beam, and hence no beam dilution correction was applied.

G31.41 is a chemically-rich source, so the blending among lines of different species is frequent. To take this into consideration, we performed the fit of each molecule accounting also for the emission of all other species detected. To run AUTOFIT, we have selected the most unblended transitions of each molecule, and also those transitions that, together with the emission from other known species, well reproduce the observed spectrum. If possible, we have left free the four physical parameters of the fit. In case the AUTOFIT algorithm did not converge, we fixed some of the parameters. Unfortunately, in many cases AUTOFIT does not converge if T_{ex} is set as a free parameter due to the lack of enough transitions free of contamination and covering a broad range of energy levels. Thus, T_{ex} cannot be directly derived, and we assumed a value for it. For the most complex molecules with ≥ 6 atoms, which are expected to trace the hot molecular core, we have assumed 150 K (similar to the values derived by Rivilla et al. 2017; Mininni et al. 2020; Colzi et al. 2021); while for molecules with < 6 atoms, which likely trace colder gas, we have assumed 50 K. To evaluate the impact of these assumptions on the derived column densities, we have also repeated the fits using a range of temperatures: 100 and 200 K for molecules with ≥ 6 atoms, and 25 and 75 K for molecules with < 6 atoms, respectively. As shown in Table 2 and in Table A1, the resulting column densities in these

temperature ranges are, in most cases, within less than a factor of 2 with respect to the values derived using the assumed values of 50 K or 150 K. In addition, to allow the convergence of AUTOFIT in some cases, $v - v_0$ and/or FWHM were fixed to 0 km s^{-1} and 7 km s^{-1} , respectively, which fit properly the most unblended transitions.

Some of the molecules analysed present high abundances and thus they are optically thick. As a consequence, the derived N should be considered as a lower limit. In these cases, we have searched for and analysed their optically-thinner isotopologues to obtain a better estimation of the column density. If more than one isotopologue is well detected, we have adopted the optically thinnest to derive the N of the main isotopologue. We used the following values of the isotopic ratios, which depends on the galactocentric distance (D_{GC}), assuming D_{GC} for G31.41 of 5.02 kpc (calculated from the heliocentric distance of 3.75 kpc, Immer et al. 2019): $^{12}\text{C}/^{13}\text{C} = 39.5 \pm 9.6$ (Milam et al. 2005; Yan et al. 2019), $^{14}\text{N}/^{15}\text{N} = 340 \pm 90$ (Colzi et al. 2018), $^{32}\text{S}/^{34}\text{S} = 14.6 \pm 2.1$ (Yu et al. 2020) and $^{16}\text{O}/^{18}\text{O} = 330 \pm 140$ (Wilson 1999). Moreover, for isotopic ratios that are not sensitive to D_{GC} , we used: $^{34}\text{S}/^{33}\text{S} = 5.9 \pm 1.5$ (Yu et al. 2020), $^{34}\text{S}/^{36}\text{S} = 115 \pm 17$ (Mauersberger et al. 1996) and $^{18}\text{O}/^{17}\text{O} = 3.6 \pm 0.2$ (Wilson 1999, taking the value of local ISM).

The molecular abundances were obtained by using the column density of $N(\text{H}_2) = (1.0 \pm 0.2) \times 10^{25} \text{ cm}^{-2}$ derived from the continuum emission within the same region used to extract the spectrum (more details in Mininni et al. 2020).

In the following sections we describe in detail the fitting procedure and the results obtained for each molecular species (including isotopologues) detected, the tentative detections and the upper limits derived from the non-detected molecules. The spectroscopic information of all the molecules used in this work is summarized in Table C1. The transitions used for fitting each species are listed in Table D1.

4.1 Detected molecules

We summarize in Table 2 the results of the line fitting of the different molecules. For optically thick molecules, we show in the table only the result of the optically thin isotopologue used to derive the column density of the main isotopologue. The results of the fits of the remaining isotopologues, including the main ones, are shown in Table A1 instead. The detailed analysis of each molecule (and its isotopologues) are described in the following sections.

⁴ <http://cdms.astro.uni-koeln.de/classic/>

⁵ <https://spec.jpl.nasa.gov/ftp/pub/catalog/catdir.html>

4.1.1 Hydrogen cyanide (HCN)

The spectral profiles of the $J=1-0$ rotational transitions of HCN and H^{13}CN show clear absorptions (left and middle upper panels of Fig. F1), which are likely due to filtering of extended emission by the interferometer and/or possible infall motions. To derive the molecular abundance of HCN, we have then used the ^{15}N isotopologue, which shows a Gaussian emission profile (upper right panel of Fig. F1). The results of the fit are shown in Table 2. The derived line opacity (τ) is ~ 1.7 , which indicates that even the ^{15}N isotopologue is optically thick. The column density of HCN derived, assuming the $^{14}\text{N}/^{15}\text{N}$ ratio, is $(1.5 \pm 0.4) \times 10^{18} \text{ cm}^{-2}$. We warn that, due to the opacity, this value is likely a lower limit of the true column density.

4.1.2 Hydrogen isocyanide (HNC)

Similarly to HCN, the spectral profiles of the $J=1-0$ rotational transitions of HNC and HN^{13}C show absorptions (left and middle lower panels of Fig. F1). Unlike HC^{15}N , the $J=1-0$ transition of H^{15}NC is heavily contaminated with a transition of CH_3NH_2 (right lower panel of Fig. F1). Therefore, we derived an upper limit for its column density (procedure explained in Sect. 4.2) using the H^{15}NC isotopologue, and we retrieve the upper limit of the HNC column density applying the $^{14}\text{N}/^{15}\text{N}$ ratio (Table 2). We obtain a high HCN/HNC ratio > 136 , as expected in hot gas (Colzi et al. 2018; Hacar et al. 2020).

4.1.3 Carbon monoxide (CO)

Similarly to HCN and HNC, the spectral profiles of the $J=1-0$ rotational transitions of CO and ^{13}CO show strong absorptions (Fig. F2), so we searched for optically thinner isotopologues. The isotopologue C^{17}O is heavily blended with two bright transitions of CH_3COOH (Fig. F2), and thus we report an upper limit (procedure explained in Sect. 4.2). The transition of the C^{18}O isotopologue is detected, although partially blended with emission of CH_3OCHO (see Fig. F2). The transition of the optically thinner double isotopologue $^{13}\text{C}^{18}\text{O}$ is also detected (Fig. F2), only slightly blended with a transition of CH_3NCO . We used the $^{13}\text{C}^{18}\text{O}$ isotopologue to derive the column density of CO taking into account the slight contribution of CH_3NCO , and using the corresponding carbon and oxygen isotopic ratios. The results of the fits are shown in Table 2 and Table A1. The derived CO/H_2 ratio is 2.6×10^{-4} , which is consistent with the typical value found in molecular clouds (e.g. Dickman 1978; Lis & Goldsmith 1988; Duan et al. 2023).

4.1.4 Formaldehyde (H_2CO)

The brightest transition of H_2CO , $6_{1,5} \rightarrow 6_{1,6}$ at 101.3330 GHz (Table D1), is detected and appears unblended, but it is heavily optically thick ($\tau = 4$), while other weaker transitions appear heavily blended (Fig. F3). Thus, we searched for rarer isotopologues. The ^{13}C and the ^{17}O isotopologues are detected, but their transitions are partially optically thick ($\tau = 0.24$ and 0.4 , respectively, see Table A1). Moreover, the transition of HC_2^{17}O is partially blended with CH_3OH . The $6_{1,5} \rightarrow 6_{1,6}$ transition of the ^{18}O isotopologue is unblended, and it is optically thin ($\tau = 0.053$). Therefore, we used it to derive the column density of H_2CO , obtaining $(2.6 \pm 1.2) \times 10^{18} \text{ cm}^{-2}$ (Table 2).

4.1.5 Propyne (CH_3CCH)

We fitted the two K -ladders of the $J=5-4$ and $J=6-5$ rotational transitions showed in Fig. F4. Some of the transitions are blended with CH_3COCH_3 , $\text{aGg}'-(\text{CH}_2\text{OH})_2$ and CH_3OCHO . The observed spectrum is well reproduced with the combined emission of CH_3CCH and the blending species, as shown in Fig. F4. If we leave T_{ex} as a free parameter the AUTOFIT algorithm does not converge, hence we fixed it to 150 K. We derived a column density of $(1.20 \pm 0.09) \times 10^{17} \text{ cm}^{-2}$ (see Table 2).

4.1.6 Methyl isocyanide (CH_3NC)

We fitted the K -ladder of the $J=5-4$ rotational transition. As shown in Fig. F5, the $K=0$ and $K=1$ transitions (at 100.5265 GHz and 100.5242 GHz respectively, see Table D1) are slightly blended with $\text{aGg}'-(\text{CH}_2\text{OH})_2$. In addition, the $K=2$ transition (at 100.5174 GHz) is blended with CH_3OCHO and $K=3$ (at 100.5061 GHz) is blended with HCOCH_2OH and CH_3COCH_3 . The blending of the higher energy transitions of the K -ladder (see Table D1) does not allow convergence of the AUTOFIT algorithm leaving T_{ex} as a free parameter, so we fixed it to 150 K. We retrieved a column density of $(1.1 \pm 0.4) \times 10^{15} \text{ cm}^{-2}$ (see Table 2).

4.1.7 Cyanamide (NH_2CN)

We show in Fig. 1 the most intense and less blended transitions of this species (Table D1). The $5_{1,5} \rightarrow 4_{1,4}$ transition at 99.3112 GHz is only marginally contaminated by CH_3COOH . The other transitions of the right panels of Fig. 1, are partially blended with CH_3COOH , $\text{C}_2\text{H}_5\text{OCHO}$, $\text{C}_2\text{H}_5\text{OH}$ and with a transition not identified, respectively. We note that all other transitions predicted by the LTE model are consistent with the observed spectra, but they are heavily blended with emission from other species. The transitions used for the fit are partially optically thick ($\tau = 0.04 - 0.34$; Table 2). We searched for the ^{13}C isotopologue, but it is not detected. The $\text{NH}_2\text{CN}/\text{NH}_2\text{CHO}$ ratio in G31.41 is 0.007, using the value derived here and that reported by Colzi et al. (2021) for formamide. For comparison, in IRAS16B is 0.02 (Coutens et al. 2018), which is only a factor three of difference suggesting that the NH_2CN column density that we have derived for G31.41 is more or less reliable.

4.1.8 Carbon monosulphide (CS)

The only rotational transition of CS in the GUAPOS spectral range is the $2 \rightarrow 1$ at 97.9810 GHz (see Table D1), which is optically thick and it shows a clear absorption probably due to filtering of extended emission and/or infall (see Fig. 2). The transitions of the isotopologues ^{13}CS , C^{34}S and C^{33}S are unblended, but they also are optically thick, with τ of 2.5, 1.17 and 1.0 respectively (see Table D1). The isotopologues C^{36}S and $^{13}\text{C}^{34}\text{S}$ are also detected with no or very little contamination (Fig. 2). For the fit of C^{33}S and C^{36}S isotopologues, we fixed the FWHM to 9.5 km s^{-1} (see Table 2 and Table A1), derived from the fit of C^{34}S , instead of the 7 km s^{-1} generally used when no further information are available and the AUTOFIT do not converge. We used the optically thinner isotopologue, C^{36}S ($\tau = 0.08$), to derive the column density of CS, which is shown in Table 2.

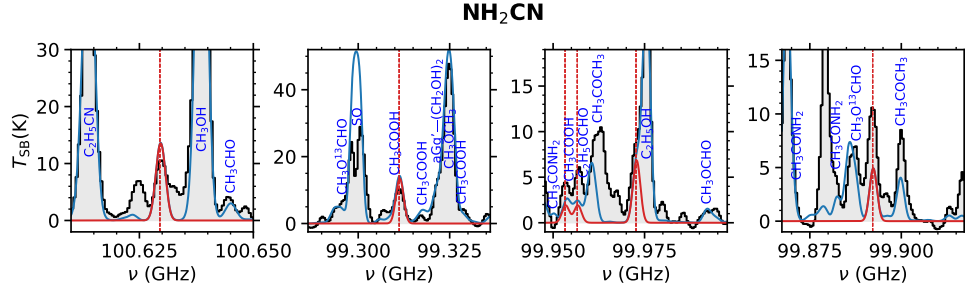


Figure 1. NH_2CN described in Sect. 4.1.7. The black histogram and its grey shadow are the observational spectrum. The red curve is the fit of the individual transition and the blue curve is the cumulative fit considering all detected species. The red dashed lines are the frequency of the transitions that we are fitting. The plots are sorted by decreasing intensity of the corresponding species (red line).

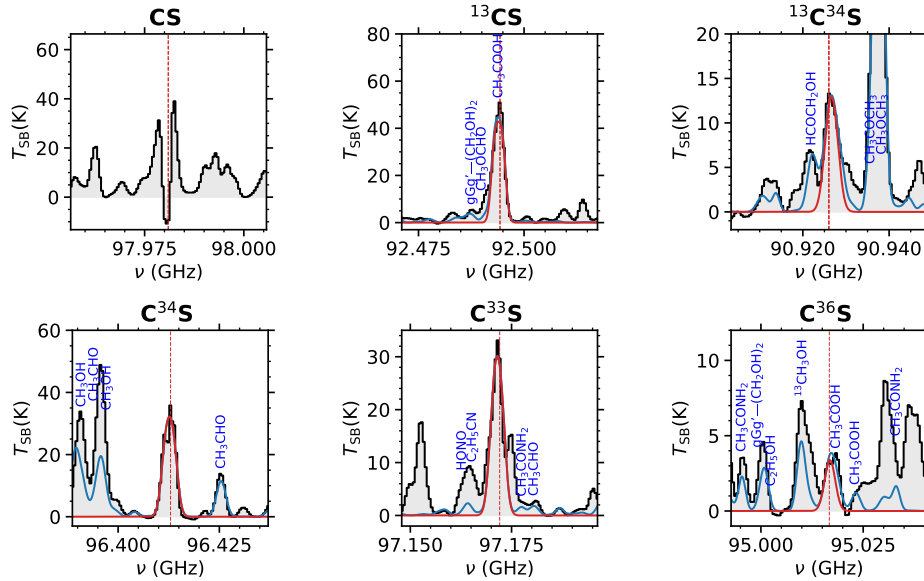


Figure 2. CS isotopologues described in Sect. 4.1.8. The black histogram and its grey shadow are the observational spectrum. The red curve is the fit of the individual transition and the blue curve is the cumulative fit considering all detected species. The red dashed lines indicate the frequency of the molecular transitions. The plots are sorted by decreasing intensity of the corresponding species (red line).

4.1.9 Ethylene oxide ($c\text{-C}_2\text{H}_4\text{O}$)

Figure 3 shows selected transitions of $c\text{-C}_2\text{H}_4\text{O}$ detected towards G31.41, which are unblended or partially blended and intense, with emission from other species whose joint contribution explains well the observed spectrum. We note that the remaining transitions predicted by the LTE model are consistent with the observed spectrum, but appear more blended with transitions of other species. The transitions are optically thin ($\tau \leq 0.10$; see Table D1). They cover a wide range of transitions energies from 9.5 K to 290 K, allowing us to leave T_{ex} as a free parameter. We found $T_{\text{ex}} = 132 \pm 7$ K, similar to the assumed value of 150 K assumed for the molecules with > 5 atoms. The other derived parameters are shown in Table 2.

4.1.10 Thioformaldehyde (H_2CS)

The fit of the detected transitions of H_2CS (see Fig. F6 and Table D1) gives a $T_{\text{ex}} = 38$ K (see Table A1), and indicates that the emission of the molecule is optically thick. We have thus searched for optically thinner isotopologues with ^{13}C , ^{33}S and ^{34}S , which are also detected and shown in Fig. F6. Since AUTOFIT does not converge leaving

T_{ex} as a free parameter, we fixed it. We do not use the value derived for the main isotopologue because of its optical thickness, but we used instead 50 K, following our general criteria. The transitions of the ^{13}C isotopologue are partially blended, while the transitions of $\text{H}_2\text{C}^{33}\text{S}$ are less blended with other species (Fig. F6). The isotopologue $\text{H}_2\text{C}^{34}\text{S}$ is slightly optically thick ($\tau = 0.03\text{-}0.33$), whereas $\text{H}_2\text{C}^{33}\text{S}$ has a lower τ of 0.01-0.07. Therefore, we used the $\text{H}_2\text{C}^{33}\text{S}$ isotopologue to retrieve the column density of H_2CS (Table 2). We note that the H_2CS column density derived by using $\text{H}_2\text{C}^{34}\text{S}$ would be a factor 3.6 lower, confirming that it is partially optically thick.

4.1.11 Nitrous acid (HONO)

Some few transitions of this species are detected with no or slight blending (see Table D1), such as the $6_{1,5} \rightarrow 6_{0,6}$ transition at 98.0877 GHz shown (fourth panel of Fig. F7), the $4_{0,4} \rightarrow 3_{0,3}$ at 93.9528 GHz (slightly blended with CH_3CONH_2 ; upper right panel of Fig. F7), and the $8_{1,7} \rightarrow 8_{0,8}$ transition at 111.5519 GHz (second leftmost upper panel of Fig. F7). We note that all other transitions predicted by the LTE model are consistent with the observed spectra, but they are heavily blended, with only one possible discrepancy of

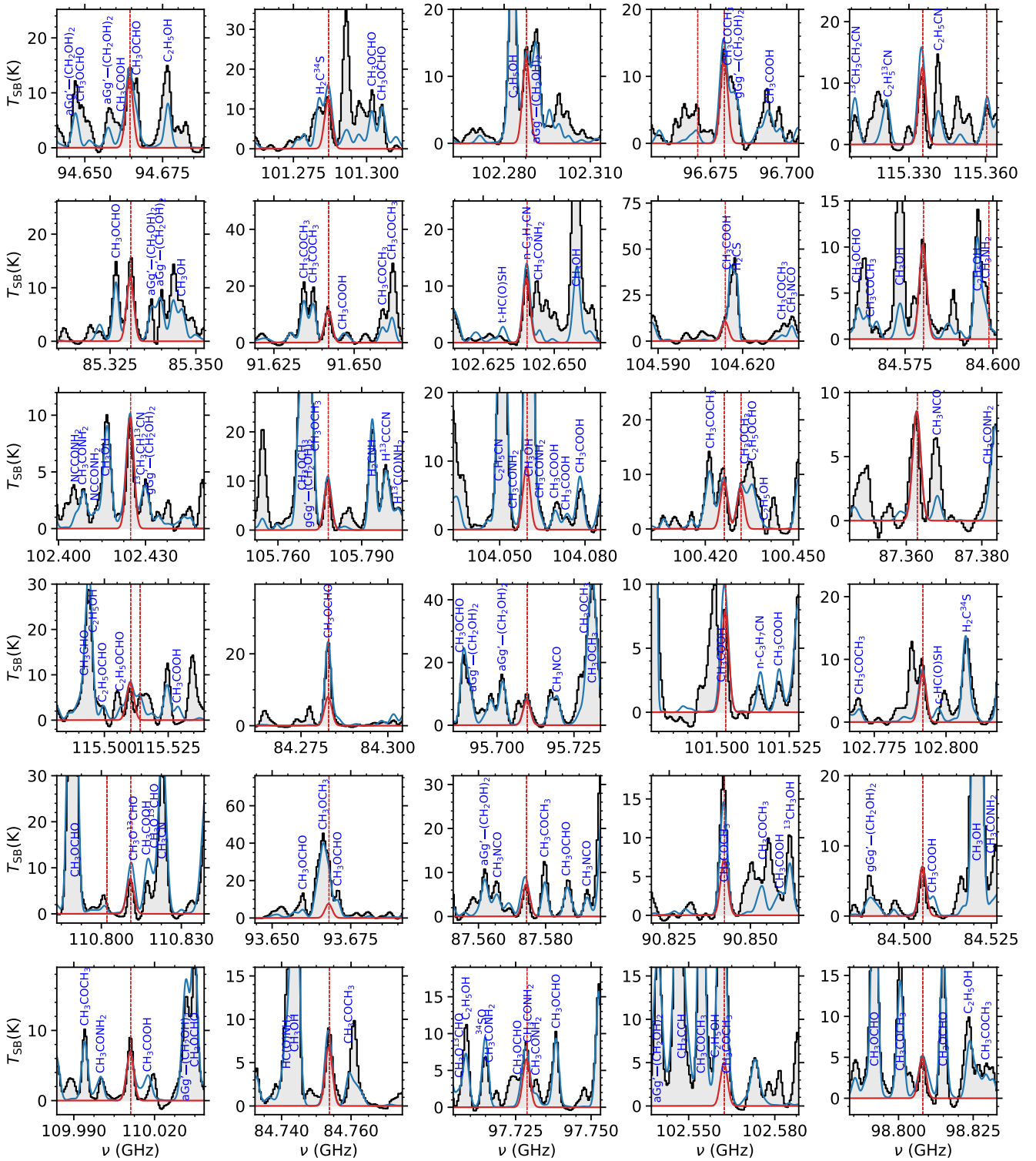
c-C₂H₄O

Figure 3. c-C₂H₄O described in Sect. 4.1.9. Selected transitions of c-C₂H₄O are shown, more transitions are detected but are not part of this figure. The black histogram and its grey shadow are the observational spectrum. The red curve is the fit of the individual transition and the blue curve is the cumulative fit considering all detected species. The red dashed lines indicate the frequency of the molecular transitions. The plots are sorted by decreasing intensity of the corresponding species (red line).

the $3_{1,2} \rightarrow 3_{0,3}$ at 85.7329 GHz, in which the LTE model overestimate the observed spectrum by ~ 1.5 K (middle right panel of Fig. F7). This difference might be due to a non optimal baseline subtraction, considering that the uncertainty of the continuum level of the ALMA baselines in the GUAPOS survey is of the same order (1.2 K, as described in Colzi et al. 2021). Since the number of unblended transition detected of this species is not enough to claim a robust detection, we consider it as a tentative detection. We note that this species has been only detected previously towards IRAS16B by Coutens et al. (2019). In this source the HONO/CH₃OH ratio is 9×10^{-5} , whereas the ratio in G31.41 we derived a similar value of 6×10^{-5} , which further supports that the molecule is tentatively detected.

4.1.12 Sulphur monoxide (SO)

Four intense and unblended transitions of SO are detected (see Fig. F8 and Table D1). The AUTOFIT converged leaving all parameters free (see Table A1). The results indicate that three of the transitions are optically thick ($\tau > 0.8$; Table D1), and that only the $5_4 \rightarrow 4_4$ transition is optically thin ($\tau=0.15$). Therefore, we used the isotopologue ³⁴SO, whose detected transitions are shown in the lower panels of Fig. F8. Since the main isotopologue is optically thick, we do not use the T_{ex} derived for it, but assume a value of 50 K, following our general criteria. The $2_3 \rightarrow 1_2$ transitions at 97.7153 GHz (lower left panel) is completely unblended, while the other three are partially blended. These transitions are optically thin ($\tau < 0.2$). We applied the ³²S/³⁴S ratio to derive the column density of SO (see Table 2).

4.1.13 Methyl mercaptan (CH₃SH)

We have detected several unblended transitions of CH₃SH (see Fig. 4 and Table D1). These transitions are optically thin ($\tau < 0.042$). The remaining CH₃SH transitions, along with the contribution from other species, such as C₂H₅¹³CN or C₂H₅CHO, are consistent with the observed spectra. The derived parameters of the fit are shown in Table 2.

4.1.14 Cyanoacetylene (HC₃N)

The spectral coverage of the GUAPOS survey contains the $J=10-9$, $J=11-10$ and $J=12-11$ transitions of HC₃N. The transitions $J=10-9$ and $J=12-11$ are unblended, while the $J=11-10$ transitions is partially blended with CH₃OCHO (see Fig. F9 and Table D1). By fitting these transitions we obtained a value for T_{ex} of 58 ± 8 K (see Table A1), and line opacities of $\tau=1.6-2.0$, which indicate that the main isotopologue is optically thick. We have also searched for the three ¹³C isotopologues: H¹³CCCN, HC¹³CCN and HCC¹³CN. We fixed the T_{ex} to 50 K because the values obtained from the HC₃N fit are not reliable due to the high optical depth. The transitions of the three isotopologues are unblended, or they are blended with emission from other identified species that explain properly the observed spectrum. The transition $J=12-11$ of HCC¹³CN is blended with HCOCH₂OH; the transition $J=11-10$ of H¹³CCCN is blended with C₂H₃CN and CH₃COOH; and the transition $J=12-11$ of HC¹³CCN is blended with aGg⁺-(CH₂OH)₂. The emission of the ¹³C isotopologues is optically thinner than that of the main isotopologue ($\tau = 0.26-0.40$). The column densities obtained for the three isotopologues are similar (Table 2). To derive the column density of HC₃N we have thus done the average of the column densities of the ¹³C isotopologues, and applied the isotopic ratio. Since the transitions have intermediate opacities,

the HC₃N column density might be slightly underestimated. We also searched for optically thinner isotopologues (¹⁵N or the double ¹³C isotopologues), but they are not detected. We note that the upper limits obtained for those isotopologues are consistent with the column density we report for HC₃N (Table 2).

4.1.15 Propanal (C₂H₅CHO)

The transitions $12_{0,12} \rightarrow 11_{1,11}$ E and $12_{0,12} \rightarrow 11_{1,11}$ A, both at 114.1011 GHz (Table D1), shown in upper middle panel of Fig. F10, are unblended. Figure F10 also shows other several transitions of C₂H₅CHO that reproduce well the observed spectra when the contribution of the emission from other species is considered. The other transitions predicted by the LTE model are consistent with the observed spectra, but they are heavily blended, and thus they are not used for the LTE model fit. Therefore, we consider that this species is tentatively detected. The results of the fit using the transitions shown in Fig. F10 are presented in Table 2. This molecule has been detected previously in other interstellar sources, including IRAS16B, in which Lykke et al. (2017) found a C₂H₅CHO/CH₃OH ratio of 2.2×10^{-4} , very similar to the value derived here for G31.41 (4.0×10^{-4}), which supports the tentative detection.

4.1.16 Carbonyl sulphide (OCS)

Several transitions of OCS, O¹³CS, OC³⁴S are clearly detected with no contamination (see Fig. F11 and Table D1). For OCS and O¹³CS AUTOFIT converges leaving T_{ex} as a free parameter, giving 74 ± 5 K and 35 ± 16 K, respectively (Table A1). However, both are optically thick ($\tau > 1.1$), and hence they do not provide a reliable value for the temperature. Thus, we have fixed $T_{\text{ex}} = 50$ K for the other isotopologues. The transitions of ¹⁸OCS and OC³³S are optically thinner ($\tau = 0.16-0.22$), and also unblended, except for the $8 \rightarrow 7$ transition of OC³³S, which is blended with CH₃OCHO, and for the $10 \rightarrow 9$ transition of ¹⁸OCS which is blended with an unidentified species. The results of the fits for the isotopologues and the main molecule are shown in Table 2 and Table A1. The column density of OCS using the isotopologue ¹⁸OCS or OC³³S are consistent within a factor of 1.3. We used the isotopologue ¹⁸OCS to estimate the column density of OCS because it is slightly optically thinner.

4.1.17 Methoxymethanol (CH₃OCH₂OH)

The LTE model using the parameters shown in Table 2 is depicted in Fig. F12, which shows several transitions of this species that might be detected towards G31.41. The inclusion of the contribution of the CH₃OCH₂OH emission, along with that of other molecules previously identified, explain better the observed spectrum than without considering it. We note that the remaining transitions predicted by the LTE model are consistent with the observed data. However, there is not enough unblended transitions of this species to provide a robust detection, and hence we consider it as tentative. This molecule has been only previously detected in the MM1 core of NGC6334-I by McGuire et al. (2017), in Orion KL by Tercero et al. (2018), and in IRAS16B by Manigand et al. (2020). These works found a CH₃OCH₂OH/CH₃OH ratios of 0.014, 0.014 and 0.029 respectively. In this work we have derived a very similar ratio of 0.034 towards G31.41, supporting the tentative detection.

Table 2: Results of the SLIM fits of the molecules analysed towards G31.41, ordered by increasing molecular mass, from which we have retrieved their abundances. For optically thick molecules, we include the optically thin isotopologue that we have used to derive the column density of the main isotopologue (the results of the other isotopologues are presented in Table A1 instead). The resulting physical parameters, along with their associated uncertainties, are presented. The values of the parameters fixed to perform some fits are shown without uncertainties. In the case of non detections, we indicated the upper limit in the column density with <. In the case of tentative detections, they are denoted with ~. When T_{ex} is fixed, we calculate in what factor the value of N changes when using the different temperatures T_{min} and T_{max} : 25-75 K and 100-200 K for fixed temperatures of 50 K and 150 K, respectively. We also present the maximum line opacity of the transitions of each molecule (τ_{max}), and the molecular abundances compared to H_2 . The transitions used to obtain these values are in Table D1.

Formula	T_{ex} (K)	N ($\times 10^{16} \text{ cm}^{-2}$)	$N(T_{\text{min}})/N(T_{\text{max}})$	$v - v_0$ (km s^{-1})	FWHM (km s^{-1})	τ_{max}^a	$N/N_{\text{H}_2}^b$ ($\times 10^{-8}$)	Fig.
Detected molecules								
HCN		150 ± 40	1.6-1.2				10 ± 6	F1
HC^{15}N	50	0.45 ± 0.02	1.6-1.2	0.3 ± 0.2	9.1 ± 0.3	1.7 ± 0.2	$(4.5 \pm 0.9) \times 10^{-2}$	F1
HNC*		<1.1	0.7-1.6				0.073	F1
H^{15}NC^*	50	<0.003	0.7-1.6	0	7	0.017	3.2×10^{-4}	F1
CO		$(2.6 \pm 1.5) \times 10^5$	1.0-2.1				$(2.6 \pm 1.6) \times 10^4$	F2
$^{13}\text{C}^{18}\text{O}$	50	20 ± 6	1.0-2.1	0	7	0.13 ± 0.11	2.0 ± 0.7	F2
H_2CO		$(2.6 \pm 1.2) \times 10^2$	2.0-1.0				26 ± 13	F3
$\text{H}_2\text{C}^{18}\text{O}$	50	0.78 ± 0.07	2.0-1.0	-0.9 ± 0.3	7.4 ± 0.7	0.053 ± 0.007	0.078 ± 0.017	F3
CH_3CCH	150	12.0 ± 0.9	0.6-1.7	1.3 ± 0.6	11.8 ± 1.2	0.06 ± 0.03	1.2 ± 0.3	F4
CH_3NC	150	0.11 ± 0.04	0.8-1.8	0	7	0.03 ± 0.03	$(1.1 \pm 0.5) \times 10^{-2}$	F5
NH_2CN	50	0.111 ± 0.008	0.6-1.6	-0.5 ± 0.3	7	0.34 ± 0.08	$(1.1 \pm 0.3) \times 10^{-2}$	1
CS		71 ± 22	0.6-1.4				7 ± 3	2
C^{36}S	50	0.04 ± 0.01	0.6-1.4	-0.5 ± 1.2	9.5	0.08 ± 0.04	$(4.2 \pm 1.3) \times 10^{-3}$	2
c- $\text{C}_2\text{H}_4\text{O}$	132 ± 7	6.3 ± 0.3		0.47 ± 0.15	8.6 ± 0.4	0.10 ± 0.03	0.63 ± 0.13	3
H_2CS		30.6 ± 11	0.6-1.6				3.1 ± 1.2	F6
$\text{H}_2\text{C}^{33}\text{S}$	50	0.36 ± 0.06	0.6-1.6	0	7	0.07 ± 0.06	$(3.6 \pm 1.0) \times 10^{-2}$	F6
trans-HONO	50	$\sim 0.45 \pm 0.06$	0.6-1.7	-1.1 ± 0.5	7	0.10 ± 0.06	$(4.5 \pm 1.1) \times 10^{-2}$	F7
SO		3.9 ± 0.8	0.6-1.4				0.39 ± 0.11	F8
^{34}SO	50	0.27 ± 0.04	0.6-1.4	1.3 ± 0.6	7	0.20 ± 0.06	$(2.7 \pm 0.7) \times 10^{-2}$	F8
CH_3SH	150	7.2 ± 0.4	0.5-1.6	1.3 ± 0.3	7	0.042 ± 0.014	0.70 ± 0.15	4
HC_3N		2.8 ± 0.4	1.1-1.2				0.28 ± 0.07	F9
H^{13}CCCN	50	0.062 ± 0.004	1.1-1.2	1.0 ± 0.3	9.2 ± 0.7	0.32 ± 0.08	$(6.2 \pm 1.3) \times 10^{-3}$	F9
HC^{13}CCN	50	0.070 ± 0.003	1.1-1.2	0.7 ± 0.3	10.4 ± 0.6	0.33 ± 0.05	$(7.0 \pm 1.5) \times 10^{-3}$	F9
HCC^{13}CN	50	0.080 ± 0.004	1.2-1.2	2.2 ± 0.3	9.5	0.40 ± 0.07	$(8.0 \pm 1.7) \times 10^{-3}$	F9
$\text{C}_2\text{H}_5\text{CHO}$	150	$\sim 3.00 \pm 0.15$	0.6-1.3	0.1 ± 0.2	7	0.02 ± 0.02	0.30 ± 0.07	F10
OCS		$(1.8 \pm 0.8) \times 10^2$	0.9-1.2				18 ± 9	F11
^{18}OCS	50	0.55 ± 0.07	0.9-1.2	2.9 ± 0.5	7	0.16 ± 0.06	$(5.5 \pm 1.3) \times 10^{-2}$	F11
$\text{CH}_3\text{OCH}_2\text{OH}$	150	$\sim (2.55 \pm 0.15) \times 10^2$	0.6-1.4	2.7 ± 0.3	7	0.02 ± 0.03	26 ± 6	F12
SO_2		10 ± 3					1.1 ± 0.4	F13
$^{34}\text{SO}_2$	56 ± 14	0.68 ± 0.14		1.9 ± 0.4	7	0.15 ± 0.05	$(7 \pm 2) \times 10^{-2}$	F13
Non detected molecules (upper limits)								
H_2S	50	$< 7.6 \times 10^4$	$9120-0.07^c$	0	7	$< 9 \times 10^{-3}$	$< 8 \times 10^3$	G1
C_3H_6	150	<3.6	0.6-1.6	0	7	$< 1.4 \times 10^{-3}$	<0.4	G1
HOCN	50	<0.006	0.6-1.8	0	7	<0.03	$< 6 \times 10^{-4}$	G1
syn- CH_2CHOH	150	<4.0	0.6-1.5	0	7	$< 9 \times 10^{-3}$	<0.4	G1
PN	50	<0.005	0.6-1.4	0	7	<0.02	$< 5.0 \times 10^{-4}$	G1
PO	50	<0.019	0.6-1.4	0	7	<0.015	$< 1.9 \times 10^{-3}$	G1
CH_3Cl	50	<0.04	0.6-1.6	0	7	<0.012	$< 4 \times 10^{-3}$	G1
HC_2NC	50	<0.003	0.9-1.2	0	7	$< 5 \times 10^{-3}$	$< 2.6 \times 10^{-4}$	G1
trans- $\text{C}_2\text{H}_3\text{CHO}$	150	<0.16	0.7-1.5	0	7	<0.010	$< 1.6 \times 10^{-2}$	G1
HOCH_2CN	150	<0.8	0.6-1.4	0	7	<0.011	$< 8 \times 10^{-2}$	G1
$\text{CH}_3\text{CHCH}_2\text{O}$	150	<1.9	0.8-1.2	0	7	<0.011	<0.19	G1
gauche- $\text{C}_2\text{H}_5\text{SH}$	150	<1.7	0.6-1.8	0	7	$< 9 \times 10^{-3}$	<0.17	G1
S_2	50	<290	1.2-1.1	0	7	<0.04	<29	G1
HS_2	50	<0.4	0.6-1.6	0	7	<0.02	$< 3 \times 10^{-2}$	G1
H_2S_2	50	<1.7	0.5-1.7	0	7	<0.06	<0.17	G1

Table 2: Continued.

Formula	T_{ex} (K)	N ($\times 10^{16} \text{ cm}^{-2}$)	$N(T_{\text{min}})/N$ - $N(T_{\text{max}})/N$	$v - v_0$ (km s^{-1})	FWHM (km s^{-1})	τ_{max}^a	$N/N_{\text{H}_2}^b$ ($\times 10^{-8}$)	Fig.
NH ₂ CH ₂ COOH	150	<2	0.7-1.6	0	7	$<5 \times 10^{-3}$	<0.2	G1

Notes. Isotopic ratios used: $^{12}\text{C}/^{13}\text{C} = 39.5 \pm 9.6$ (mean value of isotopic ratios from Milam et al. 2005 and Yan et al. 2019), $^{14}\text{N}/^{15}\text{N} = 340 \pm 90$ (Colzi et al. 2018), $^{32}\text{S}/^{34}\text{S} = 14.6 \pm 2.1$ (Yu et al. 2020), $^{34}\text{S}/^{33}\text{S} = 5.9 \pm 1.5$ (Yu et al. 2020), $^{34}\text{S}/^{36}\text{S} = 115 \pm 17$ (Mauersberger et al. 1996), $^{16}\text{O}/^{18}\text{O} = 330 \pm 140$ (Wilson 1999), $^{18}\text{O}/^{17}\text{O} = 3.6 \pm 0.2$ (Wilson 1999, taking the value of local ISM). ^a Maximum τ of all the transitions detected in each species. ^b Value of $N(\text{H}_2) = (1.0 \pm 0.2) \times 10^{25} \text{ cm}^{-2}$ (Mininni et al. 2020). ^c The transition of H₂S used has a high value of E_{up} of 520 K (see Table D1), which is completely out of the range of the T_{ex} adopted in the fits (25, 50 and 75 K); and thus the derived N is extremely sensitive to the value assumed. * This molecule, HNC, is detected, but the profiles of the main isotopologue and the ^{13}C isotopologue show absorptions (see Fig. F1). We have derived an upper limit using the ^{15}N isotopologue (see details in Section 4.1.2).

5 COMPARISON WITH OTHER INTERSTELLAR SOURCES

We have compared the chemical reservoir of G31.41, using the molecular abundances derived here and in previous works (Cesaroni et al. 1994; Mininni et al. 2020; Colzi et al. 2021; Mininni et al. 2023) with that of the hot corino surrounding the low-mass Solar-like protostar IRAS16B, and the two comets 67P/C-G and 46P/W. While G31.41 and IRAS16B are two archetypical examples of a hot core and a hot corino, respectively, namely, the natal environments where massive and low-mass (Solar-like) protostars are born, the two comets (67P/C-G and 46P/W) are representatives of the outcoming products of the process of star and planet formation. We select these three sources to be compared with G31.41 because its chemical reservoir have been previously extensively studied, providing molecular catalogs of tens of molecules. Their molecular abundances were derived from deep surveys based on homogeneous data, which were analysed using the same procedure, like we have performed in the GUAPOS project for G31.41. This is a fundamental requisite to obtain reliable values of molecular abundance ratios, and fair comparisons of the chemical content of the four sources.

IRAS16B is the prototypical example of a low-mass star-forming region, and its rich molecular content has been obtained using ALMA data in multiple works, especially from the Protostellar Interferometric Line Survey (PILS) (e.g. Jørgensen et al. 2016). IRAS16B is a member of a multiple protostellar system (Maureira et al. 2020), and it is commonly considered a proto-Solar analog given its low mass, which is $0.1 M_{\odot}$ (Jacobsen et al. 2018). IRAS16B is the most chemically rich hot corino known, and several molecules have been detected towards it for the first time in the ISM (e.g. Coutens et al. 2019; Zeng et al. 2019), or in low-mass star-forming regions (e.g. Martín-Doménech et al. 2017; Ligterink et al. 2017; Calcutt et al. 2018; Coutens et al. 2018). For our comparison, we have used the molecular abundances of 55 molecular species towards IRAS16B (41 detected molecules; and 14 non detected molecules for which we used column density upper limits, see Table B1), obtained from Drozdovskaya et al. (2019) (see also references therein), Martín-Doménech et al. (2017), Coutens et al. (2018, 2019), Calcutt et al. (2019) and Manigand et al. (2021). For those molecules for which the uncertainties of the derived molecular column densities are not available, we have assumed an uncertainty of 20%.

The comet 67P/C-G was visited by the European Space Agency (ESA) spacecraft Rosetta, which provided us with unique data thanks to the instrument on board ROSINA (Rosetta Orbiter Spectrometer for Ion and Neutral Analysis; Le Roy et al. 2015). This instrument has provided an unprecedented view of the volatile chemical composition of a comet (Rubin et al. 2019) by obtaining *in-situ* data from the volatile emanated from the nucleus of the comet. The abundances were obtained by mass spectroscopy, thus isomer groups cannot be distinguished. We used here the data from Calmonte et al. (2016), Dhooche et al. (2017), Fayolle et al. (2017), Altwegg et al. (2019), Hadraoui et al. (2019), Rubin et al. (2019), Schuhmann et al. (2019) and Rivilla et al. (2020). For the comparison presented in this work we have considered the molecular abundances of 32 isomeric groups (29 detections and 3 non detected species for which abundance upper limits were derived, see Table B1).

The chemical composition of the comet 46P/W was studied in detail with the IRAM 30-m telescope and the NOEMA interferometer when its distance was less than 0.1 au from Earth by Biver et al. (2021). We have used the molecular abundances reported in Biver et al. (2021), which provided information of 31 species (11 detections

and 20 non detections for which upper limits are available, see Table B1).

5.1 Comparison of molecular abundances

We have directly compared the molecular abundances derived towards the four sources in Fig. 5, in which we have normalized the column densities of all the species with respect to methanol (CH_3OH). To compute the molecular ratio uncertainties we have used error propagation for those column densities with symmetric uncertainties (e.g. those of G31.41 and IRAS16B). For the molecules with column densities reported with asymmetric uncertainties in the comet 67P/C-G (e.g. S-bearing from Calmonte et al. 2016), the error bars have been computed by considering the minimum and maximum ratios calculated considering the column density uncertainties, as also done by Drozdovskaya et al. (2019).

Figure 5 is composed of six panels that show the molecular abundance ratios for each possible pair of sources. In the cases in which the molecules are not detected, but upper limits of their column densities have been reported (see Section 4.2 for G31.41), we denote them with triangles. Due to the use of the mass spectroscopy technique for the comet 67P/C-G, we summed the column densities of the molecules with the same molecular mass of the other three sources for the comparison. In the case that the column density of one of the species is an upper limit, we have considered the sum as an upper limit as well.

In Figs. 6, 7, and 8 we have separated different families of molecules: i) oxygen(O)-bearing species; ii) nitrogen(N)-bearing species (including molecules with O); and iii) sulfur(S)-, phosphorus(P)- and chlorine(Cl)-bearing species. We have normalized the column density of each molecule by the reference molecule indicated in the axis label: CH_3OH for O-bearing, CH_3CN for N-bearing, and CH_3SH for S-, P- and Cl-bearing species. The column densities of CH_3OH and CH_3CN in G31.41 are calculated by Mininni et al. (2023) using $\text{CH}_3^{18}\text{OH}$ and $^{13}\text{CH}_3\text{CN}$ isotopologues respectively, while CH_3SH has been analyzed in this work (Sect. 4.1.13).

Figures 5, 6, and 7 shows in general a good correlation of O- and N-bearing species for all pair of sources, spanning a remarkably broad range of molecular abundance ratios, of up to six orders of magnitude. Most of the points fall in the ± 1 order of magnitude region from the 1:1 correlation (gray shaded area in the figures).

The case of S- and P-bearing species is different. Figure 5 shows that these species, when normalized to CH_3OH , lie well below the 1:1 correlation, namely they are underabundant, in the star-forming regions (G31.41 and IRAS16B) compared to 67P/C-G (upper middle and lower left panels in Fig. 5). However, when the abundance ratios are computed by using CH_3SH instead of CH_3OH , they lie closer to the 1:1 line as shown in Fig. 8. This suggests that the chemical content of S- and P-bearing species, unlike O- and N-bearing, is different in the star-forming regions and the comet 67P/C-G. We will discuss in detail the implications of this in Sect 6.

5.2 Correlation between sources using statistical tests

To quantify the goodness of the molecular abundance correlations between the different sources, and hence to investigate how their chemical contents behave, we used three statistical tests: Spearman (r_s), Kendall (τ) and Theil-Sen (T-S). Each test checks different properties of the correlations: while Spearman and Kendall report whether the data points are monotonically increasing or not (by comparing the ranges and by analyzing if the pairs of data are concordant

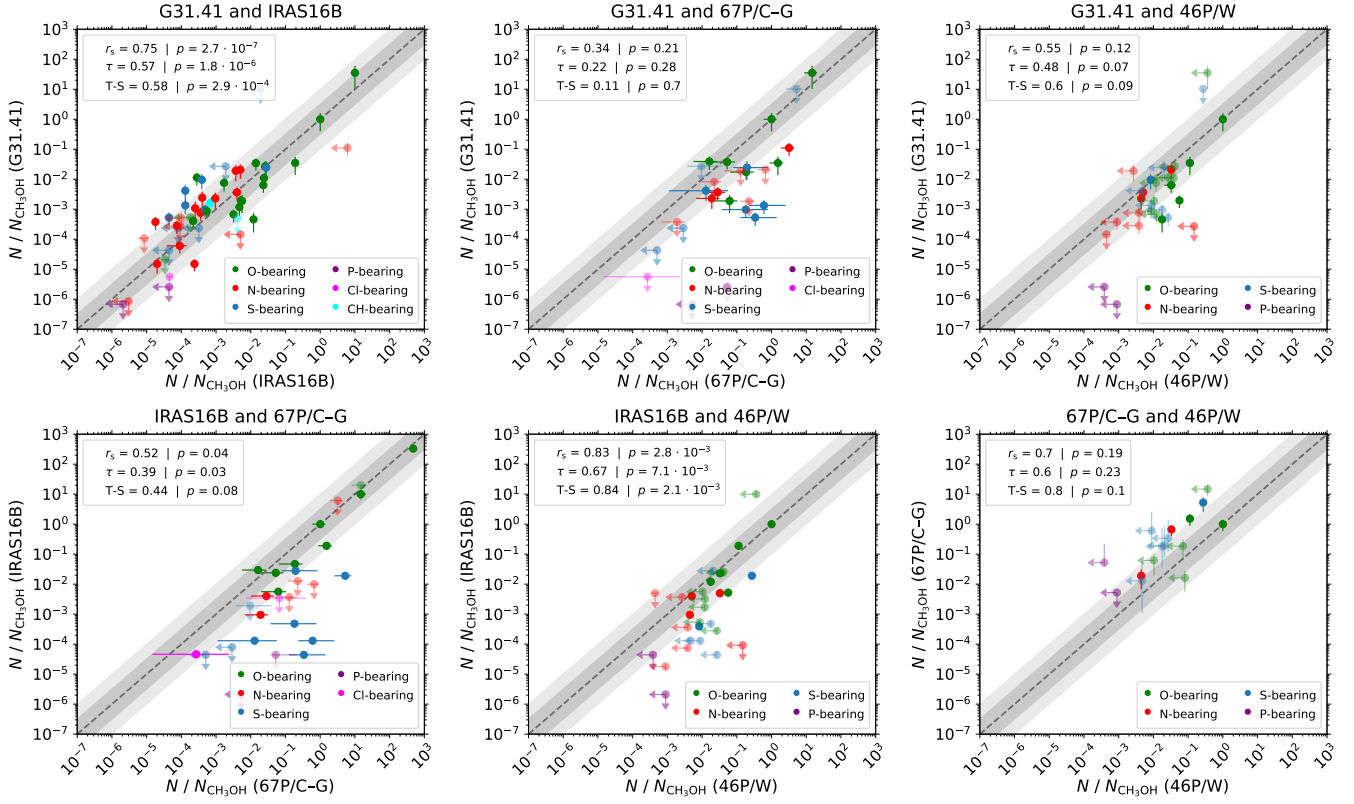


Figure 5. Molecular abundances with respect to CH₃OH (of detected molecules and upper limits) classified by chemical families on different pair of sources. The errorbars marked with arrows are the upper limits. Grey dotted line is the 1:1 relation on each plot. Dark and light grey are half and one order of magnitude difference with respect to the grey dotted line. In the legend: r_s is the Spearman correlation coefficient, τ is the Kendall one, T-S is the Theil-Sen one, p is the correspondent p -value.

or discordant, respectively), Theil-Sen indicates if the data can be fitted by a linear fit, similarly to the Pearson correlation coefficient, but with the advantage of being less sensitive to the outliers. We present a detailed description of the three tests in Appendix E.

We applied the correlation tests using the molecular abundance ratios of the detected molecules. For each statistical test we calculated its p -value, which quantifies the reliability of the derived correlation coefficient by taking into account the number of data points and the goodness of the correlation. If the correlation coefficient calculated is perfectly reliable, then the p -value is 0, whereas a value of 1 indicates that the correlation coefficient is not reliable at all. We considered that a value below 0.1 is good enough to trust the correlation coefficient.

To analyse the results of the correlation tests we have computed four correlation matrices, one for each test, and one for the average correlation coefficient (m) defined as:

$$m = \frac{r_s + \tau + \text{T-S}}{3}, \quad (1)$$

where r_s , τ , and T-S are Spearman, Kendall and Theil-Sen statistical tests, respectively. Each matrix is divided in cells, with each cell corresponding to the correlation coefficient for a pair of sources. The correlation matrices have been obtained for different groups of molecules: all molecules (Fig. 9), O-bearing (Fig. 10), N-bearing (Fig. 11), and S-bearing (Fig. 12). As shown in these figures, the results obtained using the three different statistical tests and the average one (m) are overall similar, which stress the robustness of the correlation analysis. For this reason, we will restrict the discussion to the average correlation matrices.

In order to help the interpretation of the correlation tests, we have arbitrarily defined different values of the average correlation coefficient: $m \geq 0.9$ (excellent correlation), $0.9 > m \geq 0.7$ (very good correlation), $0.7 > m \geq 0.5$ (good correlation), $0.5 > m \geq 0.3$ (poor correlation), $0.3 > m$ (no correlation).

5.2.1 Full chemical reservoir

We first discuss the results found considering all the molecules analyzed.

The average correlation matrix (Fig. 9) indicates that the pairs of sources with very good correlations are IRAS16B and 46P/W ($m=0.78$, p values < 0.01 , based on 10 molecular species), and the two comets ($m=0.7$, $p = 0.1-0.23$, indicating a low reliability because is based on only 5 species). Good correlations are also found between G31.41 and IRAS16B ($m=0.63$, $p < 0.01$ based on 35 molecular species), and G31.41 and 46P/W ($m=0.54$, $p = 0.07-0.12$, based on 9 species). The poorest correlations involve the 67P/C-G comet with the two star-forming regions: IRAS16B ($m=0.45$, $p < 0.1$, based on 17 molecular species), and G31.41 ($m=0.22$, based on 15 molecular species, with high p values ranging 0.21–0.7, which indicated a low reliability). As discussed in the next subsections, the main reason for these discrepancies are the different molecular abundance ratios for S-bearing species found in 67P/C-G compared to those in the star-forming regions.

In the following subsections, we discuss the results obtained for the different families of molecules.

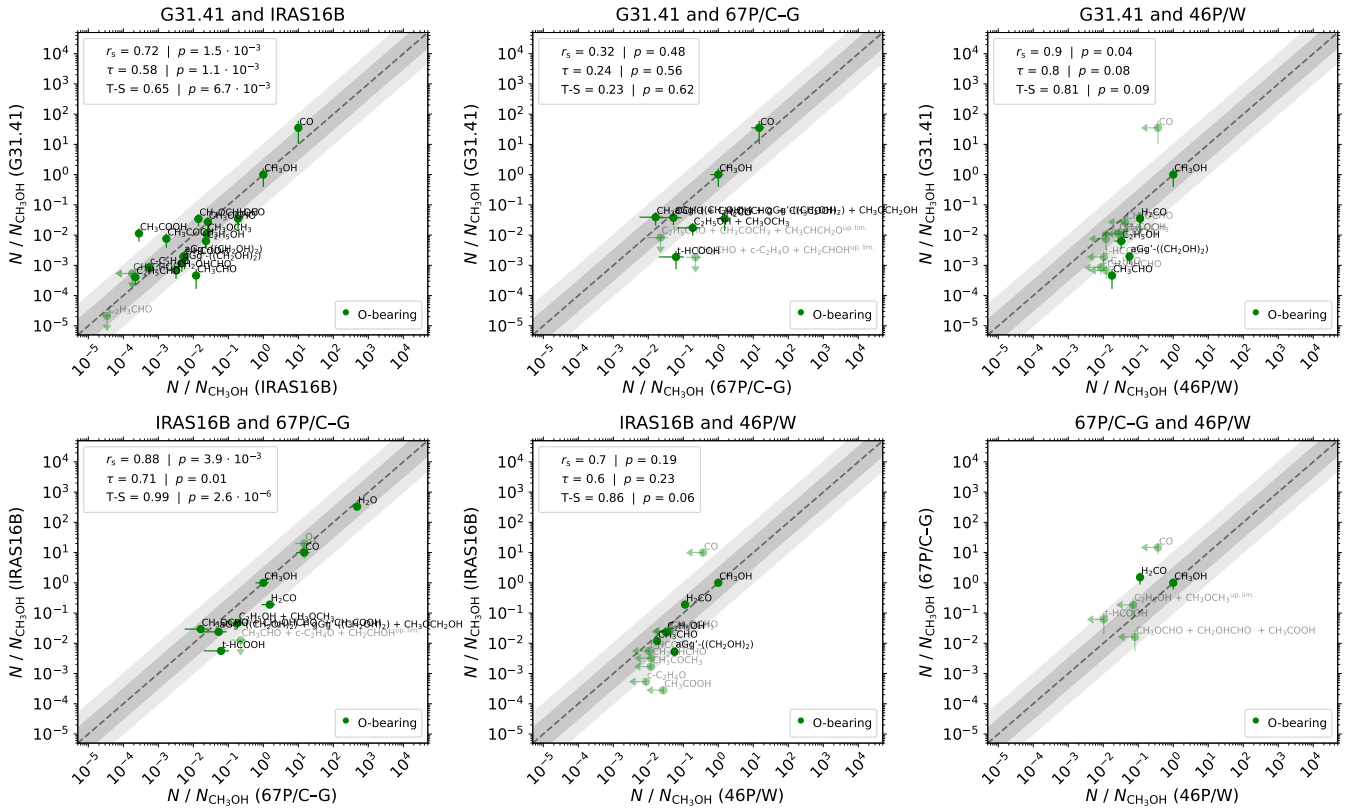


Figure 6. Same as in Fig. 5 but only plotting O-bearing molecules with respect to CH_3OH . The errorbars marked with arrows are the upper limits. Grey dotted line is the 1:1 relation on each plot. Dark and light grey are half and one order of magnitude difference with respect to the grey dotted line. In the legend: r_s is the Spearman correlation coefficient, τ is the Kendall one, T-S is the Theil-Sen one, p is the correspondent p -value. We note that the limits of the axis are different to those shown in Fig. 5 for display purposes.

5.2.2 O-bearing species

Considering only O-bearing species, the correlation matrix (Fig. 10) indicates that this family of molecules has in general better correlations between sources than the full chemical reservoir (compare with Fig. 9). The best correlation is found between IRAS16B and comet 67P/C-G ($m=0.86$, $p \leq 0.01$, using 8 molecules); in agreement with the results previously found by Drozdovskaya et al. (2019). There is also a very good correlation between G31.41 and 46P/W ($m=0.84$, $p < 0.1$, based on 5 molecules).

A very good correlation is also found between IRAS16B and 46P/W ($m=0.72$, using 5 molecules). The lower middle panel of Fig. 6 shows that the detected molecules are inside the grey shaded area around the 1:1 correlation line, although the p values (0.06–0.23) indicate that the correlation should be taken with some caution.

The correlation between G31.41 and IRAS16B is good ($m=0.65$, $p < 0.001$, based on 16 molecules). Most of the molecular abundance ratios (with the only exceptions of CH_3CHO and CH_3COOH) fall within the area of ± 1 order of magnitude around the 1:1 line, confirming a very similar chemical composition of O-bearing molecules between these two star-forming sources. CH_3CHO is less abundant in G31.41 by a factor of 26.1, which might be partially due to opacity effects, since Mininni et al. (2023) derived that its emission is partially optically thick, with line opacities up to $\tau=0.2$. CH_3COOH is more abundant in G31.41 than in IRAS16B by a factor of 40.5. However, this result is compatible with the ones obtained by Mininni et al. (2020), in which CH_3COOH was more abundant in G31.41

compared with other 3 sources by a factor of 2 and also was more abundant on G31.41 than other 18 sources.

The poorest correlation found is between G31.41 and 67P/C-G ($m=0.26$, based on 7 groups with same molecular mass). The reason for this poor correlation (see upper middle panel of Fig. 6) is the presence of two outliers: t-HCOOH and H_2CO . In the case of t-HCOOH , the transitions analyzed by García de la Concepción et al. (2022) are slightly optically thick ($\tau=0.05$ –0.2), so the true column density would be higher, and thus closer to the 1:1 region. These two outlier molecules might be either underabundant in G31.41 or overabundant in 67P/C-G. Comparing G31.41 with IRAS16B and the comet 46P/W, both molecules fall in the shaded area around the 1:1 line (Fig. 6; being t-HCOOH an upper limit in 46P/W). In addition, when comparing the two comets (67P/C-G and 46P/W), H_2CO and the upper limit of t-HCOOH are above the 1:1 line. Thus, these two species seem to be overabundant in comet 67P/C-G compared to the other sources.

We did not perform correlation tests for the 67P/C-G and 46P/W pair because only 2 molecular abundance ratios are available (lower right panel of Fig. 6).

5.2.3 N-bearing species

The correlation matrices of N-bearing species are shown in Fig. 11. The comparison between the two star-forming regions (G31.41 and IRAS16B) shows a very good correlation ($m=0.78$, $p \leq 0.01$, based on 11 molecules).

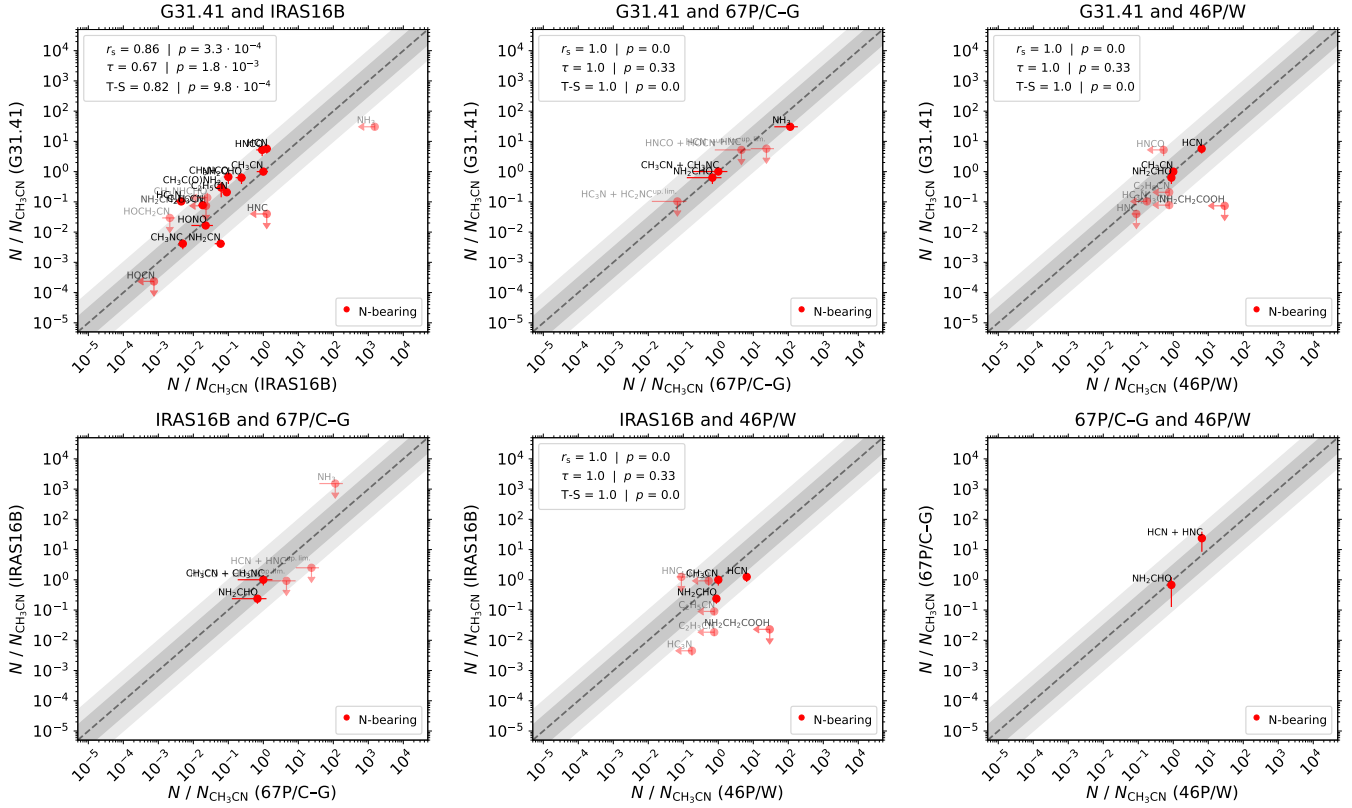


Figure 7. Same as in Fig. 5 but only for N-bearing molecules (including molecules containing O) with respect to CH₃CN. The errorbars marked with arrows are the upper limits. Grey dotted line is the 1:1 relation on each plot. Dark and light grey are half and one order of magnitude difference with respect to the grey dotted line. In the legend: r_s is the Spearman correlation coefficient, τ is the Kendall one, T-S is the Theil-Sen one, p is the correspondent p -value. We note that the limits of the axis are different to those shown in Fig. 5 for display purposes.

As shown in Fig. 7, most of the molecular abundance ratios are within the area of ± 1 order of magnitude with respect to the 1:1 line, with only two outliers: HC₃N and NH₂CN. Both molecules fall only slightly outside of the ± 1 order of magnitude area. As already mentioned in Sect. 4.1.7, this discrepancy in NH₂CN might be due to optical depth effects.

Only HCN, HNC, CH₃CN, and NH₂CHO are detected in both comets, and also NH₃ and CH₃CN were reported in 67P/C-G. As a consequence, only three molecular abundance ratios are available for the comparisons of G31.41 vs. 67P/C-G, G31.41 vs. 46P/W, and IRAS16B vs. 46P/W, and so the correlation tests performed should be taken with caution. The average correlation coefficients are in the three cases $m=1$ (Fig. 11), but the low number of points (only three), make these correlations not fully reliable.

For the two comparisons left (IRAS16B vs. 67P/C-G and 67P/C-G vs. 46P/W), we did not perform statistical tests because only two molecular abundance ratios are available.

5.2.4 S-, P- and Cl-bearing species

Figure 12 shows the correlation matrices for S-bearing molecules. The correlations are systematically poorer than those for O- and N-bearing molecules.

The comparison between the two star-forming regions, based on 6 molecules (upper left panel in Fig. 8), gives a good correlation in the Spearman and Kendall correlation matrix ($r_s=0.64$ and $\tau=0.55$ respectively). However, the Theil-Sen correlation matrix value gives

no correlation (T-S=0.2). This is because Theil-Sen searches for a linear fit, while the other two methods check if the points are monotonically increasing. The low correlation derived by Theil-Sen decreases the average coefficient to $m=0.46$, which is slightly below to the threshold we have considered for a good correlation. In any case, the low number of molecules considered (6), and the high p -values ($p=0.13$ - 0.70), advice to take this result with some caution.

We cannot retrieve the correlation coefficients in the comparisons involving 46P/W due to the low number of S-bearing species detected (only H₂S and CS), and the non detection of the reference molecule, CH₃SH.

The comparison between the comet 67P/C-G and the two star-forming regions gives no correlation ($m=-0.2$ for G31.41, and $m=0.09$ for IRAS16B; Fig. 12), confirming that the S chemical content in the comet significantly differs from that of the star-forming regions, unlike the O and N content, as already mentioned in Sect. 5.1.

Regarding Cl- and P-bearing species, we did not perform correlation tests given the low number of species detected. Only CH₃Cl has been detected towards IRAS16B and 67P/C-G (Fayolle et al. 2017), and PO towards 67P/C-G (Rivilla et al. 2020), preventing us to compare among the different sources.

6 DISCUSSION: THE CHEMICAL THREAD DURING STAR FORMATION

We have compared in this work the chemical composition of four sources that cover initial and final steps of the formation of stars

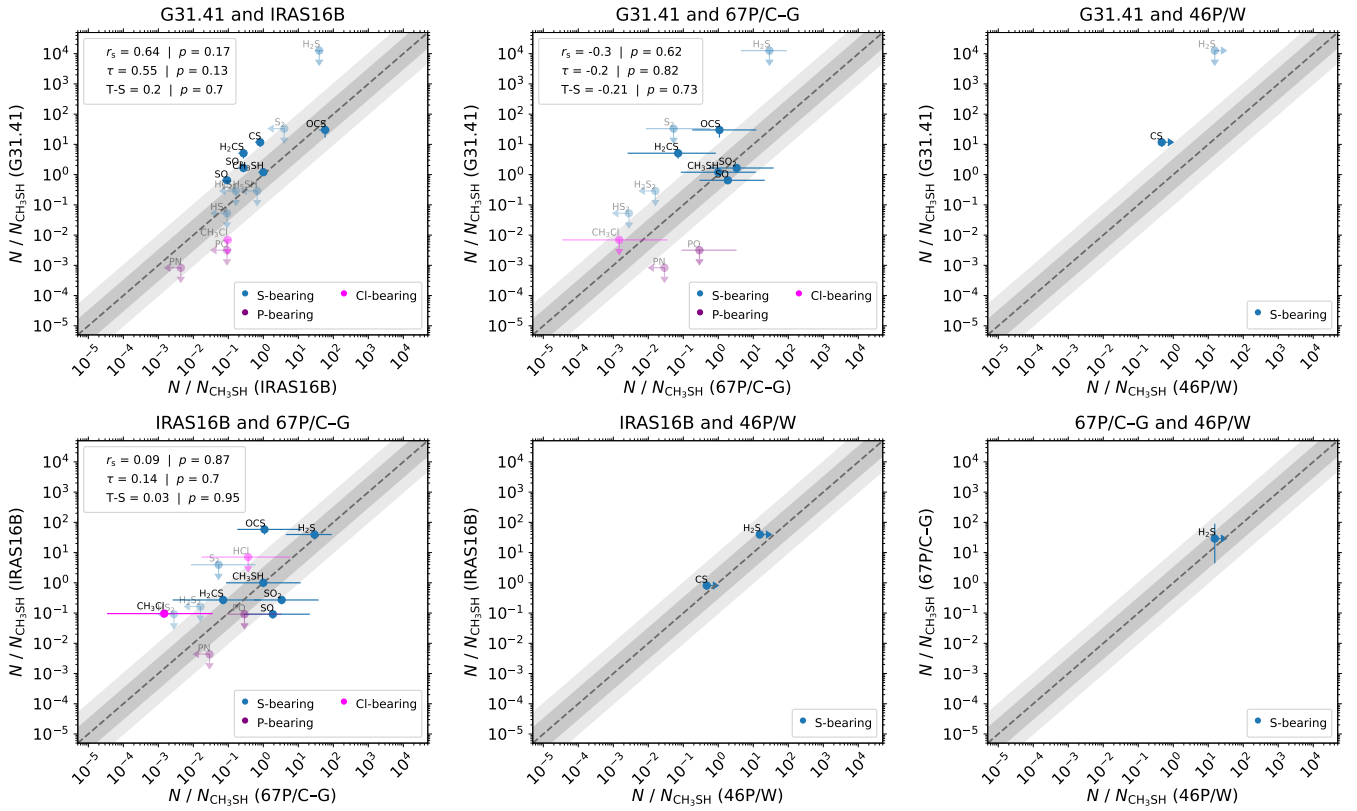


Figure 8. Same as in Fig. 5 but only for the P-, S-, and Cl-bearing molecules with respect to CH_3SH . The errorbars marked with arrows are the upper limits. Grey dotted line is the 1:1 relation on each plot. Dark and light grey are half and one order of magnitude difference with respect to the grey dotted line. In the legend: r_s is the Spearman correlation coefficient, τ is the Kendall one, T-S is the Theil-Sen one, p is the correspondent p -value. We note that the limits of the axis are different to those shown in Fig. 5 for display purposes.

and planetary systems. On the one hand, the natal cores in a high-mass and a low-mass star-forming region (G31.41 and IRAS16B, respectively). On the other hand, two Solar System comets (67P/C-G and 46P/W), whose chemical composition is thought to be almost pristine, namely it informs us about the primitive molecular ingredients of our planetary system that could have been delivered to the young Earth (Altwegg et al. 2016, 2019). In the following, we discuss the implications of our findings about the evolution of the chemical feedstock during the process of star and planet formation.

Complementing the correlations done in Sect. 5, and to follow how the molecular abundance ratios vary from source to source, we have plotted them in Fig. 13, separating O-bearing, N-bearing and S-bearing species. The two former are normalized by CH_3OH (upper right panel) and CH_3CN (upper left panel), respectively. The latter is normalized by CH_3OH (lower left panel) and CH_3SH (lower right panel). As shown in Fig. 13, and already mentioned in Sect. 5, we have found an overall very good correlation between the molecular abundance ratios of the two star-forming regions (G31.41 and IRAS16B), using a large sample of molecules (35 common detected species in both sources). Most of the molecular ratio pairs in these two regions are consistent within an order of magnitude, with variation factors of 1.0 ± 0.6 for O-bearing species, and of 2.3 ± 1.6 for N-bearing molecules. This similarity is remarkable because these two star-forming regions have very different physical properties. They differ in the masses of their gas envelopes ($70 M_\odot$ vs. $4 M_\odot$; Cesaroni 2019 and Jacobsen et al. 2018; respectively), their protostellar masses ($15\text{--}26 M_\odot$ vs. $0.1 M_\odot$), and their luminosities ($4.5 \times 10^4 L_\odot$

vs. $3 L_\odot$), from Beltrán et al. (2021) and Jacobsen et al. (2018), respectively. Their location within the Galaxy is also different, and the local environment clearly differs in terms of clustering: while G31.41 is a massive protostellar cluster (Beltrán et al. 2021), IRAS16B is an isolated low-mass triple protostellar system (see e.g., Maureira et al. 2020). This implies that the expected protostellar feedback (e.g. from protostellar molecular outflows, and UV radiation) is significantly different. As well, the protostellar heating timescales of the hot core G31.41 is expected to be much faster than that of the hot corino IRAS16B (Viti et al. 2004; Awad et al. 2010). Moreover, it should be noted that the spatial scales traced by the observations used in this work are very different: 4400 au for G31.41 and 60 au for IRAS16B (Mininni et al. 2020 and Jørgensen et al. 2018, respectively). In principle, one should expect that all these above-mentioned differences in the physical conditions might have an imprint in the molecular ratios in the gas phase, due to e.g. different desorption histories (thermal and/or shock-induced), UV processing, or spatial scale effects. However, we have found that the molecular ratios of O- and N-bearing species towards the hot core and hot corino of G31.41 and IRAS16B, respectively, are remarkably similar. This result is in good agreement with previous works that have found similar chemical reservoirs comparing tens of star-forming regions, based on smaller samples of molecules (e.g. Coletta et al. 2020; van Gelder et al. 2020; Colzi et al. 2021; Nazari et al. 2021, 2022; and references therein).

When the comparison is extended to comets, we have found different results depending on the chemical family. O- and N-bearing

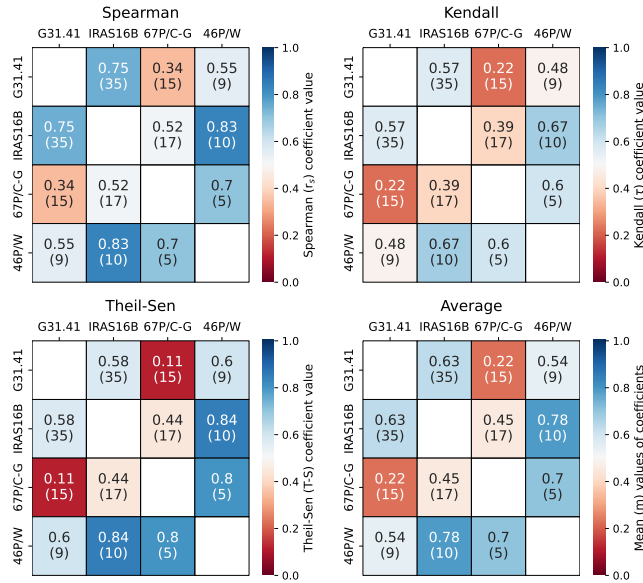


Figure 9. Correlation matrices considering all the molecules analysed in this work. The goodness of the correlation is color-coded, the bluer the color, the better the correlation. The value between brackets on each cell is the number of molecules considered.

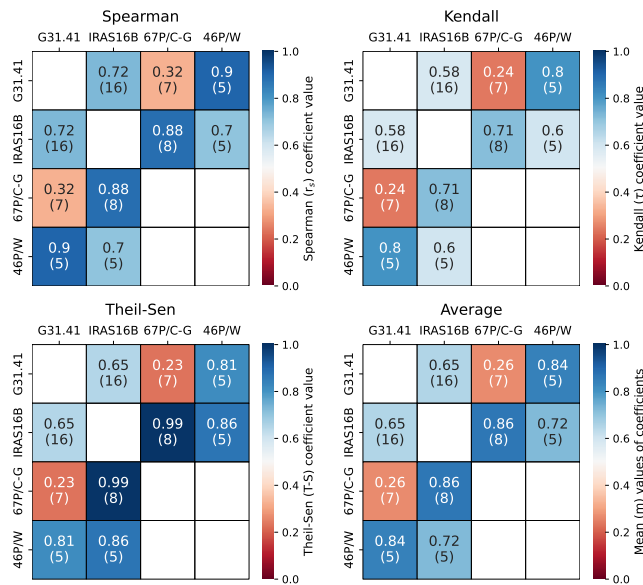


Figure 10. Correlation matrices for O-bearing molecules. The goodness of the correlation is color-coded, the bluer the color, the better the correlation. The value between brackets on each cell is the number of molecules considered.

species correlates well in general. As shown in the upper panels of Fig. 13, most of the abundance ratios with respect to CH_3OH and CH_3CN , respectively, are consistent within one order of magnitude in the four sources. This might imply that the molecular abundance ratios of O- and N-bearing species are set at early evolutionary stages of star formation, and that the subsequent evolution does not significantly alter them by a factor larger than one order of magnitude, as shown in Fig. 13. This is consistent with previous works that compared comets with several interstellar sources (Bockelée-Morvan et al. 2000; Bianchi et al. 2019; Drozdovskaya et al. 2019; Coletta

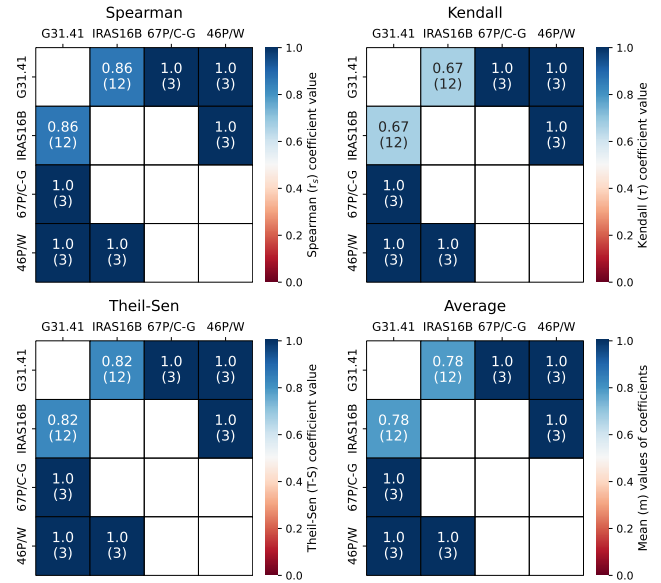


Figure 11. Correlation matrices for N-bearing molecules. The goodness of the correlation is color-coded, the bluer the color, the better the correlation. The value between brackets on each cell is the number of molecules considered.

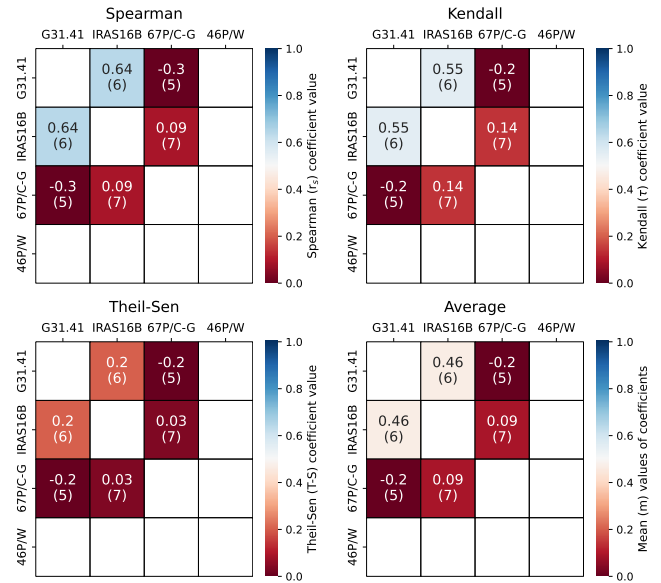


Figure 12. Correlation matrices for S-bearing molecules. The goodness of the correlation is color-coded, the bluer the color, the better the correlation. The value between brackets on each cell is the number of molecules considered.

et al. 2020), supporting the idea of chemical heritage of these chemical families during the different phases of star and planet formation.

We note that this does not imply that all molecular abundance ratios remain completely fixed and unaltered during the process of star and planet formation. It is known that some molecular ratios can vary when comparing sources at different evolutionary stages. For instance, Sabatini et al. (2021), using observations and predictions from chemical models of a large sample of massive star-forming clumps, found that while the median abundances of some species remain almost constant (H_2CO or CH_3OH), those of other species (CH_3CN or CH_3CCH) change by less than one order of magnitude.

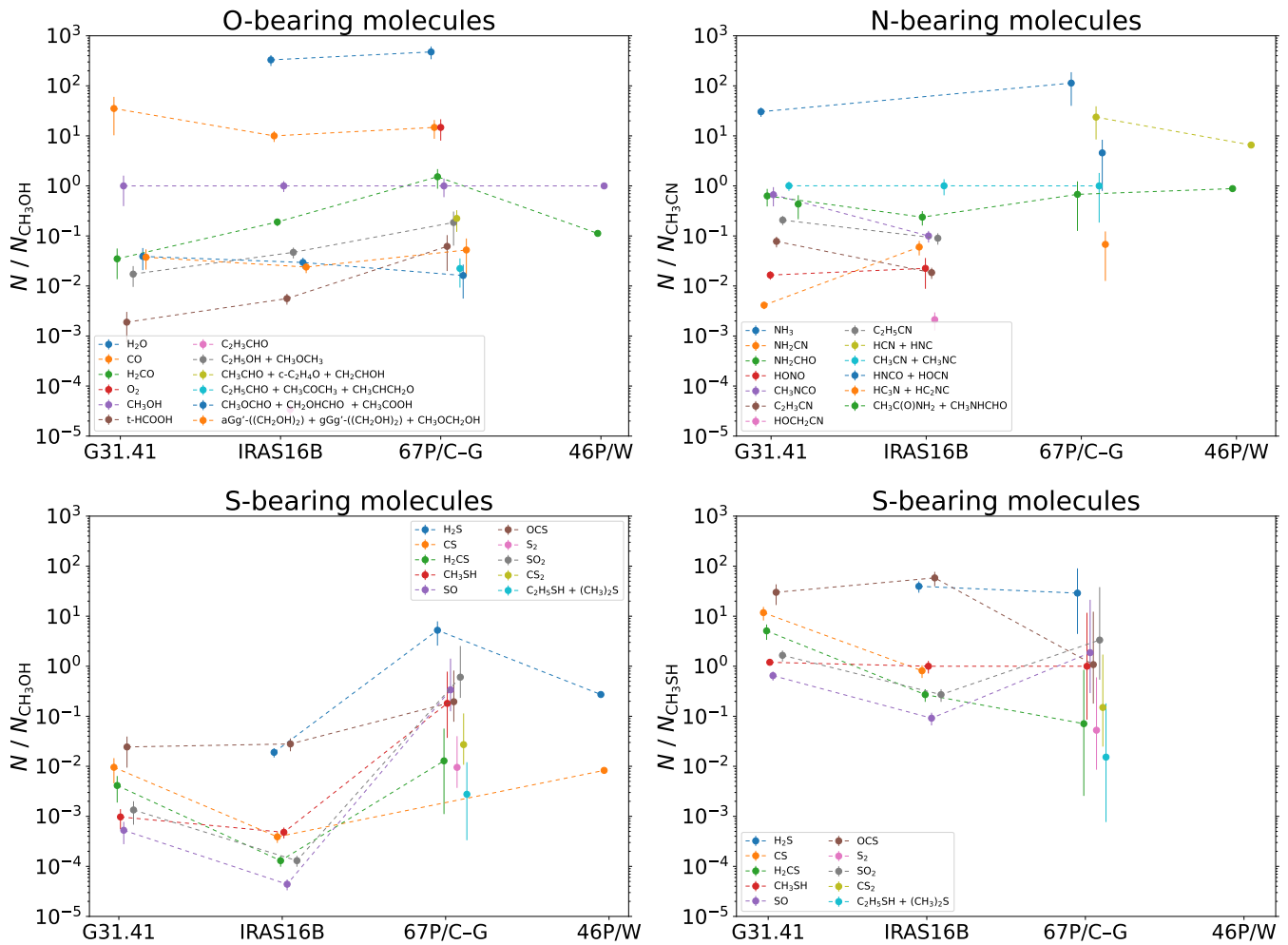


Figure 13. Comparison of the molecular abundances of the different molecules detected towards the four astronomical sources analyzed in this work. Upper panels show the column densities of detected molecules of O- and N- bearing molecules with respect to CH_3OH and CH_3CN respectively. On the lower panels S-bearing are represented with respect to CH_3OH (left) and CH_3SH (right).

Urquhart et al. (2019) considered up to 120 line intensity ratios (which can be used as an approximate proxy of abundance ratios) towards massive clumps at different stages, and found that 13 of them show some trends with evolutionary stage (see their Fig. 20). The ratios change only by a factor of ~ 2 – 4 at most, with only a couple of exceptions, for which the factor is >5 . These variations are in agreement with the results found in our analysis for the molecular ratios for N- and O-bearing species, when comparing the two star-forming regions (low and high-mass) and the two comets. Although a few species appear as outliers, as discussed in Section 5, most of the molecular ratios are in general well correlated in the four sources analyzed, with variations less than one order of magnitude (see Figs. 6, 7 and 13).

Regarding S- and P-bearing species, clear differences were observed between the star-forming regions and the comets, as already mentioned in Sect. 5. The two lower panels of Fig. 13 are very illustrative of the behaviour of the S-bearing family. The abundance ratios with respect to CH_3OH (lower left panel) have significantly higher values in 67P/C-G than in the two star-forming regions by 1–2 orders of magnitude (factors of 7–377). However, once normalized with CH_3SH (lower right panel), the molecular abundance ratios in

67P/C-G are very similar to those of the two star-forming regions (CH_3SH was not detected towards 46P/W).

The thiol/alcohol ratio $\text{CH}_3\text{SH}/\text{CH}_3\text{OH}$ is 0.18 in 67P/C-G. This value is three orders of magnitude higher than those derived in G31.41 and IRAS16B: $(8\pm 4)\times 10^{-4}$ and $(4.8\pm 0.8)\times 10^{-4}$, respectively. This suggests an overabundance of S-bearing species, compared to O-bearing, in the comet 67P/C-G. This is in good agreement with the high S/O ratio of 0.015 found by Calmonte et al. (2016) in the coma of 67P/C-G, and in the comet C/1995 O1 Hale-Bopp of 0.02 (Bockelée-Morvan et al. 2000). Both values are very close to the cosmic abundance S/O ratio measured from solar photospheric abundances (Anders & Grevesse 1989; Lodders 2010). As discussed in Calmonte et al. (2016), this strongly suggests that S is not depleted in these comets, in contrast to the results usually found in dense clouds and star-forming regions (Gondhalekar 1985; Jiménez-Escobar & Muñoz Caro 2011; Laas & Caselli 2019; Fuente et al. 2023), like G31.41 and IRAS16B. This means that in star-forming regions most of the sulfur is trapped in ice grains, since S-bearing species are more refractory than O- and N-bearing species, and thus they are not easily thermally desorbed into the gas phase in the hot cores/corinos present in high- and low-mass star-forming regions, respectively. In contrast, the results found in comets indicate that these S-bearing

species can escape the surface, and hence we can have access to the refractory S-bearing content.

A similar behaviour is also observed for P-bearing species, which are also thought to have a refractory character. In this work, we have not performed the statistical tests for P-bearing molecules because only a single species, phosphorus monoxide (PO), has been detected towards only one of the sources considered, the comet 67P/C-G (Rivilla et al. 2020). The derived P/O ratio is $(0.5-2.7)\times 10^{-4}$, close to the solar value of $\sim 6\times 10^{-4}$, which indicates that P, similarly to S, is only slightly or not depleted. In contrast, the middle upper and left lower panels of Fig. 8 show that the PO upper limits derived towards G31.41 (this work) and IRAS16B (Drozdovskaya et al. 2019) are below the 1:1 line, indicating that this species is underabundant in the gas phase of star-forming regions compared to the 67P/C-G comet, similarly to the S-bearing species.

Indeed, P-bearing molecules are not detected in hot cores (Rivilla et al. 2020) or hot corinos (Bergner et al. 2022). The interferometric high-angular resolution of these works has shown that the emission of P-bearing molecules (PN and PO) does not arise from the hot gas surrounding the protostars, but from more distant gas affected by shocks, which are able to sputter the grains and release the P content of their surfaces. Very recently, Fontani et al. (2024) have confirmed that PN, and tentatively PO, are indeed detected in shocked gas associated with molecular outflows powered by the protostars embedded in the G31.41 cluster.

Finally, we note that the analysis performed here presents evident caveats that need to be addressed in the near future. We have considered the molecular ratios of only four sources (two star-forming regions and two comets), whose chemical composition is very well known. This has allowed to study tens of different molecular ratios, but with poor statistics in terms of number of sources. Therefore, we stress that it is mandatory to perform unbiased and sensitive spectral surveys towards large samples of low- and high-mass star-forming regions. This will allow an extensive analysis of their full chemical census, including tens of molecules, like the ones done for G31.41 and IRAS16B by the GUAPOS and PILS survey, respectively. This will complement previous efforts that have been focused on a handful of selected species towards large samples of hot corinos (e.g. Bouvier et al. 2021 or Yang et al. 2021), and hot cores (e.g. Chen et al. 2023).

Moreover, there is still a key step in the process of star and planet formation whose chemical content is largely unknown: the planet-forming disk phase. Numerous efforts have been done in the last years (e.g. Banzatti et al. 2020; Grant et al. 2021; Pegues et al. 2021; Booth et al. 2021; Brunken et al. 2022), including the detection of complex molecules (Brunken et al. 2022; Tabone et al. 2023), which have suggested a direct inheritance between protoplanetary disks and previous phases e.g. (Booth et al. 2021). However, the number of species detected in these objects, which are the cradles of new planets, is still low compared with the ISM census (see McGuire 2022). Hence, direct comparisons based on a large sample of molecules, like the ones done in this work, are not possible yet, and should be addressed in the forthcoming years. As well, current and future space *in-situ* and sample-return missions, targeting new comets and asteroids, like the on-going JAXA Hayabusa2 mission to the asteroid Ryugu (e.g. Potiszil et al. 2023), or the OSIRIS-REx mission to the asteroid Bennu (Lauretta et al. 2017), will significantly widen our current view of the chemical ingredient of Solar System objects, and thus they will allow us to attain a complete view of the chemical thread during the whole evolution of planetary systems.

7 SUMMARY AND CONCLUSIONS

In this work we provide a comprehensive view of the chemical feedstock of the massive star-forming protocluster G31.41+0.31. We have analyzed the emission of 34 molecules using data from the GUAPOS project (G31.41+0.31 Unbiased ALMA sPectral Observational Survey). We have derived the column densities and abundances of 18 molecular species, including 25 isotopologues and 3 tentative detections (HONO, C₂H₅CHO and CH₃OCH₂OH). For the 16 molecules not detected, we derived column density upper limits. We have added these molecules to those already reported in previous GUAPOS works, to compile a total molecule sample of 57 species. Then, we have performed a comparative study of the G31.41 molecular abundance ratios with those of sources that represent different evolutionary stages of star formation, from the protostellar stage to Solar System objects: the prototypical Solar-like protostar (IRAS 16293-2422 B), and two comets (67P/Churyumov-Gerasimenko and 46P/Wirtanen). To quantitatively study the correlation between the chemical content of the sources we performed three complementary statistical tests: Spearman, Kendall and Theil-Sen. Our results shows that the molecular abundances of the two star-forming regions, G31.41 (high-mass) and IRAS16B (low-mass), are in general well correlated, including O-, N- and S-bearing species. This similarity, based on a large sample of molecules, denotes that molecular abundance ratios do not vary by factors larger than one order of magnitude, despite of the very different physical properties of these two high- and low-mass star-forming regions, such as the mass or the luminosity, level of clustering, protostellar feedback, UV radiation, evolution timescales, or location within the Galaxy.

The comparison with the two comets (67P/C-G and 46P/W) shows that their O- and N-bearing molecular abundance ratios are also well correlated with those of the star-forming regions. This suggests that the abundances ratios of these chemical families are primarily set at initial phases of star formation, and subsequently inherited without variations larger than one order of magnitude during the process of star and planet formation. However, the S-bearing molecules behave differently, being significantly more abundant in 67P/C-G and 46P/W than in the gas phase of star-forming regions. This result can be explained in terms of sulfur-depletion in the ISM, namely that sulfur is trapped on the icy surfaces of dust grains. On the contrary, S-bearing species are believed to have been freely desorbed into the coma of the comets, recovering the expected cosmic abundance. A similar behaviour is also suggested for P, based on the PO detection in the comet 67P/C-G, and the upper limits derived in the two star-forming regions.

ACKNOWLEDGEMENTS

We thank the anonymous referee for a careful reading of the article and her/his useful comments. The figures showing the molecular spectra of G31.41 and the table of molecular transitions were made thanks to a code created by Andrés Megías (Github: <https://github.com/andresmegias/madcubaslim-scripts>) and the Python library *richvalues*, respectively. We thank to Miguel Sanz-Novo for the help regarding the quantum numbers of each molecule. We also thank to M. Drozdovskaya for some discussion about the IRAS16B molecular abundances. This paper makes use of the following ALMA data: ADS/JAO.ALMA#2017.1.00501.S. ALMA is a partnership of ESO (representing its member states), NSF (USA) and NINS (Japan), together with NRC (Canada), MOST and ASIAA (Taiwan), and KASI

(Republic of Korea), in cooperation with the Republic of Chile. The Joint ALMA Observatory is operated by ESO, AUI/NRAO and NAOJ. A. L.-G. and V.M.R. have received support from the Comunidad de Madrid through the Atracción de Talento Investigador Modalidad I (Doctores con experiencia) Grant (COOL: Cosmic Origins Of Life; 2019-T1/TIC-5379), the project RYC2020-029387-I funded by MICIU/AEI/10.13039/501100011033 and by “ESF, Investing in your future”, from the the Consejo Superior de Investigaciones Científicas (CSIC) and the Centro de Astrobiología (CAB) through the project 20225AT015 (Proyectos intramurales especiales del CSIC), and from the Spanish Ministry of Science through the project PID2022-136814NB-I00. L.C. and I.J.-S. acknowledge financial support through the Spanish grants PID2019-105552RB-C41 and PID2022-136814NB-I00 from the Spanish Ministry of Science and Innovation/State Agency of Research MICIU/AEI/10.13039/501100011033 and by “ERDF A way of making Europe”. C.M. acknowledges funding from the European Research Council (ERC) under the European Union’s Horizon 2020 program through the ECOGAL Synergy grant (ID 855130). A.S.-M. acknowledges support from the RyC2021-032892-I and PID2020-117710GB-I00 grants funded by MICIU/AEI/10.13039/501100011033 and by the European Union ‘Next GenerationEU’/PRTR, as well as the program Unidad de Excelencia María de Maeztu CEX2020-001058-M. S.V. acknowledges support from the European Research Council (ERC) grant MOPPEX ERC-833460.

DATA AVAILABILITY

The data presented in this work are available upon reasonable request.

REFERENCES

- Adams F. C., 2010, *ARA&A*, **48**, 47
- Altwegg K., et al., 2016, *Science Advances*, **2**, e1600285
- Altwegg K., et al., 2017, *Philosophical Transactions of the Royal Society of London Series A*, **375**, 20160253
- Altwegg K., Balsiger H., Fuselier S. A., 2019, *ARA&A*, **57**, 113
- Anders E., Grevesse N., 1989, *Geochimica Cosmochimica Acta*, **53**, 197
- Awad Z., Viti S., Collings M. P., Williams D. A., 2010, *MNRAS*, **407**, 2511
- Banzatti A., et al., 2020, *ApJ*, **903**, 124
- Beltrán M. T., Codella C., Viti S., Neri R., Cesaroni R., 2009, *ApJ*, **690**, L93
- Beltrán M. T., et al., 2018, *A&A*, **615**, A141
- Beltrán M. T., et al., 2021, *A&A*, **648**, A100
- Bergner J. B., Burkhardt A. M., Öberg K. I., Rice T. S., Bergin E. A., 2022, *ApJ*, **927**, 7
- Bianchi E., et al., 2019, *MNRAS*, **483**, 1850
- Biver N., et al., 2021, *A&A*, **648**, A49
- Bockelée-Morvan D., et al., 2000, *A&A*, **353**, 1101
- Bonato M., et al., 2018, *MNRAS*, **478**, 1512
- Booth A. S., Walsh C., Terwisscha van Scheltinga J., van Dishoeck E. F., Ilee J. D., Hogerheijde M. R., Kama M., Nomura H., 2021, *Nature Astronomy*, **5**, 684
- Bouvier M., López-Sepulcre A., Ceccarelli C., Sakai N., Yamamoto S., Yang Y. L., 2021, *A&A*, **653**, A117
- Brinkman H. E., den Hartogh J. W., Doherty C. L., Pignatari M., Lugaro M., 2021, *ApJ*, **923**, 47
- Brunken N. G. C., Booth A. S., Leemker M., Nazari P., van der Marel N., van Dishoeck E. F., 2022, *A&A*, **659**, A29
- Calcutt H., et al., 2018, *A&A*, **616**, A90
- Calcutt H., et al., 2019, *A&A*, **631**, A137
- Calmonte U., et al., 2016, *MNRAS*, **462**, S253
- Carpenter J. M., 2000, *AJ*, **120**, 3139
- Ceccarelli C., et al., 2023, in Inutsuka S., Aikawa Y., Muto T., Tomida K., Tamura M., eds, *Astronomical Society of the Pacific Conference Series* Vol. 534, *Astronomical Society of the Pacific Conference Series*. p. 379
- Cesaroni R., 2019, *A&A*, **631**, A65
- Cesaroni R., Churchwell E., Hofner P., Walmsley C. M., Kurtz S., 1994, *A&A*, **288**, 903
- Chen Y., et al., 2023, *A&A*, **678**, A137
- Cleeves L. I., Bergin E. A., Alexander C. M. O. D., Du F., Graninger D., Öberg K. I., Harries T. J., 2014, *Science*, **345**, 1590
- Coletta A., Fontani F., Rivilla V. M., Mininni C., Colzi L., Sánchez-Monge Á., Beltrán M. T., 2020, *A&A*, **641**, A54
- Colzi L., Fontani F., Rivilla V. M., Sánchez-Monge A., Testi L., Beltrán M. T., Caselli P., 2018, *MNRAS*, **478**, 3693
- Colzi L., et al., 2021, *A&A*, **653**, A129
- Coutens A., et al., 2018, *A&A*, **612**, A107
- Coutens A., et al., 2019, *A&A*, **623**, L13
- Dhooghe F., et al., 2017, *MNRAS*, **472**, 1336
- Dickman R. L., 1978, *ApJS*, **37**, 407
- Drozhdovskaya M. N., van Dishoeck E. F., Rubin M., Jørgensen J. K., Altwegg K., 2019, *MNRAS*, **490**, 50
- Duan Y., Li D., Pagani L., Goldsmith P. F., Ching T.-C., Wang C., Xie J., 2023, *Research in Astronomy and Astrophysics*, **23**, 095006
- Dukes D., Krumholz M. R., 2012, *ApJ*, **754**, 56
- Endres C. P., Schlemmer S., Schilke P., Stutzki J., Müller H. S. P., 2016, *Journal of Molecular Spectroscopy*, **327**, 95
- Fayolle E. C., et al., 2017, *Nature Astronomy*, **1**, 703
- Fontani F., et al., 2024, *A&A*, **682**, A74
- Fuente A., et al., 2023, *A&A*, **670**, A114
- García de la Concepción J., et al., 2022, *A&A*, **658**, A150
- Gondhalekar P. M., 1985, *MNRAS*, **217**, 585
- Grant S. L., et al., 2021, *ApJ*, **913**, 123
- Hacar A., Bosman A. D., van Dishoeck E. F., 2020, *A&A*, **635**, A4
- Hadraoui K., et al., 2019, *A&A*, **630**, A32
- Herbst E., van Dishoeck E. F., 2009, *ARA&A*, **47**, 427
- Immer K., Li J., Quiroga-Núñez L. H., Reid M. J., Zhang B., Moscadelli L., Rygl K. L. J., 2019, *A&A*, **632**, A123
- Jacobsen S. K., et al., 2018, *A&A*, **612**, A72
- Jiménez-Escobar A., Muñoz Caro G. M., 2011, *A&A*, **536**, A91
- Jørgensen J. K., et al., 2016, *A&A*, **595**, A117
- Jørgensen J. K., et al., 2018, *A&A*, **620**, A170
- Korschinek G., Faestermann T., Poutivtsev M., Arazi A., Knie K., Rugel G., Wallner A., 2020, *Phys. Rev. Lett.*, **125**, 031101
- Laas J. C., Caselli P., 2019, *A&A*, **624**, A108
- Lada C. J., Lada E. A., 2003, *ARA&A*, **41**, 57
- Lauretta D. S., et al., 2017, *Space Sci. Rev.*, **212**, 925
- Le Roy L., et al., 2015, *A&A*, **583**, A1
- Ligterink N. F. W., et al., 2017, *MNRAS*, **469**, 2219
- Ligterink N. F. W., Terwisscha van Scheltinga J., Taquet V., Jørgensen J. K., Cazaux S., van Dishoeck E. F., Linnartz H., 2018, *MNRAS*, **480**, 3628
- Lis D. C., Goldsmith P. F., 1988, in Dickman R. L., Snell R. L., Young J. S., eds., Vol. 315, *Molecular Clouds, Milky-Way and External Galaxies*. p. 191, doi:10.1007/3-540-50438-9_266
- Lodders K., 2010, in *Principles and Perspectives in Cosmochemistry*. p. 379 (arXiv:1010.2746), doi:10.1007/978-3-642-10352-0_8
- Loomis R. A., Cleeves L. I., Öberg K. I., Aikawa Y., Bergner J., Furuya K., Guzman V. V., Walsh C., 2018, *ApJ*, **859**, 131
- Lykke J. M., et al., 2017, *A&A*, **597**, A53
- Manigand S., et al., 2020, *A&A*, **635**, A48
- Manigand S., et al., 2021, *A&A*, **645**, A53
- Martín-Doménech R., Rivilla V. M., Jiménez-Serra I., Quénard D., Testi L., Martín-Pintado J., 2017, *MNRAS*, **469**, 2230
- Martín S., Martín-Pintado J., Blanco-Sánchez C., Rivilla V. M., Rodríguez-Franco A., Rico-Villas F., 2019, *A&A*, **631**, A159
- Mauersberger R., Henkel C., Langer N., Chin Y. N., 1996, *A&A*, **313**, L1
- Maureira M. J., Pineda J. E., Segura-Cox D. M., Caselli P., Testi L., Lodato G., Loinard L., Hernández-Gómez A., 2020, *ApJ*, **897**, 59
- McGuire B. A., 2022, *ApJS*, **259**, 30
- McGuire B. A., et al., 2017, *ApJ*, **851**, L46

- McMullin J. P., Waters B., Schiebel D., Young W., Golap K., 2007, in Shaw R. A., Hill F., Bell D. J., eds, *Astronomical Society of the Pacific Conference Series Vol. 376, Astronomical Data Analysis Software and Systems XVI*, p. 127
- Milam S. N., Savage C., Brewster M. A., Ziurys L. M., Wyckoff S., 2005, *ApJ*, **634**, 1126
- Mininni C., et al., 2020, *A&A*, **644**, A84
- Mininni C., et al., 2023, *A&A*, **677**, A15
- Müller H. S. P., Thorwirth S., Roth D. A., Winnewisser G., 2001, *A&A*, **370**, L49
- Müller H. S. P., Schlöder F., Stutzki J., Winnewisser G., 2005, *Journal of Molecular Structure*, **742**, 215
- Nazari P., et al., 2021, *A&A*, **650**, A150
- Nazari P., et al., 2022, *A&A*, **668**, A109
- Öberg K. I., Boogert A. C. A., Pontoppidan K. M., van den Broek S., van Dishoeck E. F., Bottinelli S., Blake G. A., Evans Neal J. I., 2011, *ApJ*, **740**, 109
- Öberg K. I., Guzmán V. V., Furuya K., Qi C., Aikawa Y., Andrews S. M., Loomis R., Wilner D. J., 2015, *Nature*, **520**, 198
- Orosio M., Anglada G., Lizano S., D'Alessio P., 2009, *ApJ*, **694**, 29
- Pegues J., et al., 2021, *ApJ*, **911**, 150
- Pfalzner S., Vincke K., 2020, *ApJ*, **897**, 60
- Pickett H. M., Poynter R. L., Cohen E. A., Delitsky M. L., Pearson J. C., Müller H. S. P., 1998, *J. Quant. Spectrosc. Radiative Transfer*, **60**, 883
- Porras A., Christopher M., Allen L., Di Francesco J., Megeath S. T., Myers P. C., 2003, *AJ*, **126**, 1916
- Potaszil C., et al., 2023, *Nature Communications*, **14**, 1482
- Reach W. T., et al., 2009, *ApJ*, **690**, 683
- Rivilla V. M., Beltrán M. T., Cesaroni R., Fontani F., Codella C., Zhang Q., 2017, *A&A*, **598**, A59
- Rivilla V. M., et al., 2020, *MNRAS*, **492**, 1180
- Rubin M., et al., 2019, *MNRAS*, **489**, 594
- Sabatini G., et al., 2021, *A&A*, **652**, A71
- Sánchez-Monge Á., Schilke P., Ginsburg A., Cesaroni R., Schmiedeke A., 2018, *A&A*, **609**, A101
- Schuhmann M., et al., 2019, *ACS Earth and Space Chemistry*, **3**, 1854
- Suzuki T., et al., 2023, *ApJ*, **954**, 189
- Tabone B., et al., 2023, *Nature Astronomy*, **7**, 805
- Tercero B., Cuadrado S., López A., Brouillet N., Despois D., Cernicharo J., 2018, *A&A*, **620**, L6
- Tobin J. J., et al., 2023, *Nature*, **615**, 227
- Urquhart J. S., et al., 2019, *MNRAS*, **484**, 4444
- Visser R., van Dishoeck E. F., Black J. H., 2009, *A&A*, **503**, 323
- Viti S., Collings M. P., Dever J. W., McCoustra M. R. S., Williams D. A., 2004, *MNRAS*, **354**, 1141
- Wilson T. L., 1999, *Reports on Progress in Physics*, **62**, 143
- Yan Y. T., et al., 2019, *ApJ*, **877**, 154
- Yang Y.-L., et al., 2021, *ApJ*, **910**, 20
- Yu H. Z., et al., 2020, *ApJ*, **899**, 145
- Zeng S., Quénard D., Jiménez-Serra I., Martín-Pintado J., Rivilla V. M., Testi L., Martín-Doménech R., 2019, *MNRAS*, **484**, L43
- van Gelder M. L., et al., 2020, *A&A*, **639**, A87
- van der Marel N., Booth A. S., Leemker M., van Dishoeck E. F., Ohashi S., 2021, *A&A*, **651**, L5

APPENDIX A: SLIM FITS OF OTHER ISOTOPOLOGUES

Table A1: Results of the SLIM fits of the isotopologues of the molecules analysed towards G31.41 that were not used to derive the abundances of the main isotopologues, ordered by increasing molecular mass. The resulting physical parameters, along with their associated uncertainties, are presented. The values of the parameters fixed to perform some fits are shown without uncertainties. In the case of non detections, we indicated the upper limit in the column density with $<$. When T_{ex} is fixed, we calculate in what factor the value of N changes when using the different temperatures T_{min} and T_{max} : 25-75 K and 100-200 K for fixed temperatures of 50 K and 150 K, respectively. We also present the maximum line opacity of the transitions of each molecule (τ_{max}). The transitions used to obtain these values are in Table D1.

Formula	T_{ex} (K)	N ($\times 10^{16} \text{ cm}^{-2}$)	$N(T_{\text{min}})/N$ - $N(T_{\text{max}})/N$	$\nu - \nu_0$ (km s^{-1})	FWHM (km s^{-1})	τ_{max}^a	Fig.
Detected molecules							
C^{17}O	50	<5	0.7-1.6	0	7	0.02	F2
C^{18}O	50	14 ± 5	0.7-1.4	0	7	0.15 ± 0.10	F2
H_2CO	50	62 ± 22	3.8-0.6	0.8 ± 0.4	7.4 ± 1.0	4 ± 14	F3
H_2^{13}CO	50	3.0 ± 0.4	2.2-1.0	1.4 ± 0.4	6.3 ± 0.9	0.24 ± 0.05	F3
$\text{H}_2\text{C}^{17}\text{O}$	50	4.9 ± 1.3	2.8-1.0	0	7	0.4 ± 0.3	F3
^{13}CS	50	1.21 ± 0.14	1.0-1.0	1.2 ± 0.3	7.7 ± 0.5	2.5 ± 1.0	2
$^{13}\text{C}^{34}\text{S}$	50	0.23 ± 0.02	0.7-1.3	-2.0 ± 0.5	11.3 ± 1.2	0.32 ± 0.06	2
C^{34}S	50	0.64 ± 0.04	2.7-1.2	0.8 ± 0.3	9.5 ± 0.5	1.17 ± 0.18	2
C^{33}S	50	0.56 ± 0.07	3.4-1.2	1.8 ± 0.6	9.5	1.0 ± 0.4	2
H_2CS	38.3 ± 1.2	9.9 ± 1.5		0.6 ± 0.2	5.1 ± 0.2	>10	F6
H_2^{13}CS	50	0.17 ± 0.04	0.6-1.7	1.4 ± 0.9	7	0.10 ± 0.05	F6
$\text{H}_2\text{C}^{34}\text{S}$	50	0.58 ± 0.05	0.6-1.4	1.7 ± 0.4	7	0.33 ± 0.07	F6
SO	50	3.5 ± 0.3	2.0-1.0	1.0 ± 0.3	8.6 ± 0.6	2.2 ± 1.2	F8
HC_3N	58 ± 8	0.55 ± 0.06		1.5 ± 0.2	11.0 ± 0.7	2.0 ± 1.1	F9
OCS	74 ± 5	18.7 ± 1.3		0.95 ± 0.09	7.4 ± 0.3	2.8 ± 1.3	F11
O^{13}CS	35 ± 16	2.0 ± 0.3		1.3 ± 0.3	5.9 ± 0.8	1.1 ± 1.0	F11
OC^{34}S	50	4.8 ± 0.4	1.8-1.2	0.8 ± 0.2	6.6 ± 0.5	1.4 ± 0.4	F11
OC^{33}S	50	0.7 ± 0.1	0.6-0.8	2.1 ± 0.5	6.9 ± 1.0	0.22 ± 0.06	F11
SO_2	56	4.4 ± 0.3	1.6-1.2	0.3 ± 0.4	10.6 ± 0.8	0.64 ± 0.15	F13
$^{33}\text{SO}_2$	56	1.7 ± 0.2	0.4-1.3	2.7 ± 0.6	8.8 ± 1.5	0.08 ± 0.04	F13

Notes. ^a Maximum τ of all the transitions detected in each species.

APPENDIX B: SAMPLE OF MOLECULES USED FOR COMPARISONS BETWEEN SOURCES

The complete list of molecules used in this work (detections, tentative detections and upper limits) is given in Table B1 for the four sources used in this work (G31.41, IRAS16B, 67P/C-G and 46P/W). The species are ordered by increasing molecular mass.

Table B1: Molecules used in this work. Molecules with a [✓] implies that they are detected; [~ ✓] indicates a tentative detection; and [<] denotes non detections. The molecules indicated with * in the 67P/C-G column are members of isomeric groups

Formula	Name	Mol. mass	G31.41	IRAS16B	67P/C-G	46P/W
NH_3	Ammonia	17	✓ ^a	< ^f	✓ ^f	-
H_2O	Water	18	-	✓ ^f	✓ ^f	-
HCN	Hydrogen cyanide	27	✓ ^e	✓ ^f	✓* ^f	✓ ^p
HNC	Hydrogen isocyanide	27	< ^e	< ^f	✓* ^f	✓ ^p
CO	Carbon monoxide	28	✓ ^e	✓ ^f	✓ ^f	< ^p
H_2CO	Formaldehyde	30	✓ ^e	✓ ^f	✓ ^f	✓ ^p
O_2	Molecular oxygen	32	-	< ^f	✓ ^f	-
CH_3OH	Methanol	32	✓ ^d	✓ ^f	✓ ^f	✓ ^p
H_2S	Hydrogen sulphide	34	< ^e	✓ ^f	✓ ^f	✓ ^p
HCl	Hydrogen chloride	34	-	< ^f	✓ ^f	-
CH_3CCH	Propyne	34	✓ ^e	✓ ⁱ	-	-
CH_3CN	Methyl cyanide	41	✓ ^d	✓ ^f	✓* ^f	✓ ^p
CH_3NC	Methyl isocyanide	41	✓ ^e	✓ ^f	✓* ^f	-
NH_2CN	Cyanamide	42	✓ ^e	✓ ^j	-	-

Table B1: Continued.

Formula	Name	Mol. mass	G31.41	IRAS16B	67P/C-G	46P/W
C ₃ H ₆	Propylene/Propene	42	< ^e	✓ ^l	-	-
HNCO	Isocyanic acid	43	✓ ^c	✓ ^f	✓* ^f	< ^p
HOCN	Cyanic acid	43	< ^e	< ^f	✓* ^f	-
CS	Carbon monosulphide	44	✓ ^e	✓ ^f	-	✓ ^p
CH ₃ CHO	Acetaldehyde	44	✓ ^d	✓ ^f	✓* ^f	✓ ^p
c-C ₂ H ₄ O	Ethylene oxide	44	✓ ^e	✓ ^f	✓* ^f	< ^p
syn-CH ₂ CHOH	Vinyl alcohol	44	< ^e	< ^f	✓* ^f	-
NH ₂ CHO	Formamide	45	✓ ^c	✓ ^f	✓ ^f	✓ ^p
PN	Phosphorus mononitride	45	< ^e	< ^f	< ^f	< ^p
H ₂ CS	Thioformaldehyde	46	✓ ^e	✓ ^f	✓ ^f	< ^p
C ₂ H ₅ OH	Ethanol	46	✓ ^d	✓ ^f	✓* ^f	✓ ^p
CH ₃ OCH ₃	Dimethyl ether	46	✓ ^d	✓ ^f	✓* ^f	< ^p
trans-HCOOH	Formic acid	46	✓ ^h	✓ ^f	✓ ^f	< ^p
trans-HONO	Nitrous acid	47	~ ✓ ^e	✓ ^k	-	-
PO	Phosphorus monoxide	47	< ^e	< ^f	✓ ^f	< ^p
CH ₃ SH	Methyl mercaptan	48	✓ ^e	✓ ^f	✓ ^f	< ^p
SO	Sulphur monoxide	48	✓ ^e	✓ ^f	✓ ^f	< ^p
CH ₃ Cl	Methyl chloride	50	< ^e	✓ ^f	✓ ^f	-
HC ₃ N	Cyanoacetylene	51	✓ ^e	✓ ^f	✓* ^f	< ^p
HC ₂ NC	Isocyanoacetylene	51	< ^e	-	✓* ^f	-
trans-C ₂ H ₃ CHO	Propenal	56	< ^e	✓ ^l	-	-
CH ₃ NCO	Methyl isocyanate	57	✓ ^c	✓ ^m	-	-
C ₂ H ₃ CN	Vinyl cyanide	57	✓ ^d	✓ ^h	-	< ^p
HOCH ₂ CN	Glycolonitrile	57	< ^e	✓ ⁿ	-	-
C ₂ H ₅ CHO	Propanal	58	~ ✓ ^e	✓ ^f	✓* ^f	-
CH ₃ COCH ₃	Acetone	58	✓ ^d	✓ ^f	✓* ^f	< ^p
CH ₃ CHCH ₂ O	Propylene oxide	58	< ^e	-	✓* ^f	-
CH ₃ C(O)NH ₂	Acetamide	59	✓ ^c	✓ ^o	-	-
CH ₃ NHCHO	N-Methylformamide	59	✓ ^c	< ^o	-	-
C ₂ H ₅ CN	Ethyl cyanide	59	✓ ^d	✓ ^h	-	< ^p
OCS	Carbonyl sulphide	60	✓ ^e	✓ ^f	✓ ^f	< ^p
CH ₃ OCHO	Methyl formate	60	✓ ^b	✓ ^f	✓* ^f	< ^p
CH ₂ OHCHO	Glycoaldehyde	60	✓ ^b	✓ ^f	✓* ^f	< ^p
CH ₃ COOH	Acetic acid	60	✓ ^b	✓ ^f	✓* ^f	< ^p
gauche-C ₂ H ₅ SH	Ethyl mercaptan	62	< ^e	< ^f	✓ ^f	-
aGg'-(CH ₂ OH) ₂	aGg' - Ethylene glycol	62	✓ ^d	✓ ^f	✓* ^f	✓ ^p
gGg'-(CH ₂ OH) ₂	gGg' - Ethylene glycol	62	✓ ^d	✓ ^f	✓* ^f	-
CH ₃ OCH ₂ OH	Methoxymethanol	62	~ ✓ ^e	✓ ^f	✓* ^f	-
S ₂	Disulphur	64	< ^e	< ^f	✓ ^f	-
SO ₂	Sulphur dioxide	64	✓ ^e	✓ ^f	✓ ^f	< ^p
HS ₂	Disulphanide	65	< ^e	< ^f	< ^f	-
H ₂ S ₂	Disulphane	66	< ^e	< ^f	< ^f	-
NH ₂ CH ₂ COOH	Glycine (conf. I)	75	< ^e	< ^f	✓ ^f	< ^p

References. a) Cesaroni et al. (1994); b) Mininni et al. (2020); c) Colzi et al. (2021); d) Mininni et al. (2023); e) This work; f) Drozdovskaya et al. (2019) and references therein; g) García de la Concepción et al. (2022); h) Calcutt et al. (2018); i) Calcutt et al. (2019); j) Coutens et al. (2018); k) Coutens et al. (2019); l) Manigand et al. (2021); m) Martín-Doménech et al. (2017); n) Zeng et al. (2019); o) Ligterink et al. (2018); p) Biver et al. (2021).

APPENDIX C: SPECTROSCOPIC CATALOG ENTRIES

Table C1 lists the spectroscopic catalog entries of all the molecules analysed in this work towards G31.41. The species are ordered by increasing molecular mass.

Table C1: Spectroscopic entries used to perform the analysis, including the molecular catalog, tag of the species, version number, and date of the version.

Formula	Name	Mol. mass	Catalogue	Tag	Version	Date version
Detected molecules						
HCN	Hydrogen cyanide	27	CDMS	27501	4	May 2007
HC ¹⁵ N			CDMS	28506	2	Dec. 2017
C ¹⁸ O			CDMS	30502	1	June 2001
¹³ C ¹⁸ O			CDMS	31502	1	July 2000
H ₂ CO	Formaldehyde	30	CDMS	30501	3	Feb. 2017
H ₂ ¹³ CO			CDMS	31503	1	May 2000
H ₂ C ¹⁷ O			CDMS	31514	1	Feb. 2017
H ₂ C ¹⁸ O			CDMS	32503	2	Feb. 2017
CH ₃ CCH	Propyne	40	CDMS	40502	3	Aug. 2008
CH ₃ NC	Methyl isocyanide	41	CDMS	41514	1	Aug. 2018
NH ₂ CN	Cyanamide	42	JPL	42003	1	Jan. 1991
¹³ CS	Carbon monosulphide	44	CDMS	45501	2	Jan. 2004
¹³ C ³⁴ S			CDMS	47501	2	Jan. 2004
C ³⁴ S			CDMS	46501	2	Jan. 2004
C ³³ S			CDMS	45502	2	Jan. 2004
C ³⁶ S			CDMS	48503	2	Jan. 2004
c-C ₂ H ₄ O	Ethylene oxide	44	CDMS	44504	3	Mar. 2022
H ₂ CS	Thioformaldehyde	46	CDMS	42517	1	Sep. 2017
H ₂ ¹³ CS			CDMS	47505	2	Jan. 2019
H ₂ C ³³ S			CDMS	47506	2	Jan. 2019
H ₂ C ³⁴ S			CDMS	48508	2	Jan. 2019
trans-HONO	Nitrous acid	47	JPL	47007	1	Jan. 2006
SO	Sulphur monoxide	48	CDMS	48501	1	Aug. 1998
³⁴ SO			CDMS	50501	1	Aug. 1998
CH ₃ SH	Methyl mercaptan	48	CDMS	48510	2	May 2020
HC ₃ N	Cyanoacetylene	51	CDMS	51501	1	Oct. 2000
H ¹³ CCCN			CDMS	52509	1	Dec. 2004
HC ¹³ CCN			CDMS	52510	1	Dec. 2004
HCC ¹³ CN			CDMS	52511	1	Dec. 2004
C ₂ H ₅ CHO	Propanal	58	CDMS	58505	2	Jan. 2018
OCS	Carbonyl sulphide	60	CDMS	60503	2	Nov. 2005
O ¹³ CS			CDMS	61502	1	Apr. 2005
¹⁸ OCS			CDMS	62506	1	Apr. 2005
OC ³⁴ S			CDMS	62505	1	Apr. 2005
OC ³³ S			CDMS	61503	1	Apr. 2005
CH ₃ OCH ₂ OH	Methoxymethanol	62	CDMS	62527	1	Aug. 2020
SO ₂	Sulphur dioxide	64	CDMS	64502	2	July 2005
³⁴ SO ₂			CDMS	66501	1	Dec. 1999
³³ SO ₂			CDMS	65501	1	Dec. 1999
Non detected molecules (upper limits)						
H ¹⁵ NC	Hydrogen isocyanide	27	JPL	28006	1	Dec. 1979
C ¹⁷ O	Carbon monoxide	28	CDMS	29503	1	Jan. 2003
H ₂ S	Hydrogen sulphide	34	CDMS	34502	1	Oct. 2008
C ₃ H ₆	Propylene/Propene	42	CDMS	42516	1	Jan. 2017
HOCN	Cyanic acid	43	CDMS	43510	1	May. 2009
syn-CH ₂ CHOH	Vinyl alcohol	44	CDMS	44506	2	Sep. 2019
PN	Phosphorus mononitride	45	CDMS	45511	2	Sep. 2019
PO	Phosphorus monoxide	47	CDMS	47507	2	Oct. 2019
CH ₃ Cl	Methyl chloride	50	JPL	50007	3	May 2009
HC ₂ NC	Isocyanoacetylene	51	JPL	51004	1	Dec. 1994
trans-C ₂ H ₃ CHO	Propenal	56	JPL	56008	1	Jan. 1996
HOCH ₂ CN	Glycolonitrile	57	CDMS	57512	1	Mar. 2017
CH ₃ CHCH ₂ O	Propylene oxide	58	CDMS	58514	1	Jan. 2016
gauche-C ₂ H ₅ SH	Ethyl mercaptan	62	CDMS	62523	1	Sep. 2015

Table C1: Continued.

Formula	Name	Mol. mass	Catalog	TAG	Version	Date version
S ₂	Disulphur	64	JPL	64001	2	Oct. 1989
HS ₂	Disulphanide	65	CDMS	65509	1	July 2008
H ₂ S ₂	Disulphane	66	CDMS	66507	1	Dec. 2014
NH ₂ CH ₂ COOH	Glycine (conf. I)	75	CDMS	75511	1	Apr. 2006

APPENDIX D: MOLECULAR TRANSITIONS USED IN THE ANALYSIS

The transitions used for the MADCUBA fits of the molecular emission of the analysed species in this work towards G31.41+0.31 (see Table 2 and Table A1) are listed in Table D1.

Table D1: List of the transitions of the molecules analysed in this work that were used to perform the MADCUBA fits to obtain their physical parameters (see Table 2 and Table A1). Frequency is the rest frequency of the transitions in GHz; Quantum numbers indicates the quantum number used to label the rotational energy levels; $\log I$ is the logarithm of the line intensity on $\text{nm}^2 \text{ MHz}$; E_{up} is the energy of the state of higher energy in K; Area is the integrated intensity of the line in K km s^{-1} and τ is the optical depth of the transition. In case of upper limits, the transitions listed are only those used to retrieve the upper limit (see Fig G1). The quantum numbers used are: J which indicates the total angular momentum (fine structure effects imply the use of both N and J), K_a and K_c are the projections of J onto the a and c inertial axis (if the molecule is symmetric top only K is needed), ν specifies the vibrational states, ν_t is the torsional state and F designates the spin quanta. The A and E labels refers to the A- and E-symmetry states, respectively, if present. We label as 0^+ and 0^- the symmetric and antisymmetric tunneling states, respectively, if present. The molecules are in the ground state by default in this table unless specified.

Molecule	Frequency (GHz)	Quantum numbers	Transition	$\log I$ ($\text{nm}^2 \text{ MHz}$)	E_{up} (K)	Area (K km s^{-1})	τ
Detected molecules							
HC ¹⁵ N	86.05497	J	1 \rightarrow 0	-2.5525	4.1	478 \pm 6	1.7 \pm 0.2
C ¹⁸ O	109.78217	J	1 \rightarrow 0	-5.0708	5.3	49 \pm 9	0.15 \pm 0.10
¹³ C ¹⁸ O	104.71140	$J_{F+1/2}$	1 ₁ \rightarrow 0 ₁	-5.6079	5.0	29 \pm 12	0.07 \pm 0.11
¹³ C ¹⁸ O	104.71140		1 ₂ \rightarrow 0 ₁	-5.3069	5.0	56 \pm 12	0.13 \pm 0.11
H ₂ CO	89.56506	J_{K_a, K_c}	13 _{2,11} \rightarrow 13 _{2,12}	-4.7850	370	3 \pm 18	(8.0 \pm 162.7) $\cdot 10^{-3}$
H ₂ CO	101.33299		6 _{1,5} \rightarrow 6 _{1,6}	-4.0441	88	596 \pm 20	4 \pm 14
H ₂ ¹³ CO	96.37575	J_{K_a, K_c}	6 _{1,5} \rightarrow 6 _{1,6}	-4.0960	86	71 \pm 4	0.24 \pm 0.05
H ₂ C ¹⁷ O	96.38915	J_{K_a, K_c}	6 _{1,5} \rightarrow 6 _{1,6}	-4.0959	86	111 \pm 20	0.4 \pm 0.3
H ₂ C ¹⁸ O	92.09365	J_{K_a, K_c}	6 _{1,5} \rightarrow 6 _{1,6}	-4.1432	84	18.9 \pm 0.7	0.053 \pm 0.007
CH ₃ CCH	85.43117	J_K	5 ₄ \rightarrow 4 ₄	-5.4018	128	14 \pm 11	0.01 \pm 0.02
CH ₃ CCH	85.44260		5 ₃ \rightarrow 4 ₃	-4.7776	77	67 \pm 11	0.04 \pm 0.02
CH ₃ CCH	85.45077		5 ₂ \rightarrow 4 ₂	-4.9082	41	56 \pm 11	0.03 \pm 0.02
CH ₃ CCH	85.45567		5 ₁ \rightarrow 4 ₁	-4.8187	19.5	74 \pm 11	0.04 \pm 0.02
CH ₃ CCH	85.45730		5 ₀ \rightarrow 4 ₀	-4.7905	12.3	81 \pm 11	0.04 \pm 0.02
CH ₃ CCH	102.49902		6 ₅ \rightarrow 5 ₅	-5.3363	198	10 \pm 11	0.01 \pm 0.02
CH ₃ CCH	102.51664		6 ₄ \rightarrow 5 ₄	-4.9824	133	29 \pm 11	0.02 \pm 0.02
CH ₃ CCH	102.53035		6 ₃ \rightarrow 5 ₃	-4.4777	82	109 \pm 11	0.06 \pm 0.03
CH ₃ CCH	102.54014		6 ₂ \rightarrow 5 ₂	-4.6526	46	83 \pm 11	0.05 \pm 0.02
CH ₃ CCH	102.54602		6 ₁ \rightarrow 5 ₁	-4.5822	24	104 \pm 11	0.06 \pm 0.03
CH ₃ CCH	102.54798		6 ₀ \rightarrow 5 ₀	-4.5595	17.2	112 \pm 11	0.06 \pm 0.03
CH ₃ NC	100.49016	J_K	5 ₄ \rightarrow 4 ₄	-3.5850	128	5 \pm 9	0.00 \pm 0.03
CH ₃ NC	100.50607		5 ₋₃ \rightarrow 4 ₃	-3.2633	78	12 \pm 9	0.01 \pm 0.03
CH ₃ NC	100.50607		5 ₃ \rightarrow 4 ₋₃	-3.2633	78	12 \pm 9	0.01 \pm 0.03
CH ₃ NC	100.51743		5 ₂ \rightarrow 4 ₂	-3.0940	43	19 \pm 10	0.02 \pm 0.03
CH ₃ NC	100.52425		5 ₁ \rightarrow 4 ₁	-3.0053	22	25 \pm 10	0.02 \pm 0.03
CH ₃ NC	100.52654		5 ₀ \rightarrow 4 ₀	-2.9773	14.5	28 \pm 10	0.03 \pm 0.03
NH ₂ CN ($\nu=0$)	99.31120	J_{K_a, K_c}	5 _{1,5} \rightarrow 4 _{1,4}	-3.0431	29	105 \pm 6	0.34 \pm 0.08
NH ₂ CN ($\nu=1$)	99.89218		5 _{0,5} \rightarrow 4 _{0,4}	-3.1135	86	37 \pm 6	0.11 \pm 0.06
NH ₂ CN ($\nu=0$)	99.95327		5 _{2,4} \rightarrow 4 _{2,3}	-3.6359	72	14 \pm 6	0.04 \pm 0.06
NH ₂ CN ($\nu=0$)	99.95660		5 _{2,3} \rightarrow 4 _{2,2}	-3.6359	72	14 \pm 6	0.04 \pm 0.06
NH ₂ CN ($\nu=0$)	99.97267		5 _{0,5} \rightarrow 4 _{0,4}	-3.4758	14.4	52 \pm 6	0.16 \pm 0.07
NH ₂ CN ($\nu=0$)	100.62950		5 _{1,4} \rightarrow 4 _{1,3}	-3.0319	29	106 \pm 6	0.34 \pm 0.08
¹³ CS	92.49431	J	2 \rightarrow 1	-2.8001	6.7	491 \pm 11	2.5 \pm 1.0

Table D1: Continued.

Molecule	Frequency (GHz)	Quantum numbers	Transition	$\log I$ ($\text{nm}^2 \text{ MHz}$)	E_{up} (K)	Area (K km s^{-1})	τ	
$^{13}\text{C}^{34}\text{S}$	90.92603	J	$2 \rightarrow 1$	-2.8223	6.5	158 ± 6	0.32 ± 0.06	
C^{34}S	96.41295	J	$2 \rightarrow 1$	-2.7462	6.9	394 ± 8	1.17 ± 0.18	
C^{33}S	97.17206	J	$2 \rightarrow 1$	-2.7360	7.0	361 ± 18	1.0 ± 0.4	
C^{36}S	95.01672	J	$2 \rightarrow 1$	-2.7651	6.8	35 ± 4	0.08 ± 0.04	
c-C ₂ H ₄ O	84.28293	J_{K_a, K_c}	$6_{2,4} \rightarrow 6_{1,5}$	-4.4034	40	74 ± 9	0.06 ± 0.03	
c-C ₂ H ₄ O	84.58020		$7_{4,4} \rightarrow 7_{3,5}$	-4.2644	56	95 ± 9	0.08 ± 0.03	
c-C ₂ H ₄ O	84.75372		$16_{10,6} \rightarrow 16_{9,7}$	-4.0195	290	63 ± 9	0.05 ± 0.03	
c-C ₂ H ₄ O	85.33100		$9_{6,4} \rightarrow 9_{5,5}$	-4.1169	95	112 ± 9	0.10 ± 0.03	
c-C ₂ H ₄ O	87.36290		$9_{8,2} \rightarrow 9_{7,3}$	-4.2471	103	79 ± 9	0.07 ± 0.03	
c-C ₂ H ₄ O	87.57435		$10_{7,4} \rightarrow 10_{6,5}$	-4.2872	117	68 ± 9	0.06 ± 0.03	
c-C ₂ H ₄ O	91.64206		$11_{8,4} \rightarrow 11_{7,5}$	-4.0183	142	107 ± 9	0.09 ± 0.03	
c-C ₂ H ₄ O	93.29832		$15_{9,6} \rightarrow 15_{8,7}$	-4.1812	250	46 ± 9	0.04 ± 0.03	
c-C ₂ H ₄ O	93.66810		$3_{0,3} \rightarrow 2_{1,2}$	-4.4416	9.5	70 ± 9	0.06 ± 0.03	
c-C ₂ H ₄ O	94.66448		$3_{1,3} \rightarrow 2_{0,2}$	-4.2047	9.5	118 ± 9	0.10 ± 0.03	
c-C ₂ H ₄ O	95.70981		$10_{9,1} \rightarrow 10_{8,2}$	-4.1937	126	74 ± 9	0.06 ± 0.03	
c-C ₂ H ₄ O	96.67956		$10_{5,5} \rightarrow 10_{4,6}$	-4.0105	113	116 ± 9	0.10 ± 0.03	
c-C ₂ H ₄ O	100.42654		$12_{10,2} \rightarrow 12_{9,3}$	-4.0456	175	80 ± 9	0.07 ± 0.03	
c-C ₂ H ₄ O	100.43217		$9_{4,5} \rightarrow 9_{3,6}$	-4.2604	90	70 ± 9	0.06 ± 0.03	
c-C ₂ H ₄ O	101.28702		$11_{7,5} \rightarrow 11_{6,6}$	-3.9409	138	117 ± 9	0.10 ± 0.03	
c-C ₂ H ₄ O	101.50304		$10_{6,5} \rightarrow 10_{5,6}$	-4.1967	113	73 ± 9	0.06 ± 0.03	
c-C ₂ H ₄ O	102.12815		$9_{9,1} \rightarrow 9_{8,2}$	-4.4052	107	46 ± 9	0.04 ± 0.03	
c-C ₂ H ₄ O	102.15666		$12_{8,5} \rightarrow 12_{7,6}$	-4.1373	165	67 ± 9	0.06 ± 0.03	
c-C ₂ H ₄ O	102.42481		$14_{8,6} \rightarrow 14_{7,7}$	-3.9020	220	90 ± 9	0.08 ± 0.03	
c-C ₂ H ₄ O	102.64039		$8_{3,5} \rightarrow 8_{2,6}$	-4.1066	70	106 ± 9	0.09 ± 0.03	
c-C ₂ H ₄ O	102.79198	$14_{11,3} \rightarrow 14_{10,4}$	-3.9770	230	72 ± 9	0.06 ± 0.03		
c-C ₂ H ₄ O	103.22521	$8_{4,5} \rightarrow 8_{3,6}$	-4.3241	70	64 ± 9	0.06 ± 0.03		
c-C ₂ H ₄ O	104.05960	$7_{3,5} \rightarrow 7_{2,6}$	-4.2309	52	85 ± 9	0.07 ± 0.03		
c-C ₂ H ₄ O	104.61389	$13_{9,5} \rightarrow 13_{8,6}$	-3.8934	194	100 ± 9	0.09 ± 0.03		
c-C ₂ H ₄ O	105.77803	$13_{10,4} \rightarrow 13_{9,5}$	-3.9301	199	89 ± 9	0.08 ± 0.03		
c-C ₂ H ₄ O	110.01110	$13_{7,6} \rightarrow 13_{6,7}$	-4.0837	189	63 ± 9	0.06 ± 0.03		
c-C ₂ H ₄ O	110.81097	$11_{10,2} \rightarrow 11_{9,3}$	-4.1038	152	70 ± 9	0.06 ± 0.03		
c-C ₂ H ₄ O	115.33540	$12_{6,6} \rightarrow 12_{5,7}$	-3.8470	160	116 ± 9	0.10 ± 0.03		
c-C ₂ H ₄ O	115.51028	$15_{11,5} \rightarrow 15_{10,6}$	-3.8502	260	76 ± 9	0.07 ± 0.03		
H ₂ CS	101.47780	J_{K_a, K_c}	$3_{1,3} \rightarrow 2_{1,2}$	-3.6338	23	391 ± 12	> 10	
H ₂ CS	103.03990		$3_{2,2} \rightarrow 2_{2,1}$	-4.3591	63	143 ± 9	1.0 ± 0.3	
H ₂ CS	103.04045		$3_{0,3} \rightarrow 2_{0,2}$	-4.0276	9.9	347 ± 12	7 ± 170	
H ₂ CS	103.05184		$3_{2,1} \rightarrow 2_{2,0}$	-4.3590	63	143 ± 9	1.0 ± 0.3	
H ₂ CS	104.61703		$3_{1,2} \rightarrow 2_{1,1}$	-3.6077	23	393 ± 13	> 10	
H ₂ ¹³ CS	99.07613	J_{K_a, K_c}	$3_{2,2} \rightarrow 2_{2,1}$	-4.4099	62	3 ± 5	0.01 ± 0.04	
H ₂ ¹³ CS	99.07781		$3_{0,3} \rightarrow 2_{0,2}$	-4.0782	9.5	17 ± 5	0.05 ± 0.04	
H ₂ ¹³ CS	99.08632		$3_{2,1} \rightarrow 2_{2,0}$	-4.4099	62	3 ± 5	0.01 ± 0.04	
H ₂ ¹³ CS	100.53473		$3_{1,2} \rightarrow 2_{1,1}$	-3.6588	23	34 ± 5	0.10 ± 0.05	
H ₂ C ³³ S	100.59846	$J_{K_a, K_c, F+1/2}$	$3_{1,3,4} \rightarrow 2_{1,2,3}$	-4.2561	23	17 ± 7	0.05 ± 0.06	
H ₂ C ³³ S	100.59910		$3_{1,3,5} \rightarrow 2_{1,2,4}$	-4.0922	23	25 ± 7	0.07 ± 0.06	
H ₂ C ³³ S	100.60122		$3_{1,3,3} \rightarrow 2_{1,2,2}$	-4.4410	23	11 ± 7	0.03 ± 0.06	
H ₂ C ³³ S	100.60196		$3_{1,3,2} \rightarrow 2_{1,2,1}$	-4.6451	23	7 ± 7	0.02 ± 0.06	
H ₂ C ³³ S	102.13423		$3_{0,3,2} \rightarrow 2_{0,2,1}$	-5.0390	9.8	3 ± 7	0.01 ± 0.06	
H ₂ C ³³ S	102.13429		$3_{0,3,3} \rightarrow 2_{0,2,2}$	-4.8349	9.8	6 ± 7	0.02 ± 0.06	
H ₂ C ³³ S	102.13451		$3_{2,2,3} \rightarrow 2_{2,1,2}$	-5.1664	62	1 ± 7	0.00 ± 0.06	
H ₂ C ³³ S	102.13474		$3_{2,2,5} \rightarrow 2_{2,1,4}$	-4.8177	62	2 ± 7	0.01 ± 0.06	
H ₂ C ³³ S	102.13500		$3_{0,3,5} \rightarrow 2_{0,2,4}$	-4.4861	9.8	12 ± 7	0.04 ± 0.06	
H ₂ C ³³ S	102.13506		$3_{0,3,4} \rightarrow 2_{0,2,3}$	-4.6500	9.8	8 ± 7	0.02 ± 0.06	
H ₂ C ³³ S	102.13637		$3_{0,3,3} \rightarrow 2_{0,2,3}$	-5.3209	9.8	2 ± 7	0.01 ± 0.06	
H ₂ C ³³ S	103.68387		$3_{1,2,4} \rightarrow 2_{1,1,3}$	-4.2302	23	17 ± 7	0.05 ± 0.06	
H ₂ C ³³ S	103.68451		$3_{1,2,5} \rightarrow 2_{1,1,4}$	-4.0663	23	25 ± 7	0.07 ± 0.06	
H ₂ C ³⁴ S	101.28338		J_{K_a, K_c}	$3_{2,2} \rightarrow 2_{2,1}$	-4.3814	62	11 ± 5	0.03 ± 0.05

Table D1: Continued.

Molecule	Frequency (GHz)	Quantum numbers	Transition	$\log I$ ($\text{nm}^2 \text{ MHz}$)	E_{up} (K)	Area (K km s^{-1})	τ
H ₂ C ³⁴ S	101.28431		3 _{0,3} → 2 _{0,2}	-4.0498	9.7	53 ± 5	0.16 ± 0.06
H ₂ C ³⁴ S	102.80734		3 _{1,2} → 2 _{1,1}	-3.6301	23	104 ± 5	0.33 ± 0.07
trans-HONO	85.73293	J_{K_a, K_c}	3 _{1,2} → 3 _{0,3}	-4.6587	10.9	18 ± 6	0.05 ± 0.06
trans-HONO	88.91519		4 _{1,3} → 4 _{0,4}	-4.5168	15.5	22 ± 6	0.06 ± 0.06
trans-HONO	91.10546		4 _{1,4} → 3 _{1,3}	-4.5011	14.8	22 ± 6	0.07 ± 0.06
trans-HONO	93.00864		5 _{1,4} → 5 _{0,5}	-4.3895	21	25 ± 6	0.07 ± 0.06
trans-HONO	93.95279		4 _{0,4} → 3 _{0,3}	-4.4413	11.3	26 ± 6	0.08 ± 0.06
trans-HONO	94.14469		4 _{2,3} → 3 _{2,2}	-4.5869	27	15 ± 6	0.04 ± 0.06
trans-HONO	94.35453		4 _{2,2} → 3 _{2,1}	-4.5849	27	15 ± 6	0.04 ± 0.06
trans-HONO	97.13505		4 _{1,3} → 3 _{1,2}	-4.4463	15.6	24 ± 6	0.07 ± 0.06
trans-HONO	97.16409		7 _{0,7} → 6 _{1,6}	-4.7344	32	9 ± 6	0.03 ± 0.06
trans-HONO	98.08767		6 _{1,5} → 6 _{0,6}	-4.2698	28	28 ± 6	0.08 ± 0.06
trans-HONO	103.90574		1 _{1,1} → 0 _{0,0}	-5.0365	5.0	7 ± 6	0.02 ± 0.05
trans-HONO	104.23771		7 _{1,6} → 7 _{0,7}	-4.1542	37	30 ± 6	0.09 ± 0.06
trans-HONO	111.55187		8 _{1,7} → 8 _{0,8}	-4.0410	46	31 ± 6	0.09 ± 0.06
trans-HONO	113.84133		5 _{1,5} → 4 _{1,4}	-4.2076	20	32 ± 6	0.10 ± 0.06
SO	86.09395	N_J	2 ₂ → 1 ₁	-3.7129	19.3	269 ± 17	0.8 ± 0.3
SO	99.29987		2 ₃ → 1 ₂	-3.2826	9.2	525 ± 19	2.2 ± 1.2
SO	100.02964		5 ₄ → 4 ₄	-4.2359	39	61 ± 16	0.15 ± 0.15
SO	109.25222		3 ₂ → 2 ₁	-3.5047	21	316 ± 17	1.0 ± 0.4
³⁴ SO	84.41069	N_J	2 ₂ → 1 ₁	-3.7385	19.2	25 ± 6	0.07 ± 0.06
³⁴ SO	96.78176		5 ₄ → 4 ₄	-4.2700	38	5 ± 6	0.01 ± 0.05
³⁴ SO	97.71532		2 ₃ → 1 ₂	-3.3047	9.1	66 ± 6	0.20 ± 0.06
³⁴ SO	106.74324		3 ₂ → 2 ₁	-3.5335	21	30 ± 6	0.09 ± 0.06
CH ₃ SH (vt=0)	100.11022	J_{K_a, K_c}	4 _{1,3} → 3 _{1,2} A	-4.7606	17.1	41 ± 5	0.038 ± 0.014
CH ₃ SH (vt=0)	100.16413		6 _{1,5} → 6 _{0,6} E	-5.2272	32	13 ± 5	0.012 ± 0.014
CH ₃ SH (vt=0)	101.13915		4 _{0,4} → 3 _{0,3} A	-4.7166	12.1	45 ± 5	0.042 ± 0.014
CH ₃ SH (vt=0)	101.13965		4 _{0,4} → 3 _{0,3} E	-4.7183	13.6	45 ± 5	0.042 ± 0.014
CH ₃ SH (vt=0)	101.15688		4 _{3,1} → 3 _{3,0} E	-5.1317	51	15 ± 5	0.014 ± 0.014
CH ₃ SH (vt=0)	101.15933		4 _{-2,3} → 3 _{-2,2} A	-4.8688	31	30 ± 5	0.028 ± 0.014
CH ₃ SH (vt=0)	101.15999		4 _{-3,2} → 3 _{-3,1} E	-5.1335	52	15 ± 5	0.014 ± 0.014
CH ₃ SH (vt=0)	101.16066		4 _{3,1} → 3 _{3,0} A	-5.1337	53	15 ± 5	0.014 ± 0.014
CH ₃ SH (vt=0)	101.16069		4 _{-3,2} → 3 _{-3,1} A	-5.1337	53	15 ± 5	0.014 ± 0.014
CH ₃ SH (vt=0)	101.16716		4 _{-2,3} → 3 _{-2,2} E	-4.8665	30	30 ± 5	0.028 ± 0.014
CH ₃ SH (vt=0)	101.16830		4 _{2,2} → 3 _{2,1} E	-4.8674	30	30 ± 5	0.028 ± 0.014
CH ₃ SH (vt=0)	101.95538		8 _{1,7} → 8 _{0,8} E	-5.0769	50	17 ± 5	0.016 ± 0.014
CH ₃ SH (vt=0)	102.20247		4 _{-1,4} → 3 _{-1,3} A	-4.7429	17.3	42 ± 5	0.039 ± 0.014
CH ₃ SH (vt=0)	103.50419		8 _{0,8} → 7 _{1,6} A	-5.2575	44	12 ± 5	0.011 ± 0.014
CH ₃ SH (vt=0)	105.24607		10 _{1,9} → 10 _{0,10} E	-4.9596	73	20 ± 5	0.019 ± 0.014
CH ₃ SH (vt=0)	107.55635		11 _{1,10} → 11 _{0,11} E	-4.9112	87	21 ± 5	0.020 ± 0.014
CH ₃ SH (vt=0)	113.26158		7 _{-1,7} → 7 _{0,7} A	-4.8824	39	25 ± 5	0.023 ± 0.014
CH ₃ SH (vt=0)	115.48181		8 _{-1,8} → 8 _{0,8} A	-4.8301	49	27 ± 5	0.025 ± 0.014
HC ₃ N	90.97902	J	10 → 9	-2.2848	24	656 ± 17	1.6 ± 0.7
HC ₃ N	100.07639		11 → 10	-2.1673	29	699 ± 17	1.8 ± 0.9
HC ₃ N	109.17363		12 → 11	-2.0612	34	732 ± 17	2.0 ± 1.1
H ¹³ CCCN	88.16683	J	10 → 9	-2.3247	23	109 ± 7	0.26 ± 0.07
H ¹³ CCCN	96.98300		11 → 10	-2.2070	28	120 ± 7	0.28 ± 0.08
H ¹³ CCCN	105.79911		12 → 11	-2.1007	33	128 ± 7	0.31 ± 0.08
H ¹³ CCCN	114.61499		13 → 12	-2.0040	39	134 ± 7	0.32 ± 0.08
HC ¹³ CCN	90.59306	J	10 → 9	-2.2902	24	131 ± 5	0.28 ± 0.05
HC ¹³ CCN	99.65185		11 → 10	-2.1726	29	143 ± 5	0.30 ± 0.05
HC ¹³ CCN	108.71053		12 → 11	-2.0665	34	152 ± 5	0.33 ± 0.05
HCC ¹³ CN	90.60178	J	10 → 9	-2.2901	24	144 ± 6	0.34 ± 0.07
HCC ¹³ CN	99.66147		11 → 10	-2.1725	29	157 ± 6	0.37 ± 0.07
HCC ¹³ CN	108.72100		12 → 11	-2.0664	34	167 ± 7	0.40 ± 0.07
C ₂ H ₅ CHO	95.92183	J_{K_a, K_c}	9 _{1,8} → 8 _{1,7} E	-4.7545	24	13 ± 7	0.01 ± 0.02
C ₂ H ₅ CHO	95.92183		9 _{1,8} → 8 _{1,7} A	-4.7545	24	13 ± 7	0.01 ± 0.02

Table D1: Continued.

Molecule	Frequency (GHz)	Quantum numbers	Transition	$\log I$ ($\text{nm}^2 \text{ MHz}$)	E_{up} (K)	Area (K km s^{-1})	τ
C ₂ H ₅ CHO	105.23370		20 _{6,14} → 20 _{5,15} A	-4.6066	127	12 ± 7	0.01 ± 0.02
C ₂ H ₅ CHO	105.23370		20 _{6,14} → 20 _{5,15} E	-4.6066	127	12 ± 7	0.01 ± 0.02
C ₂ H ₅ CHO	105.24563		11 _{0,11} → 10 _{0,10} E	-4.5895	31	16 ± 7	0.02 ± 0.02
C ₂ H ₅ CHO	105.24563		11 _{0,11} → 10 _{0,10} A	-4.5895	31	16 ± 7	0.02 ± 0.02
C ₂ H ₅ CHO	106.14414		10 _{4,7} → 9 _{4,6} E	-4.7010	37	12 ± 7	0.01 ± 0.02
C ₂ H ₅ CHO	106.14414		10 _{4,7} → 9 _{4,6} A	-4.7010	37	12 ± 7	0.01 ± 0.02
C ₂ H ₅ CHO	114.10106		12 _{0,12} → 11 _{1,11} E	-4.4792	37	19 ± 7	0.02 ± 0.02
C ₂ H ₅ CHO	114.10106		12 _{0,12} → 11 _{1,11} A	-4.4792	37	19 ± 7	0.02 ± 0.02
C ₂ H ₅ CHO	114.39401		12 _{0,12} → 11 _{0,11} E	-4.4865	37	19 ± 7	0.02 ± 0.02
C ₂ H ₅ CHO	114.39401		12 _{0,12} → 11 _{0,11} A	-4.4865	37	19 ± 7	0.02 ± 0.02
C ₂ H ₅ CHO	114.39671		11 _{1,10} → 10 _{1,9} E	-4.5299	35	17 ± 7	0.02 ± 0.02
C ₂ H ₅ CHO	114.39671		11 _{1,10} → 10 _{1,9} A	-4.5299	35	17 ± 7	0.02 ± 0.02
C ₂ H ₅ CHO	114.56471		12 _{1,12} → 11 _{0,11} E	-4.4754	37	19 ± 7	0.02 ± 0.02
C ₂ H ₅ CHO	114.56471		12 _{1,12} → 11 _{0,11} A	-4.4754	37	19 ± 7	0.02 ± 0.02
OCS	85.13910	<i>J</i>	7 → 6	-3.7954	16.3	634 ± 12	1.9 ± 0.5
OCS	97.30121		8 → 7	-3.6277	21	706 ± 12	2.3 ± 0.8
OCS	109.46306		9 → 8	-3.4815	26	762 ± 12	2.8 ± 1.3
O ¹³ CS	84.86517	<i>J</i>	7 → 6	-3.7994	16.3	138 ± 9	0.9 ± 0.7
O ¹³ CS	96.98812		8 → 7	-3.6317	21	153 ± 9	1.0 ± 0.9
O ¹³ CS	109.11085		9 → 8	-3.4854	26	163 ± 9	1.1 ± 1.0
¹⁸ OCS	91.27539	<i>J</i>	8 → 7	-3.7102	19.7	42 ± 6	0.13 ± 0.06
¹⁸ OCS	102.68412		9 → 8	-3.5635	25	48 ± 6	0.15 ± 0.06
¹⁸ OCS	114.09261		10 → 9	-3.4337	30	53 ± 6	0.16 ± 0.06
OC ³⁴ S	94.92280	<i>J</i>	8 → 7	-3.6591	21	287 ± 12	1.3 ± 0.4
OC ³⁴ S	106.78739		9 → 8	-3.5126	26	314 ± 12	1.4 ± 0.4
OC ³³ S	96.07605	<i>J</i>	8 → 7	-3.6438	21	62 ± 6	0.19 ± 0.06
OC ³³ S	108.08478		9 → 8	-3.4974	26	70 ± 6	0.22 ± 0.06
CH ₃ OCH ₂ OH	85.08004	<i>J</i> _{K_a,K_c}	8 _{2,6} → 7 _{2,5} A	-6.6963	21	14 ± 8	0.01 ± 0.02
CH ₃ OCH ₂ OH	85.20982		8 _{1,7} → 7 _{1,6} E	-6.6736	19.1	15 ± 8	0.01 ± 0.02
CH ₃ OCH ₂ OH	85.21097		8 _{1,7} → 7 _{1,6} A	-6.6736	19.1	15 ± 8	0.01 ± 0.02
CH ₃ OCH ₂ OH	89.21647		9 _{1,9} → 8 _{1,8} E	-6.5847	22	17 ± 8	0.02 ± 0.02
CH ₃ OCH ₂ OH	89.21696		9 _{1,9} → 8 _{1,8} A	-6.5847	22	17 ± 8	0.02 ± 0.02
CH ₃ OCH ₂ OH	90.14764		9 _{0,9} → 8 _{0,8} E	-6.5734	22	18 ± 8	0.02 ± 0.02
CH ₃ OCH ₂ OH	90.14817		9 _{0,9} → 8 _{0,8} A	-6.5734	22	18 ± 8	0.02 ± 0.02
CH ₃ OCH ₂ OH	92.78498		9 _{2,8} → 8 _{2,7} E	-6.5707	25	17 ± 8	0.02 ± 0.02
CH ₃ OCH ₂ OH	92.78589		9 _{2,8} → 8 _{2,7} A	-6.5707	25	17 ± 8	0.02 ± 0.02
CH ₃ OCH ₂ OH	93.58279		9 _{7,2} → 8 _{7,1} A	-6.9814	51	6 ± 8	0.01 ± 0.02
CH ₃ OCH ₂ OH	93.58279		9 _{7,3} → 8 _{7,2} A	-6.9814	51	6 ± 8	0.01 ± 0.02
CH ₃ OCH ₂ OH	93.60710		9 _{6,3} → 8 _{6,2} E	-6.8223	43	9 ± 8	0.01 ± 0.02
CH ₃ OCH ₂ OH	93.60809		9 _{6,4} → 8 _{6,3} E	-6.8222	43	9 ± 8	0.01 ± 0.02
CH ₃ OCH ₂ OH	93.60833		9 _{6,4} → 8 _{6,3} A	-6.8222	43	9 ± 8	0.01 ± 0.02
CH ₃ OCH ₂ OH	93.60833		9 _{6,3} → 8 _{6,2} A	-6.8222	43	9 ± 8	0.01 ± 0.02
CH ₃ OCH ₂ OH	93.65692		9 _{5,4} → 8 _{5,3} E	-6.7176	37	12 ± 8	0.01 ± 0.02
CH ₃ OCH ₂ OH	93.65778		9 _{5,5} → 8 _{5,4} E	-6.7176	37	12 ± 8	0.01 ± 0.02
CH ₃ OCH ₂ OH	93.65801		9 _{5,5} → 8 _{5,4} A	-6.7176	37	12 ± 8	0.01 ± 0.02
CH ₃ OCH ₂ OH	93.65840		9 _{5,4} → 8 _{5,3} A	-6.7176	37	12 ± 8	0.01 ± 0.02
CH ₃ OCH ₂ OH	93.75157		9 _{4,6} → 8 _{4,5} A	-6.6445	32	14 ± 8	0.01 ± 0.02
CH ₃ OCH ₂ OH	93.75642		9 _{4,6} → 8 _{4,5} E	-6.6586	32	13 ± 8	0.01 ± 0.02
CH ₃ OCH ₂ OH	93.76442		9 _{4,5} → 8 _{4,4} E	-6.6585	32	13 ± 8	0.01 ± 0.02
CH ₃ OCH ₂ OH	93.77121		9 _{4,5} → 8 _{4,4} A	-6.6444	32	14 ± 8	0.01 ± 0.02
CH ₃ OCH ₂ OH	93.78982		9 _{3,7} → 8 _{3,6} E	-6.5942	28	16 ± 8	0.01 ± 0.02
CH ₃ OCH ₂ OH	93.79054		9 _{3,7} → 8 _{3,6} A	-6.5940	28	16 ± 8	0.01 ± 0.02
CH ₃ OCH ₂ OH	94.24198		9 _{3,6} → 8 _{3,5} E	-6.5900	28	16 ± 8	0.01 ± 0.02
CH ₃ OCH ₂ OH	94.24345		9 _{3,6} → 8 _{3,5} A	-6.5899	28	16 ± 8	0.01 ± 0.02
CH ₃ OCH ₂ OH	95.54203		9 _{1,8} → 8 _{1,7} E	-6.5284	24	18 ± 8	0.02 ± 0.02
CH ₃ OCH ₂ OH	95.54326		9 _{1,8} → 8 _{1,7} A	-6.5284	24	18 ± 8	0.02 ± 0.02
CH ₃ OCH ₂ OH	96.02709		9 _{2,7} → 8 _{2,6} E	-6.5401	25	18 ± 8	0.02 ± 0.02

Table D1: Continued.

Molecule	Frequency (GHz)	Quantum numbers	Transition	$\log I$ ($\text{nm}^2 \text{ MHz}$)	E_{up} (K)	Area (K km s^{-1})	τ
CH ₃ OCH ₂ OH	96.02854		9 _{2,7} → 8 _{2,6} A	-6.5401	25	18 ± 8	0.02 ± 0.02
CH ₃ OCH ₂ OH	98.96546		10 _{1,10} → 9 _{1,9} E	-6.4545	27	21 ± 8	0.02 ± 0.02
CH ₃ OCH ₂ OH	98.96598		10 _{1,10} → 9 _{1,9} A	-6.4545	27	21 ± 8	0.02 ± 0.02
CH ₃ OCH ₂ OH	99.70353		10 _{0,10} → 9 _{0,9} E	-6.4467	27	21 ± 8	0.02 ± 0.02
CH ₃ OCH ₂ OH	99.70407		10 _{0,10} → 9 _{0,9} A	-6.4467	27	21 ± 8	0.02 ± 0.02
CH ₃ OCH ₂ OH	102.91252		10 _{2,9} → 9 _{2,8} E	-6.4377	30	20 ± 8	0.02 ± 0.02
CH ₃ OCH ₂ OH	102.91349		10 _{2,9} → 9 _{2,8} A	-6.4377	30	20 ± 8	0.02 ± 0.02
CH ₃ OCH ₂ OH	103.98025		10 _{8,2} → 9 _{8,1} A	-6.9039	64	6 ± 8	0.01 ± 0.02
CH ₃ OCH ₂ OH	103.98025		10 _{8,3} → 9 _{8,2} A	-6.9039	64	6 ± 8	0.01 ± 0.02
CH ₃ OCH ₂ OH	103.99831		10 _{7,3} → 9 _{7,2} E	-6.7399	56	9 ± 8	0.01 ± 0.02
CH ₃ OCH ₂ OH	103.99951		10 _{7,4} → 9 _{7,3} E	-6.7399	56	9 ± 8	0.01 ± 0.02
CH ₃ OCH ₂ OH	103.99958		10 _{7,4} → 9 _{7,3} A	-6.7399	56	9 ± 8	0.01 ± 0.02
CH ₃ OCH ₂ OH	103.99958		10 _{7,3} → 9 _{7,2} A	-6.7399	56	9 ± 8	0.01 ± 0.02
CH ₃ OCH ₂ OH	104.03528		10 _{6,4} → 9 _{6,3} E	-6.6302	48	12 ± 8	0.01 ± 0.02
CH ₃ OCH ₂ OH	104.03637		10 _{6,5} → 9 _{6,4} E	-6.6302	48	12 ± 8	0.01 ± 0.02
CH ₃ OCH ₂ OH	104.03664		10 _{6,5} → 9 _{6,4} A	-6.6302	48	12 ± 8	0.01 ± 0.02
CH ₃ OCH ₂ OH	104.03665		10 _{6,4} → 9 _{6,3} A	-6.6302	48	12 ± 8	0.01 ± 0.02
CH ₃ OCH ₂ OH	104.10545		10 _{5,5} → 9 _{5,4} E	-6.5516	42	15 ± 8	0.01 ± 0.02
CH ₃ OCH ₂ OH	104.10633		10 _{5,6} → 9 _{5,5} A	-6.5515	42	15 ± 8	0.01 ± 0.02
CH ₃ OCH ₂ OH	104.10640		10 _{5,6} → 9 _{5,5} E	-6.5516	42	15 ± 8	0.01 ± 0.02
CH ₃ OCH ₂ OH	104.10743		10 _{5,5} → 9 _{5,4} A	-6.5515	42	15 ± 8	0.01 ± 0.02
CH ₃ OCH ₂ OH	104.22752		10 _{3,8} → 9 _{3,7} E	-6.4534	33	19 ± 8	0.02 ± 0.02
CH ₃ OCH ₂ OH	104.22853		10 _{3,8} → 9 _{3,7} A	-6.4534	33	19 ± 8	0.02 ± 0.02
CH ₃ OCH ₂ OH	104.22965		10 _{4,7} → 9 _{4,6} A	-6.4938	37	17 ± 8	0.02 ± 0.02
CH ₃ OCH ₂ OH	104.23394		10 _{4,7} → 9 _{4,6} E	-6.5126	37	17 ± 8	0.02 ± 0.02
CH ₃ OCH ₂ OH	104.26533		10 _{4,6} → 9 _{4,5} E	-6.5123	37	17 ± 8	0.02 ± 0.02
CH ₃ OCH ₂ OH	104.27179		10 _{4,6} → 9 _{4,5} A	-6.4934	37	17 ± 8	0.02 ± 0.02
CH ₃ OCH ₂ OH	104.97919		10 _{3,7} → 9 _{3,6} E	-6.4472	33	19 ± 8	0.02 ± 0.02
CH ₃ OCH ₂ OH	104.98066		10 _{3,7} → 9 _{3,6} A	-6.4471	33	19 ± 8	0.02 ± 0.02
CH ₃ OCH ₂ OH	105.74159		10 _{1,9} → 9 _{1,8} E	-6.4012	29	22 ± 8	0.02 ± 0.02
CH ₃ OCH ₂ OH	105.74285		10 _{1,9} → 9 _{1,8} A	-6.4012	29	22 ± 8	0.02 ± 0.02
CH ₃ OCH ₂ OH	106.95038		10 _{2,8} → 9 _{2,7} E	-6.4034	30	21 ± 8	0.02 ± 0.02
CH ₃ OCH ₂ OH	106.95198		10 _{2,8} → 9 _{2,7} A	-6.4034	30	21 ± 8	0.02 ± 0.02
CH ₃ OCH ₂ OH	108.68584		11 _{1,11} → 10 _{1,10} E	-6.3383	32	24 ± 8	0.02 ± 0.02
CH ₃ OCH ₂ OH	108.68638		11 _{1,11} → 10 _{1,10} A	-6.3383	32	24 ± 8	0.02 ± 0.02
CH ₃ OCH ₂ OH	109.24857		11 _{0,11} → 10 _{0,10} E	-6.3330	32	24 ± 8	0.02 ± 0.02
CH ₃ OCH ₂ OH	109.24914		11 _{0,11} → 10 _{0,10} A	-6.3330	32	24 ± 8	0.02 ± 0.02
CH ₃ OCH ₂ OH	112.98786		11 _{2,10} → 10 _{2,9} E	-6.3197	35	24 ± 8	0.02 ± 0.02
CH ₃ OCH ₂ OH	112.98889		11 _{2,10} → 10 _{2,9} A	-6.3197	35	24 ± 8	0.02 ± 0.02
CH ₃ OCH ₂ OH	114.38015		11 _{9,2} → 10 _{9,1} A	-7.0137	80	4 ± 8	0.00 ± 0.02
CH ₃ OCH ₂ OH	114.38015		11 _{9,3} → 10 _{9,2} A	-6.9457	80	5 ± 8	0.00 ± 0.02
CH ₃ OCH ₂ OH	114.39297		11 _{8,3} → 10 _{8,2} E	-6.6704	70	9 ± 8	0.01 ± 0.02
CH ₃ OCH ₂ OH	114.39426		11 _{8,3} → 10 _{8,2} A	-6.6704	70	9 ± 8	0.01 ± 0.02
CH ₃ OCH ₂ OH	114.39426		11 _{8,4} → 10 _{8,3} A	-6.6704	70	9 ± 8	0.01 ± 0.02
CH ₃ OCH ₂ OH	114.39440		11 _{8,4} → 10 _{8,3} E	-6.6704	70	9 ± 8	0.01 ± 0.02
CH ₃ OCH ₂ OH	114.42086		11 _{7,4} → 10 _{7,3} E	-6.5562	61	13 ± 8	0.01 ± 0.02
CH ₃ OCH ₂ OH	114.42218		11 _{7,5} → 10 _{7,4} E	-6.5562	61	13 ± 8	0.01 ± 0.02
CH ₃ OCH ₂ OH	114.42227		11 _{7,5} → 10 _{7,4} A	-6.5562	61	13 ± 8	0.01 ± 0.02
CH ₃ OCH ₂ OH	114.42227		11 _{7,4} → 10 _{7,3} A	-6.5562	61	13 ± 8	0.01 ± 0.02
CH ₃ OCH ₂ OH	114.47210		11 _{6,5} → 10 _{6,4} E	-6.4729	54	16 ± 8	0.01 ± 0.02
CH ₃ OCH ₂ OH	114.47330		11 _{6,6} → 10 _{6,5} E	-6.4729	54	16 ± 8	0.01 ± 0.02
CH ₃ OCH ₂ OH	114.47358		11 _{6,6} → 10 _{6,5} A	-6.4729	54	16 ± 8	0.01 ± 0.02
CH ₃ OCH ₂ OH	114.47363		11 _{6,5} → 10 _{6,4} A	-6.4729	54	16 ± 8	0.01 ± 0.02
CH ₃ OCH ₂ OH	114.56750		11 _{5,6} → 10 _{5,5} E	-6.4104	47	18 ± 8	0.02 ± 0.02
CH ₃ OCH ₂ OH	114.56765		11 _{5,7} → 10 _{5,6} A	-6.4101	47	18 ± 8	0.02 ± 0.02
CH ₃ OCH ₂ OH	114.56841		11 _{5,7} → 10 _{5,6} E	-6.4104	47	18 ± 8	0.02 ± 0.02
CH ₃ OCH ₂ OH	114.57037		11 _{5,6} → 10 _{5,5} A	-6.4101	47	18 ± 8	0.02 ± 0.02
CH ₃ OCH ₂ OH	114.64784		11 _{3,9} → 10 _{3,8} E	-6.3295	38	23 ± 8	0.02 ± 0.02

Table D1: Continued.

Molecule	Frequency (GHz)	Quantum numbers	Transition	$\log I$ ($\text{nm}^2 \text{ MHz}$)	E_{up} (K)	Area (K km s^{-1})	τ
CH ₃ OCH ₂ OH	114.64902		11 _{3,9} → 10 _{3,8} A	-6.3295	38	23 ± 8	0.02 ± 0.02
CH ₃ OCH ₂ OH	114.72196		11 _{4,8} → 10 _{4,7} A	-6.3626	42	21 ± 8	0.02 ± 0.02
CH ₃ OCH ₂ OH	114.72379		11 _{4,8} → 10 _{4,7} E	-6.3702	42	21 ± 8	0.02 ± 0.02
CH ₃ OCH ₂ OH	114.80088		11 _{4,7} → 10 _{4,6} E	-6.3696	42	21 ± 8	0.02 ± 0.02
CH ₃ OCH ₂ OH	114.80513		11 _{4,7} → 10 _{4,6} A	-6.3620	42	21 ± 8	0.02 ± 0.02
CH ₃ OCH ₂ OH	115.79249		11 _{1,10} → 10 _{1,9} E	-6.2886	34	25 ± 8	0.02 ± 0.02
CH ₃ OCH ₂ OH	115.79376		11 _{1,10} → 10 _{1,9} A	-6.2886	34	25 ± 8	0.02 ± 0.02
CH ₃ OCH ₂ OH	115.81704		11 _{3,8} → 10 _{3,7} E	-6.3207	38	23 ± 8	0.02 ± 0.02
CH ₃ OCH ₂ OH	115.81863		11 _{3,8} → 10 _{3,7} A	-6.3207	38	23 ± 8	0.02 ± 0.02
SO ₂	86.63909	J_{K_a, K_c}	8 _{3,5} → 9 _{2,8}	-4.7055	55	51 ± 12	0.09 ± 0.09
SO ₂	97.70233		7 _{3,5} → 8 _{2,6}	-4.6702	48	55 ± 12	0.10 ± 0.09
SO ₂	100.87811		2 _{2,0} → 3 _{1,3}	-5.3576	12.6	19 ± 12	0.03 ± 0.08
SO ₂	104.02942		3 _{1,3} → 2 _{0,2}	-4.2264	7.7	231 ± 13	0.45 ± 0.13
SO ₂	104.03358		16 _{2,14} → 15 _{3,13}	-4.2421	138	38 ± 12	0.06 ± 0.09
SO ₂	104.23930		10 _{1,9} → 10 _{0,10}	-3.7708	55	313 ± 13	0.64 ± 0.15
SO ₂	107.84347		12 _{4,8} → 13 _{3,11}	-4.4181	111	36 ± 12	0.06 ± 0.09
³⁴ SO ₂	102.03188	J_{K_a, K_c}	3 _{1,3} → 2 _{0,2}	-4.2159	7.6	38 ± 4	0.10 ± 0.04
³⁴ SO ₂	104.39171		10 _{1,9} → 10 _{0,10}	-3.7543	55	54 ± 4	0.15 ± 0.05
³³ SO ₂	93.07066	$J_{K_a, K_c, F+1/2}$	7 _{3,5,6} → 8 _{2,6,7}	-5.3800	47	4 ± 6	0.01 ± 0.04
³³ SO ₂	93.07115		7 _{3,5,9} → 8 _{2,6,10}	-5.2125	47	6 ± 6	0.01 ± 0.04
³³ SO ₂	93.07315		7 _{3,5,7} → 8 _{2,6,8}	-5.3240	47	5 ± 6	0.01 ± 0.04
³³ SO ₂	93.07359		7 _{3,5,8} → 8 _{2,6,9}	-5.2679	47	5 ± 6	0.01 ± 0.04
³³ SO ₂	102.99524		3 _{1,3,2} → 2 _{0,2,1}	-5.2041	7.7	10 ± 6	0.02 ± 0.04
³³ SO ₂	102.99551		3 _{1,3,2} → 2 _{0,2,2}	-5.6022	7.7	4 ± 6	0.01 ± 0.04
³³ SO ₂	102.99824		3 _{1,3,5} → 2 _{0,2,4}	-4.6513	7.7	35 ± 6	0.07 ± 0.04
³³ SO ₂	103.00143		3 _{1,3,3} → 2 _{0,2,2}	-5.0000	7.7	16 ± 6	0.03 ± 0.04
³³ SO ₂	103.00161		3 _{1,3,3} → 2 _{0,2,3}	-5.4862	7.7	5 ± 6	0.01 ± 0.04
³³ SO ₂	103.00411		3 _{1,3,4} → 2 _{0,2,4}	-5.5932	7.7	4 ± 6	0.01 ± 0.04
³³ SO ₂	103.00440		3 _{1,3,4} → 2 _{0,2,3}	-4.8152	7.7	24 ± 6	0.05 ± 0.04
³³ SO ₂	104.29673		10 _{1,9,11} → 10 _{0,10,11}	-4.3407	55	35 ± 6	0.07 ± 0.04
³³ SO ₂	104.29805		10 _{1,9,10} → 10 _{0,10,10}	-4.3834	55	32 ± 6	0.07 ± 0.04
³³ SO ₂	104.30599		10 _{1,9,12} → 10 _{0,10,12}	-4.2948	55	39 ± 6	0.08 ± 0.04
³³ SO ₂	104.30730		10 _{1,9,9} → 10 _{0,10,9}	-4.4214	55	29 ± 6	0.06 ± 0.04
Non detected molecules							
H ¹⁵ NC	88.86571	J	1 → 0	-2.5690	4.3	< 6	< 0.017
C ¹⁷ O	112.35878	$J_{F+1/2}$	1 ₂ → 0 ₃	-5.6952	5.4	< 4	< 0.012
C ¹⁷ O	112.35898		1 ₄ → 0 ₃	-5.3942	5.4	< 8	< 0.02
C ¹⁷ O	112.36001		1 ₃ → 0 ₃	-5.5191	5.4	< 6	< 0.018
H ₂ S	89.49799	J_{K_a, K_c}	7 _{1,6} → 6 _{4,3}	-6.7612	520	< 3	< 9 · 10 ⁻³
C ₃ H ₆	103.68912	J_{K_a, K_c}	6 _{0,6} → 5 _{0,5} E	-5.7493	17.5	< 1.5	< 1.4 · 10 ⁻³
C ₃ H ₆	103.69002		6 _{0,6} → 5 _{0,5} A	-5.7493	17.5	< 1.5	< 1.4 · 10 ⁻³
HOCN	104.87468	J_{K_a, K_c}	5 _{0,5} → 4 _{0,4}	-2.8221	15.1	< 9	< 0.03
syn-CH ₂ CHOH	96.87491	J_{K_a, K_c}	5 _{0,5} → 4 _{0,4}	-5.0111	14.0	< 10	< 9 · 10 ⁻³
PN	93.97977	J	2 → 1	-2.4850	6.8	< 8	< 0.02
PO (² Π _{1/2} , $v = 0$)	109.20620	$J + 1/2_F(\Lambda)$	3 ₃ → 2 ₃ (f)	-3.3018	8.4	< 5	< 0.015
CH ₃ Cl	106.33474	$J_{K, F+1/2}$	4 _{2,6} → 3 _{2,5}	-4.1714	43	< 1.7	< 5 · 10 ⁻³
CH ₃ Cl	106.33505		4 _{1,4} → 3 _{1,3}	-4.2831	20	< 1.9	< 6 · 10 ⁻³
CH ₃ Cl	106.33603		4 _{1,5} → 3 _{1,4}	-4.1589	20	< 3	< 7 · 10 ⁻³
CH ₃ Cl	106.33683		4 _{0,3} → 3 _{0,2}	-4.3710	12.8	< 1.8	< 5 · 10 ⁻³
CH ₃ Cl	106.33683		4 _{0,4} → 3 _{0,3}	-4.2442	12.8	< 2	< 7 · 10 ⁻³
CH ₃ Cl	106.33692		4 _{1,3} → 3 _{1,2}	-4.4099	20	< 1.4	< 4 · 10 ⁻³
CH ₃ Cl	106.33790		4 _{1,6} → 3 _{1,5}	-4.0420	20	< 3	< 0.010
CH ₃ Cl	106.33896		4 _{0,5} → 3 _{0,4}	-4.1200	12.8	< 3	< 9 · 10 ⁻³
CH ₃ Cl	106.33896		4 _{0,6} → 3 _{0,5}	-4.0030	12.8	< 4	< 0.012
HC ₂ NC	109.28910	N_J	11 ₁₂ → 10 ₁₁	-2.7069	31	< 1.8	< 5 · 10 ⁻³

Table D1: Continued.

Molecule	Frequency (GHz)	Quantum numbers	Transition	$\log I$ ($\text{nm}^2 \text{ MHz}$)	E_{up} (K)	Area (K km s^{-1})	τ
HC ₂ NC	109.28910		11 ₁₁ → 10 ₁₀	-2.7467	31	< 1.7	< 5 · 10 ⁻³
HC ₂ NC	109.28910		11 ₁₀ → 10 ₉	-2.7866	31	< 1.5	< 4 · 10 ⁻³
trans-C ₂ H ₃ CHO	114.65333	J_{K_a, K_c}	13 _{0,13} → 12 _{0,12}	-3.4357	39	< 11	< 0.010
HOCH ₂ CN	112.92288	J_{K_a, K_c}	12 _{1,11} → 11 _{1,10} 0 ⁻	-4.1281	37	< 12	< 0.011
CH ₃ CHCH ₂ O	103.70741	J_{K_a, K_c}	19 _{5,15} → 19 _{4,16}	-4.3734	130	< 12	< 0.011
gauche-C ₂ H ₅ SH	113.62252	J_{K_a, K_c}	11 _{1,10} → 10 _{1,9} 0 ⁻	-4.5362	34	< 10	< 9 · 10 ⁻³
gauche-C ₂ H ₅ SH	113.62443		11 _{1,10} → 10 _{1,9} 0 ⁺	-4.5363	34	< 10	< 9 · 10 ⁻³
S ₂	104.68660	N_J	7 ₇ → 7 ₆	-6.7048	57	< 15	< 0.04
HS ₂	110.29403	$J_{K_a, K_c, J+1/2, F}$	7 _{0,7,8,7} → 6 _{0,6,7,6}	-4.5604	21	< 7	< 0.02
HS ₂	110.29415		7 _{0,7,8,8} → 6 _{0,6,7,7}	-4.5019	21	< 8	< 0.02
H ₂ S ₂	98.07649	J_{K_a, K_c}	2 _{1,1} → 3 _{0,3}	-4.9609	8.7	< 20	< 0.06
NH ₂ CH ₂ COOH (conf. I)	113.15603	J_{K_a, K_c}	17 _{2,15} → 16 _{2,14}	-4.9207	53	< 4	< 4 · 10 ⁻³
NH ₂ CH ₂ COOH (conf. I)	113.33620		19 _{1,19} → 18 _{1,18}	-4.8602	56	< 5	< 5 · 10 ⁻³
NH ₂ CH ₂ COOH (conf. I)	113.33669		19 _{0,19} → 18 _{0,18}	-4.8602	56	< 5	< 5 · 10 ⁻³

APPENDIX E: STATISTICAL TESTS

We have used three complementary correlation tests, Spearman (r_s), Kendall (τ) and Theil-Sen (T-S), to perform a quantitative analysis of the comparison of the chemical content in the different interstellar sources. We explain here the basics of these correlation tests, and how to interpret their results.

E1 Spearman

Spearman correlation test (r_s) is a non-parametric test or a range correlation test. This test orders the x_i and y_i data from lower to higher separately. Once the data of x_i and y_i is reordered, each data are replaced by its range, i.e. an integer number starting by 1 for x_i and y_i following the order. If two or more data have the same value (x_i or y_i), the number assigned is the average number of the ranges. The formula which calculates the Spearman correlation coefficient depends on the range of both data, in this case the range of x_i and y_i is R_i and S_i respectively. Therefore, this is the formula:

$$r_s = \frac{\sum_{i=1}^n (R_i - \bar{R})(S_i - \bar{S})}{\sqrt{\sum_{i=1}^n (R_i - \bar{R})^2} \sqrt{\sum_{i=1}^n (S_i - \bar{S})^2}} \quad (\text{E1})$$

The range of this correlation test is from -1 to 1. -1 is perfect anti-correlation, 0 no correlation at all and 1 perfect correlation.

E2 Kendall

Kendall correlation test (τ) is based on Kendall correlation coefficient which is a non-parametrical correlation test. In this case, we calculate by pairs of n data (x_i, y_i). We have the n data (x, y) with all the possible pair of points (x_i, y_i) - (x_j, y_j) having $n(n-1)/2$ different pairs, which are classified in two different categories. Any pair of data (x_i, y_i) and (x_j, y_j) where $i \neq j$ are concordant if $x_i > x_j$ and $y_i > y_j$ or $x_i < x_j$ and $y_i < y_j$. Otherwise, the pair of data are discordant.

To calculate the value of this coefficient the equations is the following:

$$\tau = \frac{2(n_C - n_D)}{n(n-1)} \quad (\text{E2})$$

Where n_C is the concordant pair, n_D is the discordant one and n is the number of the data (x, y). This coefficient has the same range and interpretation as Spearman correlation coefficient.

E3 Theil-Sen

The Theil-Sen estimator (T-S) is an alternative for the conventional linear regression (i.e. Pearson correlation coefficient). This method provides us with a non-parametric linear regression which is very robust. It is very effective against outliers. The idea is to calculate the slope (b_{ij}) for each possible pair of points, using the following formula:

$$b_{ij} = \frac{y_j - y_i}{x_j - x_i} \quad (\text{E3})$$

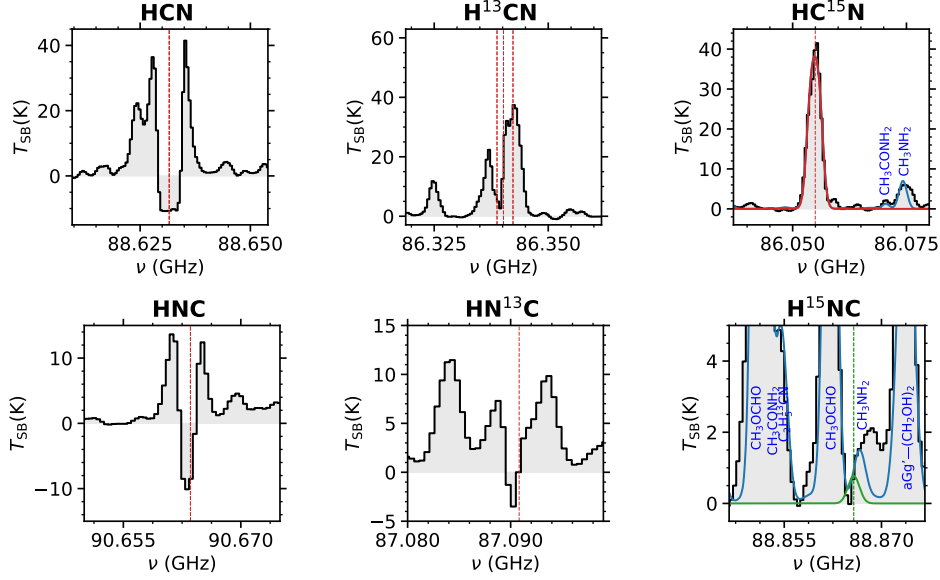


Figure F1. HCN and HNC isotopologues described in Sect. 4.1.1 and 4.1.2. The black histogram and its grey shadow are the observational spectrum. The red curve is the fit of the individual transition, the green curve is the upper limit obtained using that transition and the blue curve is the cumulative fit considering all detected species. The red/green dashed lines indicate the frequency of the molecular transitions.

The final estimation for the slope (b_{T-S}) of the linear regression is the median of all the slopes. The intercept point is calculated by doing the median of all the intercept points of the data.

Once we have the slope, we use formula which associates the slope of a linear regression with a correlation coefficient (this is used to obtain Pearson correlation coefficient), Theil-Sen in this case. The formula is the following:

$$T-S = \sqrt{b_{T-S}(y, x) \times b_{T-S}(x, y)} \quad (\text{E4})$$

By doing so, we obtain a correlation coefficient from a linear regression, but more robust and less dependent on outliers. This correlation coefficient has the same range and interpretation as Spearman and Kendall. The difference is that this coefficient is evaluating if the points are close to a straight line, and the other coefficients evaluates if the points are monotonically increasing or decreasing.

To calculate the p -value of Theil-Sen, we use the p -value of Pearson correlation coefficient, due to this estimator is a modified linear regression (Pearson), so for p -value we used the t distribution:

$$t = \frac{r\sqrt{n-2}}{\sqrt{1-r^2}} \quad (\text{E5})$$

where r is the coefficient value and n is the number of observations. To calculate the p -value the formula is $2 \times P(T > t)$ where T follows a t distribution with $n-2$ degrees of freedom. P is the probability of a certain value of being higher than t , P follows the density distribution of a t distribution. We integrated the probability density from t to infinite to obtain the P , the expression used is the following:

$$P_{x>t} = \int_t^\infty \frac{\Gamma(\frac{n+1}{2})}{\sqrt{n\pi}\Gamma(\frac{n}{2})} \left(1 + \frac{x^2}{n}\right)^{-\frac{n+1}{2}} dx \quad (\text{E6})$$

Where n is the degrees of freedom, t is the t distribution described in equation E5, and x is T .

To obtain the p -value we solve the equation E6 and we multiply the result by 2 because the p -value is from two tails of the Gaussian.

APPENDIX F: REMAINING SPECTRA OF DETECTED MOLECULES

We show here the spectra of the detected molecules towards G31.41 analyzed in this work that have not been presented in the main text. The results of the parameters obtained from the fits are summarized in Table 2 and Table A1, and the information about the transitions used are listed in Table D1.

APPENDIX G: MOLECULES NOT DETECTED TOWARDS G31.41+0.31

The spectra of the transitions used to obtain the column density upper limits towards G31.41 presented in Table 2 are shown in Fig. G1, and the information about the transitions used are included in Table D1. The upper limits are calculated by using the brightest transitions according to the LTE model that are not heavily blended, and by performing a visual inspection to make the upper limits compatible with the observed

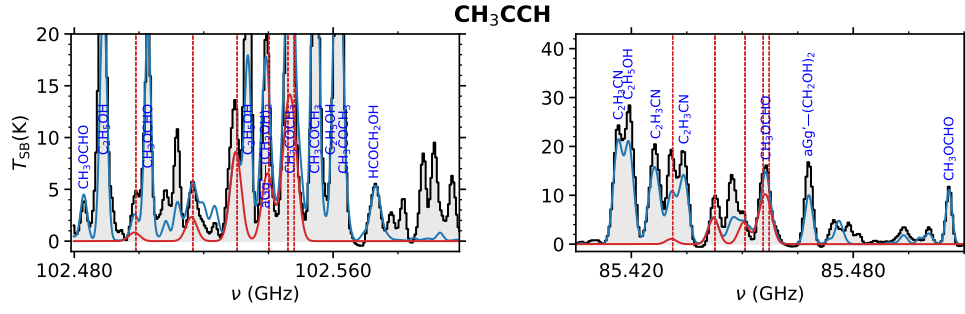


Figure F4. CH_3CCH described in Sect. 4.1.5. The black histogram and its grey shadow are the observational spectrum. The red curve is the fit of the individual transition and the blue curve is the cumulative fit considering all detected species. The red dashed lines indicate the frequency of the molecular transitions. The plots are sorted by decreasing intensity of the corresponding species (red line).

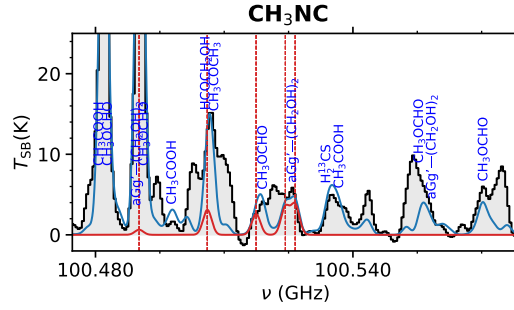


Figure F5. CH_3NC described in Sect. 4.1.6. The black histogram and its grey shadow are the observational spectrum. The red curve is the fit of the individual transition and the blue curve is the cumulative fit considering all detected species. The red dashed lines indicate the frequency of the molecular transitions.

This paper has been typeset from a $\text{T}_{\text{E}}\text{X}/\text{L}^{\text{A}}\text{T}_{\text{E}}\text{X}$ file prepared by the author.

HONO

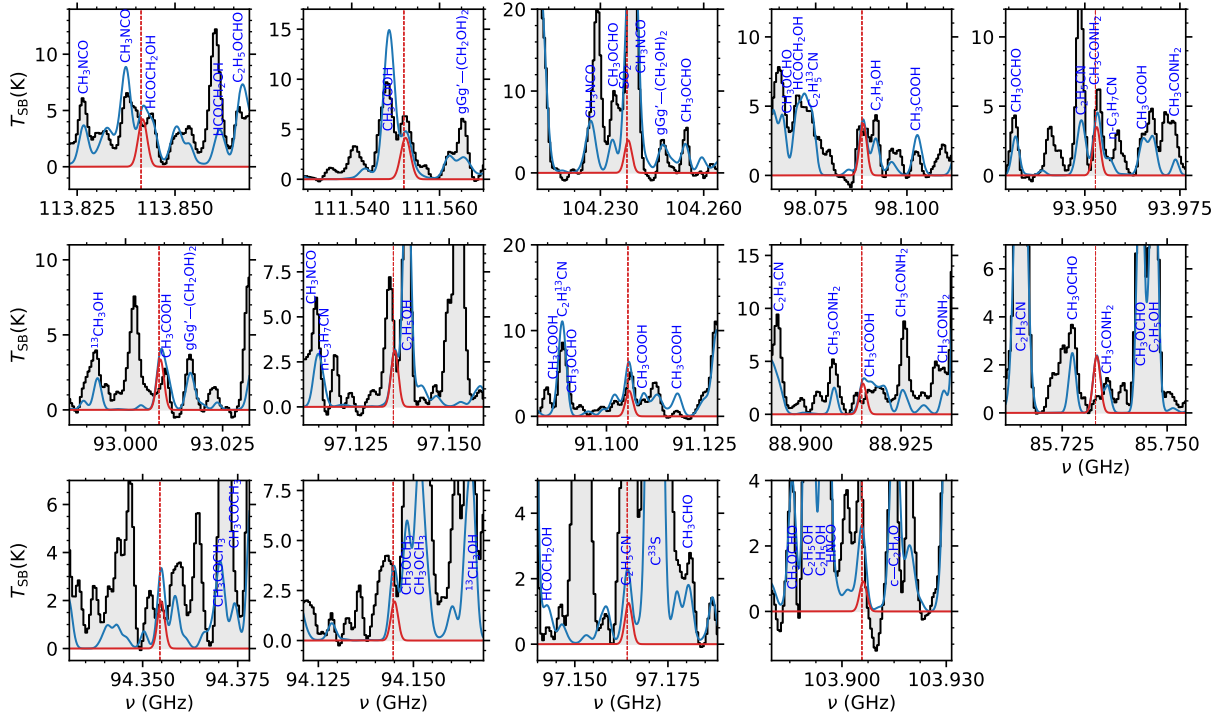


Figure F7. HONO described in Sect. 4.1.11. The black histogram and its grey shadow are the observational spectrum. The red curve is the fit of the individual transition and the blue curve is the cumulative fit considering all detected species. The red dashed lines indicate the frequency of the molecular transitions. The plots are sorted by decreasing intensity of the corresponding species (red line).

SO

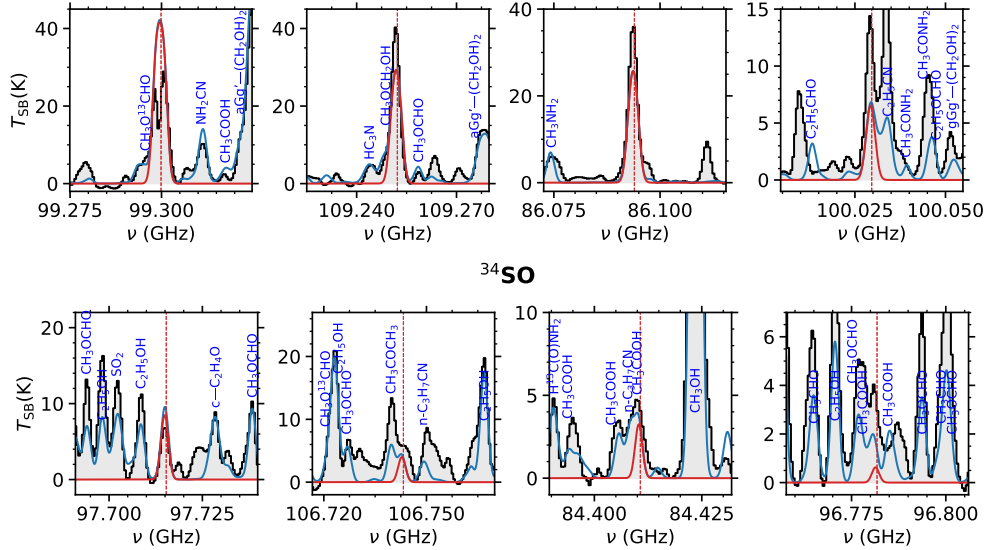


Figure F8. SO isotopologue described in Sect. 4.1.12. The black histogram and its grey shadow are the observational spectrum. The red curve is the fit of the individual transition and the blue curve is the cumulative fit considering all detected species. The red dashed lines indicate the frequency of the molecular transitions. The plots are sorted by decreasing intensity of the corresponding species (red line).

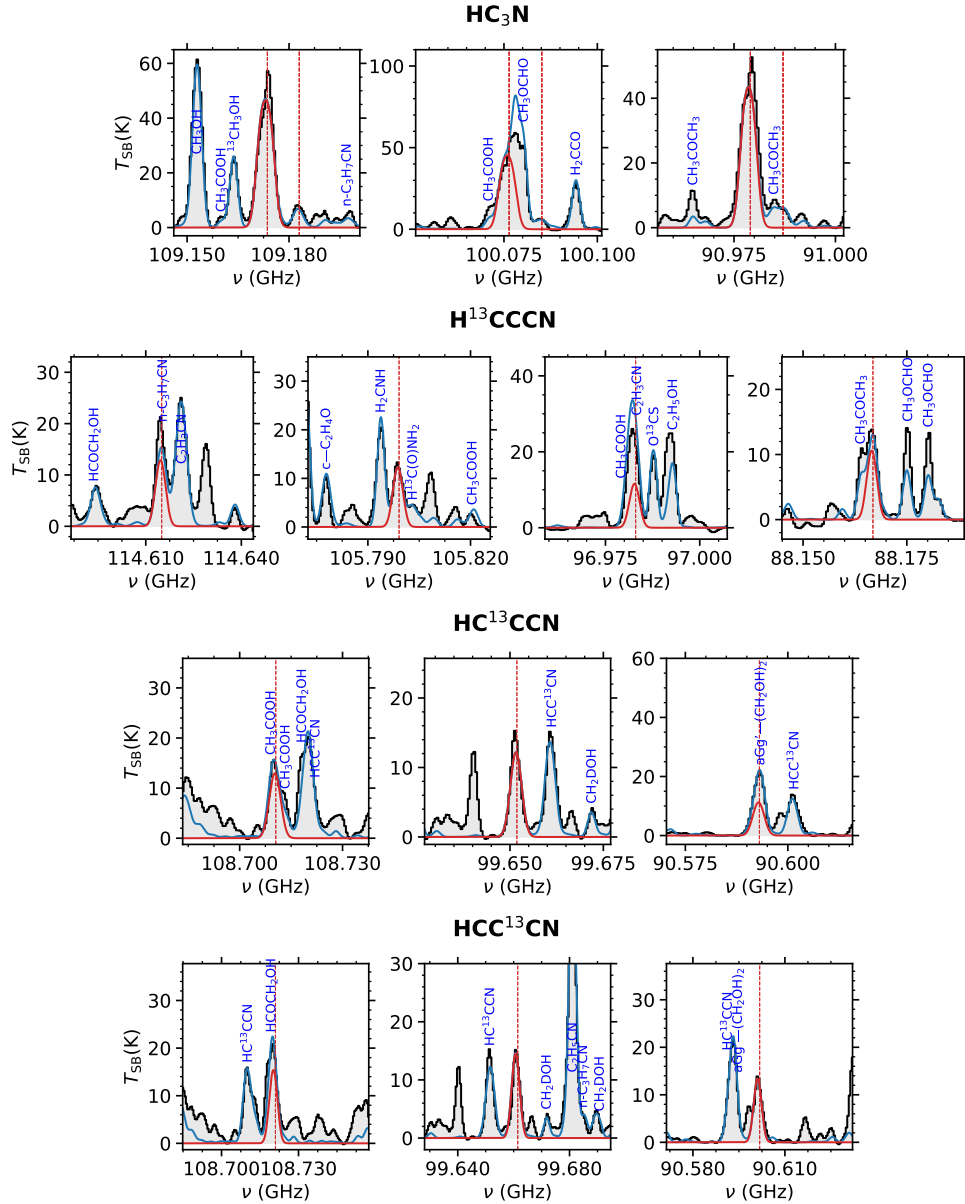


Figure F9. HC₃N isotopologues described in Sect. 4.1.14. The black histogram and its grey shadow are the observational spectrum. The red curve is the fit of the individual transition and the blue curve is the cumulative fit considering all detected species. The red dashed lines indicate the frequency of the molecular transitions. The plots are sorted by decreasing intensity of the corresponding species (red line).

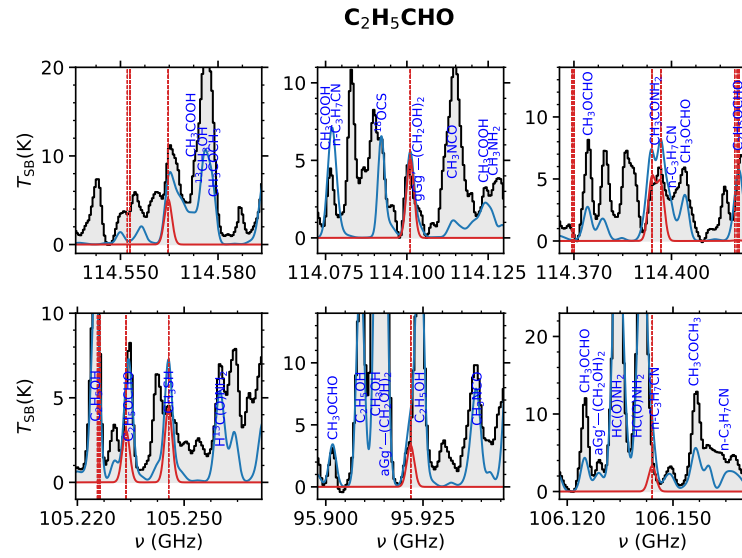


Figure F10. C₂H₅CHO described in Sect. 4.1.15. The black histogram and its grey shadow are the observational spectrum. The red curve is the fit of the individual transition and the blue curve is the cumulative fit considering all detected species. The red dashed lines indicate the frequency of the molecular transitions. The plots are sorted by decreasing intensity of the corresponding species (red line).

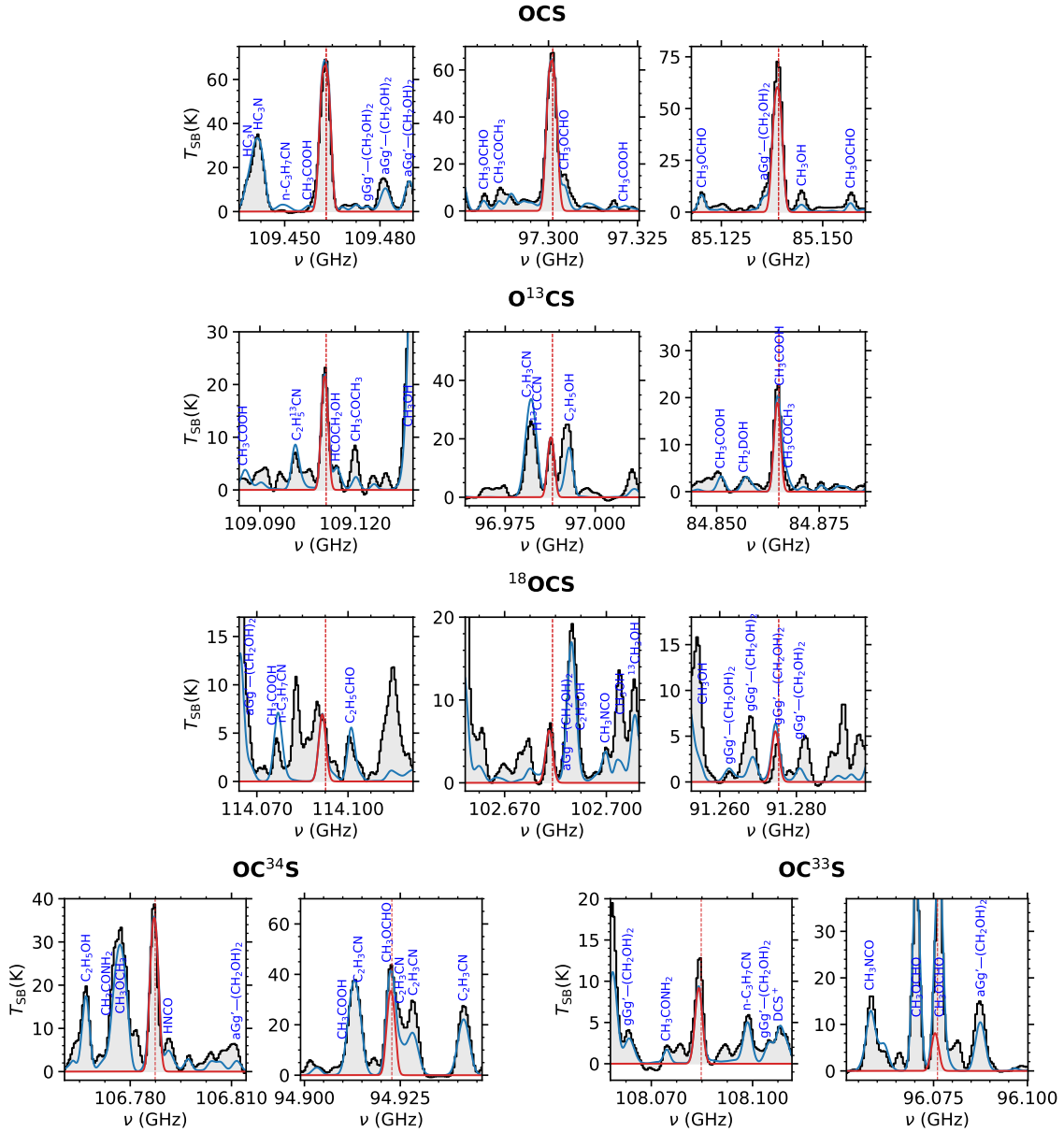


Figure F11. OCS isotopologues described in Sect. 4.1.16. The black histogram and its grey shadow are the observational spectrum. The red curve is the fit of the individual transition and the blue curve is the cumulative fit considering all detected species. The red dashed lines indicate the frequency of the molecular transitions. The plots are sorted by decreasing intensity of the corresponding species (red line).

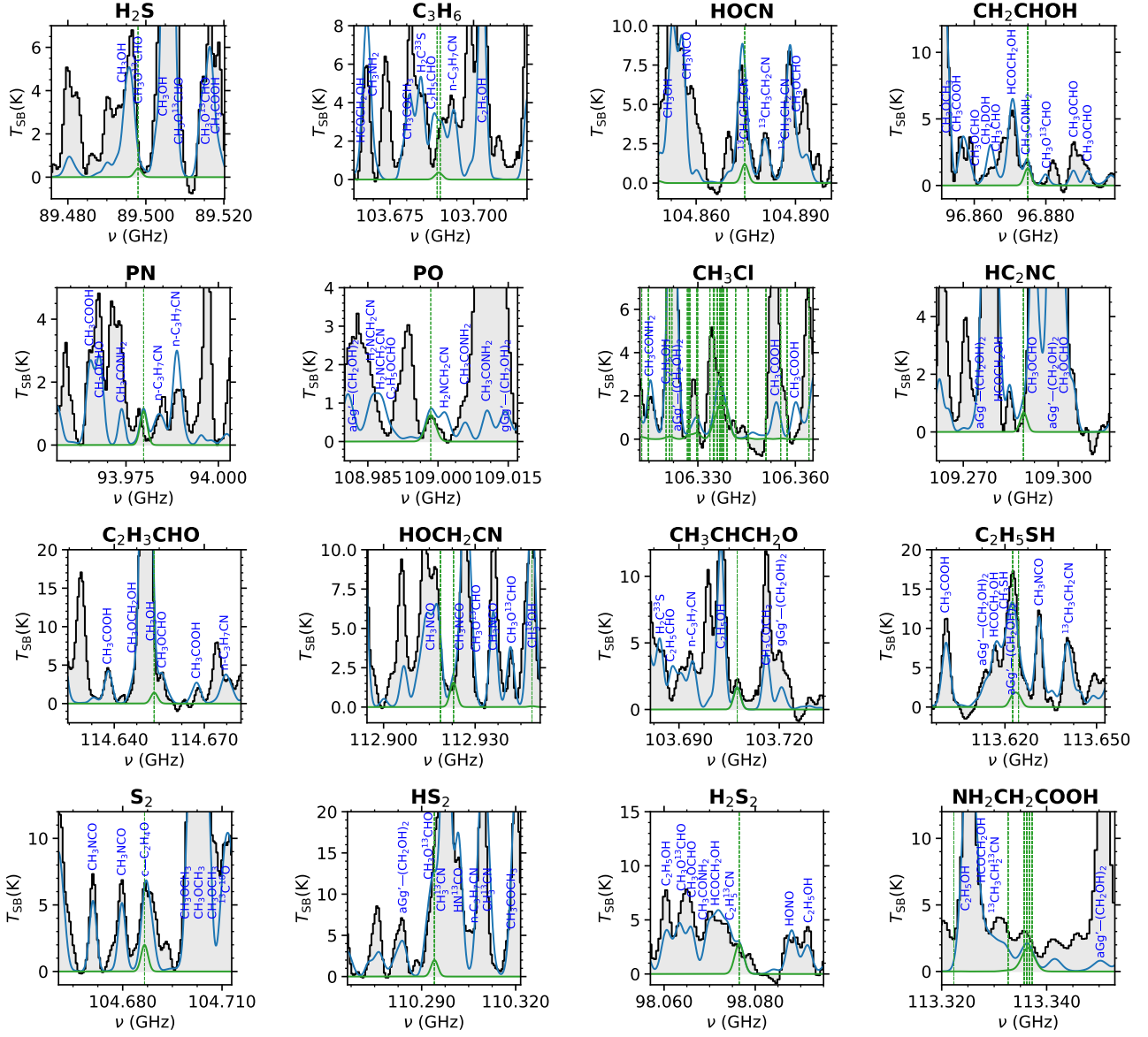


Figure G1. Molecules not detected in G31.41. The black histogram and its grey shadow are the observational spectrum. The LTE synthetic spectra using the derived upper limits of N are indicated with green curves. To compute the upper limits of their molecular abundances we have used the brightest and less blended transitions, which are shown here. The green dashed lines indicate the frequency of the molecular transitions. The transitions of this plots are in Table D1 on the not detected molecules section.

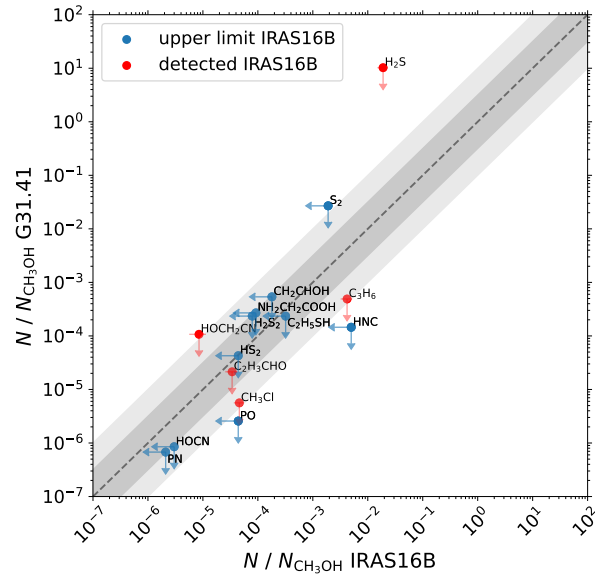


Figure G2. Molecular abundances of G31.41 upper limits with respect to CH_3OH compared with their respective values of IRAS16B. The errorbars marked with arrows are the upper limits. Grey dotted line is the 1:1 relation on each plot. Dark and light grey are half and one order of magnitude difference with respect to the grey dotted line.